**POLITECNICO DI MILANO**

**Scuola di Ingegneria Industriale e dell'Informazione**
**Electrical engineering Master of Science Course**

LUCAS YUGO TANIO

# CONVERTERS FOR AUTOMOTIVE APPLICATIONS

Multidevice Interleaved Boost Converter

Milano – MI
2018

LUCAS YUGO TANIO

# CONVERTERS FOR AUTOMOTIVE APPLICATIONS

Multidevice Interleaved Boost Converter

Thesis presented at Politecnico di Milano, as part of requirements to obtain the title of Master of Science in Electrical Engineering.

Area: Power electronics, converters

Supervisor: Prof. Roberto Perini

Milano – MI
2018

Tanio, Lucas Yugo

Converters for automotive applications / Lucas Yugo Tanio. – Milano, 2018. 102p.

Thesis Master of Science – Politecnico di Milano, Scuola di Ingegneria Industriale e dell’Informazione

Supervisor: Prof. Roberto Perini

1. Hybrid electric vehicles. 2. DC/DC converters. 3. Small signal model; 4. Dual loop control

Name: Lucas Yugo Tanio

Title: Converters for automotive applications

Thesis presented to the Master of Science program in Electrical Engineering at Scuola di Ingegneria Industriale e dell' Informazione of Politécnico di Milano

Approved thesis. Milano, _____ ____, 2018.

EXAMINATION BOARD

_____

Prof. Roberto Perini

Associated Professor at Politecnico di Milano

_____

*To my family and friends*

*who supported me in this journey.*

## Acknowledgements

I would like to express my gratitude to my thesis advisor, Professor Roberto Perini, for the trust and assistance to develop this thesis. I would also like to thank the Politecnico di Milano for the study opportunity and the support of my family and friends.

# SOMMARIO

L'interesse per i veicoli ibridi elettrici è in crescita, non solo a causa dell'impatto ambientale nel settore dei trasporti, ma anche perché sono economicamente interessanti per quanto riguarda i costi di guida e manutenzione rispetto al motore a combustione interna. L'utilizzo della pila a combustibile di tipo PEM come principale fonte dei veicoli ibridi elettrici può rappresentare il futuro dell'industria automobilistica. L'interfaccia tra la cella a combustibile e il motore elettrico è costituito da un convertitore CC/CC e da un inverter trifase. In questo lavoro, viene presentato il convertitore "Multidevice interleaved boost converter (MDIBC)" che è responsabile di aumentare e regolare la tensione dal PEMFC al DC-link. Il convertitore proposto è confrontato con altre due topologie di convertitori: il "Interleaved boost converter (IBC)" e il "Multidevice boost converter (MDBC)". Per le tre topologie, le equazioni del modello di piccolo segnale e il design della strategia di controllo a doppio loop sono dimostrate e illustrate utilizzando MATLAB e Simulink.

**Parole chiavi:** Veicoli elettrici ibridi; CC/CC convertitori; modello di piccolo segnale, due loop controllo.

# ABSTRACT

The interest in hybrid electric vehicles (HEV) is growing, not only because of environmental impact in the transportation sector, but also because they are becoming economically attractive regarding the cost of driving and maintenance when compared to internal combustion engine. The use of PEM fuel cell (PEMFC) as a main source of HEV can represent the future of the automotive industry. The link between the fuel cell and the electric motor is made by a DC/DC converter and a three-phase inverter. In this work, it is presented a unidirectional multidevice interleaved boost converter (MDIBC) which is responsible to increase and regulate the voltage from the PEMFC to the DC-link. The proposed converter is compared to other two converter topologies: the interleaved boost converter (IBC) and the multidevice boost converter (MDBC). For the three topologies, the equations of the small signal model and the design of dual loop control strategy are demonstrated and illustrated using MATLAB and Simulink.



**Key-words:** Hybrid electric vehicles; DC/DC converters; small signal model; dual loop control.

# LIST OF FIGURES

**Figure 1 –** Schematic block diagram of a BEV powertrain.....20

**Figure 2 –** Schematic block diagram of a HEV powertrain .....20

**Figure 3 –** Ragone plot of different storage systems .....21

**Figure 4 –** Global greenhouse gas emissions by sector, based on global emissions from 2010 .....26

**Figure 5** – U.S. national average of the source of electricity and the annual emissions per type of vehicle .....27

**Figure 6 –** California State average of the source of electricity and the annual emissions per type of vehicle .....28

**Figure 7** – Missouri State average of the source of electricity and the annual emissions per type of vehicle .....28

**Figure 8 –** Generic electric block diagram of the fuel cell powertrain.....30

**Figure 9 –** Electric circuit of the Multidevice Interleaved Boost Converter (MDIBC) .30

**Figure 10 –** MDIBC gate sequence for the controllable switches when the duty cycle $d$ is 0.25.....33

**Figure 11 –** MDIBC Gate sequence for the controllable switches when the duty cycle $d$ is 0.10.....34

**Figure 12 –** MDIBC Gate sequence for the controllable switches when the duty cycle $d$ is 0.40.....35

**Figure 13 –** MDIBC Gate sequence for the controllable switches when the duty cycle (d) is 0.50 .....36

**Figure 14 –** Position of poles and zeros of the transfer function $iLsds$ .....45

**Figure 15 –** Position of poles and zeros of the transfer function $vosds$.....45

**Figure 16 –** MDIBC Bode diagram transfer function of $iLsds$ and $vosds$ .....46

**Figure 17 –** MDIBC Bode diagram of normalized transfer function $iLsds$ .....46

**Figure 18 –** MDIBC Bode diagram of normalized transfer function $vosds$ .....47

**Figure 19 –** Absolute value of zeros and poles as function of the load resistance $(R)$ .....47

**Figure 20 –** Position of zeros and poles as function of the load resistance in the complex plane. .....48

**Figure 21 –** Electric circuit of the Two-Phase of Interleaved Boost Converter (IBC).51

**Figure 22 –** IBC Gate sequence for the controllable switches when the duty cycle $d$ is 0.40.....51

**Figure 23 –** Position of poles and zeros of the transfer function $iLsds$ .....58

**Figure 24 –** Position of poles and zeros of the transfer function $vosds$.....59

**Figure 25 –** IBC Bode diagram of the inductor current and output voltage .....59

**Figure 27 –** IBC Bode diagram of output voltage normalized – unit gain.....60

**Figure 28 –** Electric circuit of the Multidevice boost converter (MDBC) .....61

**Figure 29 –** MDBC Gate sequence for the controllable switches when the duty cycle $d$ is 0.40.....61

**Figure 30 –** Position of poles and zeros of the transfer function $iLsds$ for the MDBC .....67

**Figure 31 –** Position of poles and zeros of the transfer function $vosds$ for the MDBC .....67

**Figure 32 –** MDBC Bode diagram of the inductor current and output voltage.....68

**Figure 33 –** MDBC Bode diagram of inductor current normalized – unit gain.....69

**Figure 34 –** MDBC Bode diagram of output voltage normalized – unit gain .....69

**Figure 35 –** Dual loop control strategy adopted. .....71

**Figure 36 –** Inner loop control – current inductor control .....72

**Figure 37 –** Simplification of the inner loop control.....74

**Figure 38 –** $kpI\ vs.\varphi mI$ and $kiI\ vs.\varphi mI$ – MDIBC.....76

**Figure 39 –** $kpV\ vs.\varphi mV$ and $kiV\ vs.\varphi mV$ – MDIBC .....77

**Figure 40 –** $kpI\ vs.\varphi mI$ and $kiI\ vs.\varphi mI$ – IBC .....78

**Figure 41 –** $kpV\ vs.\varphi mV$ and $kiV\ vs.\varphi mV$ – IBC.....78

**Figure 42 –** $kpI\ vs.\varphi mI$ and $kiI\ vs.\varphi mI$ – MDBC.....79

**Figure 43 –** $kpV\ vs.\varphi mV$ and $kiV\ vs.\varphi mV$ – MDBC .....80

**Figure 44 –** Transfer function GI – MDIBC .....81

**Figure 45 –** Open loop LI(s) and closed loop KI(s) transfer functions – MDIBC .....81

**Figure 46 –** Transfer function GV – MDIBC.....82

**Figure 47 –** Open loop LV(s) and closed loop KV(s) transfer functions – MDIBC.....82

**Figure 48 –** Transfer function GI – IBC.....83

**Figure 49 –** Open loop LI(s) and closed loop KI(s) transfer functions – IBC.....83

**Figure 50 –** Transfer function GV – IBC .....84

**Figure 51 –** Open loop LV(s) and closed loop KV(s) transfer functions – IBC .....84

**Figure 52 –** Transfer function GI – MDBC .....85

**Figure 53 –** Open loop LI(s) and closed loop KI(s) transfer functions – MDBC .....85

**Figure 54 –** Transfer function GV – MDBC.....86

**Figure 55 –** Open loop LV(s) and closed loop KV(s) transfer functions – MDBC.....86

**Figure 56 –** Electric circuit of the MDIBC in Simulink.....87

**Figure 57 –** Regulator block.....87

**Figure 58 –** Start logic for the drive gate signal .....88

**Figure 59 –** Controller diagram MDIBC in Simulink .....88

**Figure 60 –** Anti-windup PI controller.....89

**Figure 61 –** Electric circuit of the IBC in Simulink .....90

**Figure 62 –** Controller diagram MDIBC in Simulink .....90

**Figure 63 –** Electric circuit of the IBC in Simulink .....91

**Figure 64 –** Controller diagram MDIBC in Simulink .....91

**Figure 65 –** $vo$ vs. t (orange curve) and $vo\ ref$ vs. t (blue curve) for the MDIBC .....91

**Figure 66 –** $vo$vs. t (orange curve) and $vo\ ref$ vs. t (blue curve) for the MDIBC in steady state condition for the MDIBC .....92

**Figure 67 –** $id\ vs.t$ (green curve), $iL1vs.t$ (blue curve) and $iL2vs.t$ (orange curve) for MDIBC.....94

**Figure 68 –** $iL1vs.t$ (blue curve) and $iL2vs.t$ for MDIBC (orange curve) for MDIBC 94

**Figure 69 –** $id\ vs.t$ for MDIBC .....94

**Figure 70 –** $vo$vs.t (orange curve) and $vo\ ref$ vs.t (blue curve) for the IBC in steady state condition .....95

**Figure 71 –** $id\ vs.t$ (green curve), $iL1vs.t$ (blue curve) and $iL2vs.t$ (orange curve) for IBC .....95

**Figure 72 –** $iL1vs.t$ (blue curve) and $iL2vs.t$ for MDIBC (orange curve) for IBC.....96

**Figure 73 –** $id\ vs.t$ for IBC.....96

**Figure 74 –** $vo$vs.t (blue curve) and $vo\ ref$ vs.t (orange curve) for the MDBC in steady state condition.....97

**Figure 75 –** $id\ vs.t$ for MDBC .....97

# LIST OF TABLES

**Table 1 –** Description of the MDIBC conduction of the IGBTs and diodes and load situation when duty cycle $d$ is 0.25 during one period .....33

**Table 2 –** Description of the MDIBC conduction of the IGBTs and diodes and load situation when duty cycle $d$ is 0.10 during one period .....34

**Table 3 –** Description of the MDIBC conduction of the IGBTs and diodes and load situation when duty cycle $d$ is 0.40 during one period .....35

**Table 4 –** Description of the MDIBC conduction of the IGBTs and diodes and load situation when duty cycle $d$ is 0.50 during one period .....37

**Table 5 –** Steady state value of $IL$ and $Vo$ for MDIBC .....43

**Table 6 –** Value of the converter components.....43

**Table 7 –** Position of the zero and poles of the state equations in the MDIBC .....44

**Table 8 –** Converter type identification through the value of number of phases $n$ and the number of parallel legs per phase ($m$).....50

**Table 9 –** Description of the IBC conduction of the IGBTs and diodes and load situation.....52

**Table 10 –** Steady state value of $IL$ and $Vo$ for IBC.....57

**Table 11 –** Position of the zero and poles of the state equations in the IBC.....58

**Table 12 –** Description of the MDBC conduction of the IGBTs and diodes and load situation.....62

**Table 13 –** Steady state value of $IL$ and $Vo$ for MDBC .....66

**Table 14 –** Position of the zero and poles of the state equations in the MDBC .....66

**Table 15 –** Efficiency and converter losses.....70

**Table 16 –** Values of current and voltage cut-off frequency for each converter type.75

**Table 17 –** Value of the controller proportional and integral parameters $kpI, kiI\ kpV, kiV$ for the MDIBC when $\varphi mI = 60\ deg$, $\varphi mV = 70\ deg$ .....76

**Table 18 –** Value of the controller proportional and integral parameters $kpI, kiI\ kpV, kiV$ for the IBC when $\varphi mI = 60\ deg$, $\varphi mV = 60\ deg$.....77

**Table 19 –** Value of the controller proportional and integral parameters $kpI, kiI\ kpV, kiV$ for the MDBC when $\varphi mI = 70\ deg$, $\varphi mV = 70\ deg$ .....79

**Table 20 –** Output voltage, total current and inductor current ripple for each topology .....98

# CONTENTS

1. INTRODUCTION ..... 18

1.1 Description of the multidevice interleaved boost converter ..... 18

1.2 Chapters into which the subject is divided ..... 19

1.3 History of electric vehicles ..... 19

1.4 Description of the state of art ..... 20

2. ELECTRIC VEHICLES AND THEIR ROLE IN THE SOCIETY ..... 25

3. THE CONVERTER ..... 30

3.1 Proposed converter ..... 30

3.2 Switching power converter ..... 32

3.3 Small signal model ..... 37

3.4 Current ripple in fuel cells and batteries ..... 48

4. OTHER CONVERTERS ..... 50

4.1 Two-phase interleaved boost converter (IBC) ..... 50

4.1.1 Switching power converter ..... 51

4.1.2 Small signal model ..... 52

4.2 Multidevice boost converter (MDBC) ..... 61

4.2.1 Switching power converter ..... 61

4.2.2 Small signal model ..... 62

5. LOSSES ..... 70

6. SWITCHING POWER CONTROL ..... 71

6.1 Inner loop control ..... 72

6.2 Outer loop control ..... 74

7. SIMULATION AND RESULTS ..... 87

8. CONCLUSION ..... 99

9. REFERENCE ..... 100

# 1. INTRODUCTION

The electric vehicles are gaining popularity, not only because of environmental impact of the transportation sector, such as climate change and urban pollution, but also because they are convenient, quiet; it is for the advance of technology in batteries, converters and electric motors they are becoming economically attractive since their overall cost of maintenance and driving are cheaper when compared with the internal combustion engine. Electric vehicles are reliable, safe and comfortable, turning it into an interesting solution for our daily commuting. On the other hand, electric vehicle still has to face with some problems as high purchase cost, long charging time – around one hour – and lack of fuelling infrastructure which could represent an obstacle for long range trip.

In some decades, however, concerning the public policies that are being announced from different countries, internal combustion vehicles will no longer be able to drive inside the city centre, therefore electric and hybrid vehicles will gradually substitute them. The obsolescence of internal combustion vehicles will soon become more evident.

## 1.1 Description of the multidevice interleaved boost converter

In this work, it is presented the design and control of unidirectional multidevice interleaved boost converter that interfaces an energy storage system, and a DC link (or a DC bus) that can be used in a battery electric vehicle (BEV) or a hybrid electric vehicle (HEV) powertrain. This converter may have several applications due to its performance and useful electric properties, such as low input current and output voltage ripple and a necessity of decreased size and weight of the passive components. Moreover, the converter controlling is not as cumbersome as other practical solutions presented in this type of applications, e.g. Z – source inverter. In this case, the converter was conceived to increase the voltage from the energy storage system (e.g. fuel cell), connected in the converter input. Another role of the converter would be the regulation of the output voltage, which means that the output voltage should be a constant value, e.g. 400V, at any moment. This regulation must be achieved by means of the proposed control.

For the sake of comparison, the multidevice interleaved boost converter will be compared with similar other converters: two-phase interleaved boost converter (IBC) and a multidevice boost converter (MDBC), in terms of the switching power converter pattern, bode plot response, losses and value of passive components. These comparisons will be made by means of calculations, plotting and simulations in MATLAB and Simulink.

## 1.2 Chapters into which the subject is divided

This work is formed by seven main chapters organized as follows. In this chapter it is presented an overview of what the work is about and the history of the electric car and the trending technology of power converter for automotive applications. Then, in the next chapter, it is discussed the role and the future of electric vehicles in the society. In chapter three, it is deeply understood the proposed converter concerning the circuitry, the drive gate signals and the small signal model is also presented. Moreover, some details about energy storage system are also considered in this part. The study of similar converters such as the two-phase interleaved boost converter (IBC) and the multidevice boost converter (MDBC) is analysed in chapter four. In the next chapter, it is investigated the losses in different converters presented in chapters three and four. The switching power control is presented in chapter six. Finally, in chapter seven it is validated the study by illustrating the simulation and results.

## 1.3 History of electric vehicles

According to the official website of U.S. Department of Energy [1], the history of electric vehicles starts in the 18$^{th}$ century when researches from Hungary, Netherlands and the United States of America proposed a concept of battery-powered vehicle. However, the interest in this type technology starts in the 1970s with soaring oil prices and gasoline shortages. In that time, the technology available for electric vehicles were not competitive specially with respect to a limited performance when compared to internal combustion cars. The range was limited to a few tens of kilometres before the necessity of another recharge, while the top speed was limited to 70 kilometres per hour. Then, only in the end of 20$^{th}$ century, with the development of technologies around batteries and the microelectronic, a decisive moment came with the release of the first mass produced hybrid electric car, the Toyota Prius in 1997 in Japan. However, it became a success when it was released worldwide in the end of the year 2000. In

2006, another turning point, that brought a new concept around electric car, was the announcement of a Silicon Valley start-up, Tesla motors, that would start producing luxury electric sport-cars that could range, with only one recharge, 200 miles. Since then, other electric car brands start to release new electric vehicles with different technologies, such as, in 2010, the first commercially available plug-in hybrid electric vehicles (PHEVs). Nonetheless, it is important to point that the spread of electric was only possible in the countries whose government have invested in charging infrastructure and contributed with tax initiatives.

### 1.4 Description of the state of art

The structure of the powertrain (i.e. the intervening mechanism by which power is transmitted from an engine to a propeller or axle that it drives, [2]) of electric vehicles is usually composed of four main elements: one or more electric storage systems which have the function of a power source, a DC/DC converter that regulates the voltage of a DC bus, a DC/AC inverter and the electric motor. The figures 1 and 2 show the block diagram of a battery electric vehicle (BEV) and of hybrid electric vehicle (HEV) respectively.

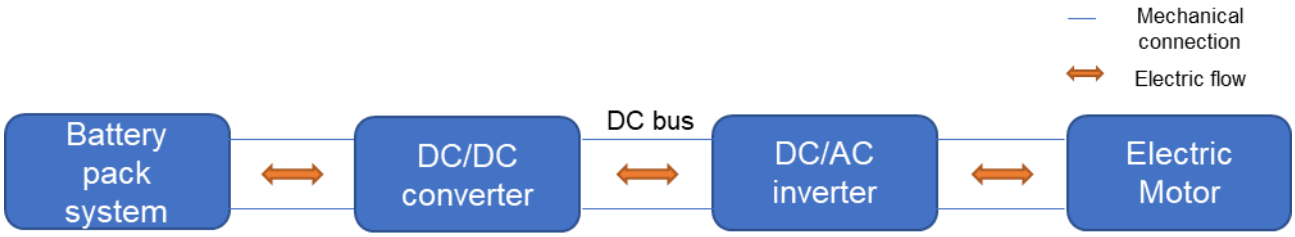


**Figure 1 –** Schematic block diagram of a BEV powertrain

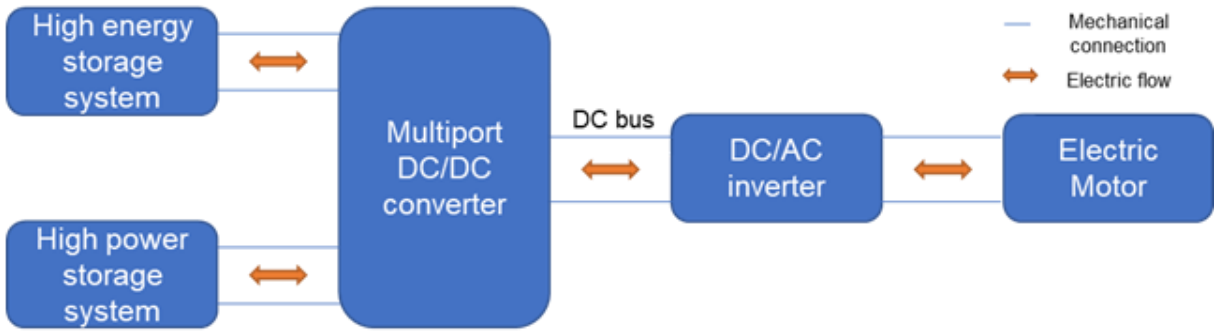


**Figure 2 –** Schematic block diagram of a HEV powertrain

**Note:** In case the high energy storage system is a fuel cell, the double arrow, that represents the electric flow becomes a right arrow, due to fuel cells electric unidirectional behaviour.

In the literature, some researches propose that powertrains should be fed by different sources in order to exploit the strong features from them. Usually, these sources present different characteristics: the main source is a high energy element, which has the main function of feeding a common DC bus and consequently providing enough energy to keep the electric motor working. On the other hand, the main aim of secondary or auxiliary sources is assisting the main source during transient periods and instantaneous peak power demand, such as acceleration. Hence, these auxiliary sources should provide a high amount of energy during a short period, which means that they must present as main characteristic a high-power density. The combination of these two different storage systems not only make available energy and power capabilities, therefore achieving a desired performance, but also this hybridization helps to improve the life span of the main source [3], [4].

There are many arrangements possible to integrate different storage systems based on their characteristics, the relation of power and energy density of different storage systems can be seen in the “Ragone Plot”, figure 3.

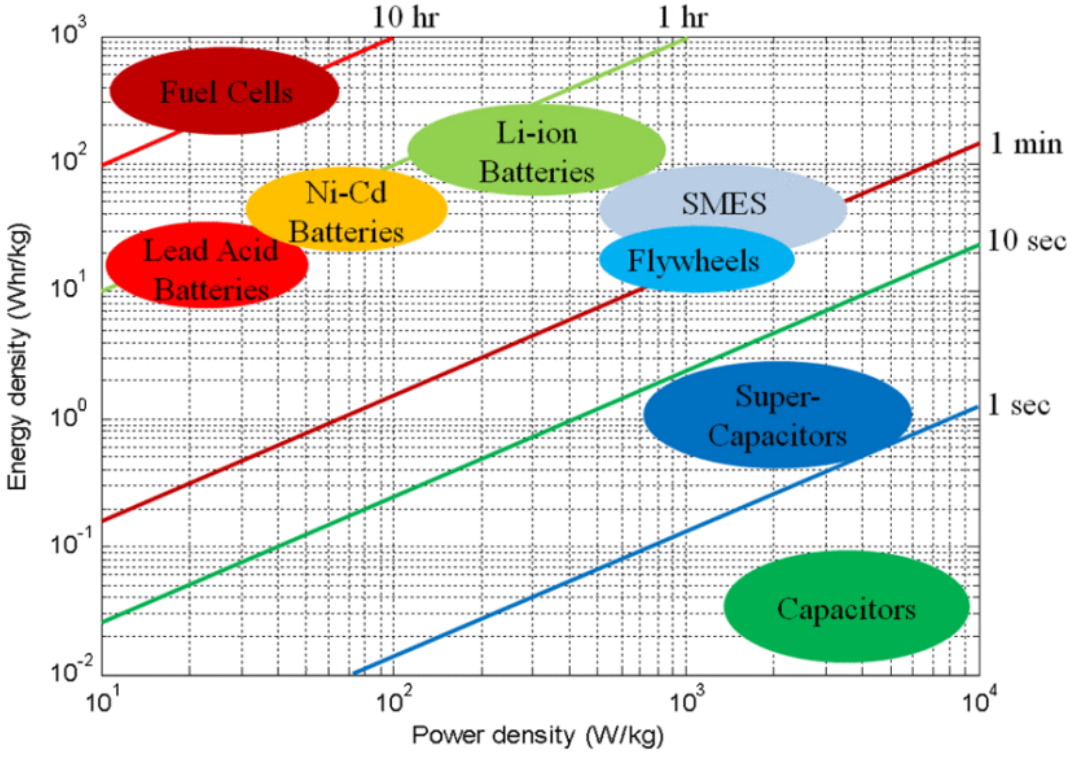


**Figure 3 –** Ragone plot of different storage systems

**Source:** J. W. Shim, Y. Cho, S. Kim, S. W. Min and K. Hur, "Synergistic Control of SMES and Battery Energy Storage for Enabling Dispatchability of Renewable Energy Sources," in *IEEE Transactions on Applied Superconductivity*, vol. 23, no. 3, pp. 5701205-5701205, June 2013, Art no. 5701205. [6]

From the figure 3, it is possible that, for example, the Li-ion Batteries are a type of storage system with a high energy density and average power density, when compared with the others storage systems. Hence, a possible configuration as a source for the powertrain would be the use of only this type of storage system, which would configure a battery electric vehicle (BEV) as proposed in [5]. Even if the use of only one type of storage system could be a practical solution, it would imply a large battery pack, which means an increase of volume, weight and cost. These increases could represent constraints in order to make the electric vehicle more efficient and market acceptable. On the other hand, the use of two complementary different sources can overcome the power deficiency at a lower volume, weight and cost. Some authors propose a hybridization that consists in batteries as main sources and ultracapacitors ([3] - [7]) or supercapacitors [4] as auxiliary source. Other authors have also proposed a fuel cell hybrid electric vehicle [8]: in this case, the fuel cell would be the main source and another energy storage system, such as a Li-ion battery, would aid the first source.

According to [4], to downsize the storage system, e.g. the battery pack, a low voltage (LV) source is connected to a DC bus through a DC/DC converter. As the DC bus voltage characteristic is higher than the output voltage of the storage system, the main function of the DC/DC converter is to increase and regulate the voltage in the DC bus. The main improvement of this choice is, in case of a bidirectional converter, the ability to recover more energy from the DC-link during the regenerative braking than HV source that is directly connected to the DC bus.

The converter that interfaces the DC bus and the energy storage system is a keystone in order to combine the properties of two different sources.

There are several ways to do the DC/DC converter, the simplest one is the use of boost converter. In [7], the authors have proposed a similar solution, in which parallel buck-boost converters are used: the boost configuration is used when the vehicle is in traction mode, otherwise the buck mode is used during regenerative braking. Moreover, the input of each converter is different, in this case ultracapacitor and battery. It is also possible to use variations of the boost converter, such as two-phase

interleaved boost converter (IBC), as proposed in [9] concerning a ripple cancellation of the two different phases. Other possible configuration that is also mentioned in the literature is the multidevice boost converter (MDBC) which by analogy is compared to IBC. The multidevice interleaved boost converter (MDIBC) is a configuration that combines the properties of IBC and MDBC configurations; thus it can enjoy advantages from both configurations, for example reducing the sizes and weight of passive components, low input current and low output voltage ripples and high-power factor.

Regarding the DC/AC inverter there are two interesting solutions that could represent the future in electric vehicles. The first one is a Z-source inverter, as proposed in [10]. This solution would have the role not only as an inverter, but also as a buck-boost converter, which means that the Z-source inverter would interface the battery and the motor without the need of the two stages of conversion. The necessity of only one stage of conversion implies a lower number of components, therefore a lower size and cost when compared to the two-stage solution. However, as mentioned in [5], the drawbacks in this configuration must be considered in the design circuit process, the most cumbersome are the high current and voltage stress, the necessity of a complex control and a limit boost ratio. The second solution is proposed in [11] and used in [5] and [8]; it is a bidirectional DC/AC converter made of eight switches, by this reason the solution name is eight switches inverter. This converter can work in four different modes: it can work as a three-phase AC/DC inverter when the motor is working in traction mode, as a three-phase DC/AC rectifier in case of regenerative braking and two other single-phase modes that relates the onboard battery and the power from the grid.

The last element of the block diagram of electric vehicle, as shown in the figures 1 and 2, is the electric motor. In spite of controlling AC motors precisely, the articles [5] and [11] proposed two possible strategies, the first, and also the most popular, is the indirect field oriented control (IFOC) in which the flux and torque currents are decoupled and controlled through vector control; however, for a constant rotor flux, it features poor efficiency of the motor at low load. Hence, in the interest of optimizing the efficiency of the induction motor, they have proposed an IFOC based on particle

swarm optimization (PSO). The PSO, in this case, is used to assess the optimal flux that minimizes the total losses.

# 2. ELECTRIC VEHICLES AND THEIR ROLE IN THE SOCIETY

The concerns about climate change have become an issue to be solved for the world community due to not only significant impact in the earth's climate but also due to severe consequences in the public health and economic implications. In 1979, the humanity took the first step, as an international concern, to combat the climate change through the First World Climate Conference. In this conference the World Climate Program was established which gave the guidelines in climate research, monitoring, applications and impact assessment, as written in the "World Meteorological Organization" website [12]. The same program was reviewed and refocused in the Second World Climate Conference in 1990. Since then, a lot of effort was put from several countries in order to propose agreements and milestones for the future years: as reference, it is possible to cite the Kyoto Protocol in 1997 and the Paris Agreement in 2015. The Paris Agreement, for example, was able to join 195 nations into the mutual cause of combating climate change through investments and public policies towards a sustainable future. According to United Nations Climate Change webpage [13], "The Paris Agreement central aim is to strengthen the global response to the threat of climate change by keeping a global temperature rise this century well below 2 degrees Celsius above pre-industrial levels and to pursue efforts to limit the temperature increase even further to 1.5 degrees Celsius. Additionally, the agreement aims to strengthen the ability of countries to deal with the impacts of climate change. To reach these ambitious goals, appropriate financial flows, a new technology framework and an enhanced capacity building framework will be put in place, thus supporting action by developing countries and the most vulnerable countries, in line with their own national objectives. The Agreement also provides for enhanced transparency of action and support through a more robust transparency framework."

In the same direction, some countries have announced severe public policies regarding internal combustion vehicles. In France, by 2040 petrol and diesel vehicles no longer will on be sale. Norway, country in which around 40% of the sales in 2016 were electric or hybrid, is planning that in 2025 all new passenger vehicle must be zero-emissions. Other European countries such as Germany, Spain and Netherlands, or non-European such as China and India are planning aggressive polices aiming at the hybrid and electric vehicles as a solution of the gases prevenient from the transportation sector.

The transportation sector is responsible for 14% of the global greenhouse gas emissions, according to the data Climate Change 2014: Mitigation of Climate Change, as shown in the figure 4.

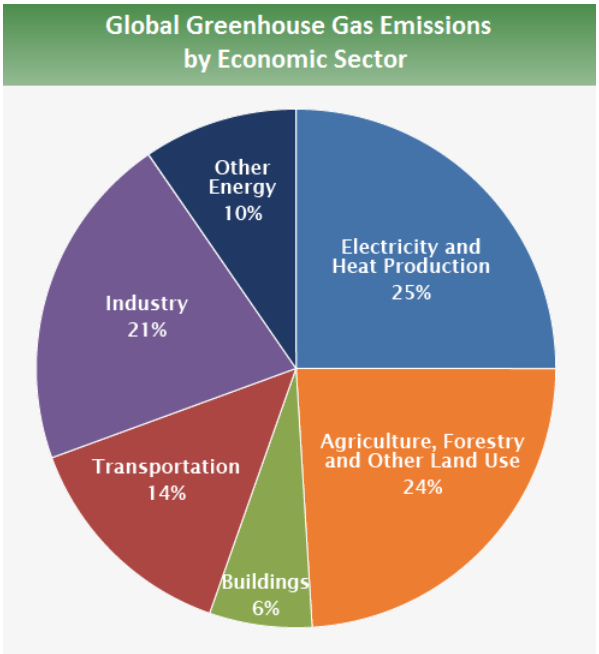


**Figure 4 –** Global greenhouse gas emissions by sector, based on global emissions from 2010

**Source:** "Global Greenhouse Gas Emissions Data". United States Environmental Protection Agency. Available in: https://www.epa.gov/. Access in: November 16th, 2018. [14]

There are two different classes of vehicle emissions, as mentioned in [15]. The first category is the direct emission that come directly from the evaporation from the fuel system and during the fuelling process. It also includes smog-forming pollutants, other pollutants harmful to human health and greenhouse gases. The second category is the life cycle emissions, that is related to fuel and vehicle production, processing, distribution, use and recycling or disposal. It is important to notice that electric vehicles do not cause direct emissions. Moreover, as the life cycle emission is variable since it depends on the energetic matrix in which the vehicle and the fuel is produced, the produced emission of any type of vehicle also varies as the production location changes. The calculation of the life cycle emission is quite cumbersome, due to the several variables to be considered. However, in the U.S. Department of Energy – Energy Efficiency & Renewable Energy website, it is possible to visualize the annual emission per vehicle as a national average or concerning each state, as the electricity

sources change, therefore a deeply analysis becomes easier to be made. Examples regarding the national, the California State and the Missouri State annual emissions average per vehicle are shown in the figures 5, 6 and 7 respectively.

Comparing the figures 6 and 7, it is possible to understand that all electric vehicles are worth it, considering only the annual emissions per vehicle. In the California State, where 47.53% of the produced energy comes from renewable sources (hydro, solar, wind, geothermal and Biomass), all electric vehicles have a lower annual emission when compared to the other types of vehicle. On the other hand, in the state of Missouri, where 79.80% of the produced electricity comes from coal, a non-renewable energy, all electric and plug-in hybrid vehicles present an annual emission per vehicle higher than hybrid vehicles. All electric vehicles in the State of Missouri can emit around three times more than the State of California. Hence, as shown in the figure 5, as a national average the order of the least to the higher emitter are all electric, plug-in hybrid and hybrid vehicles, the same sequence happen in the California State, but it is different for the Missouri State, where hybrid vehicles are less emitter than the all-electric and plug in hybrid.

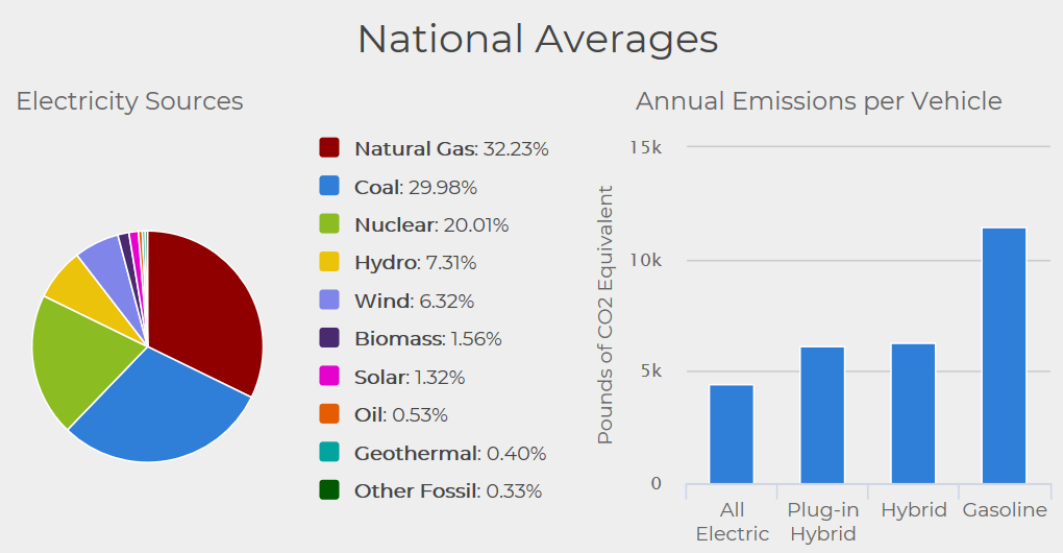


**Figure 5** – U.S. national average of the source of electricity and the annual emissions per type of vehicle

**Source:** "Alternative Fuels Data Center - Emissions from Hybrid and Plug-In Electric Vehicles". U.S. Department of Energy. Available in: https://www.energy.gov/. Access in: November 16th, 2018. [16]

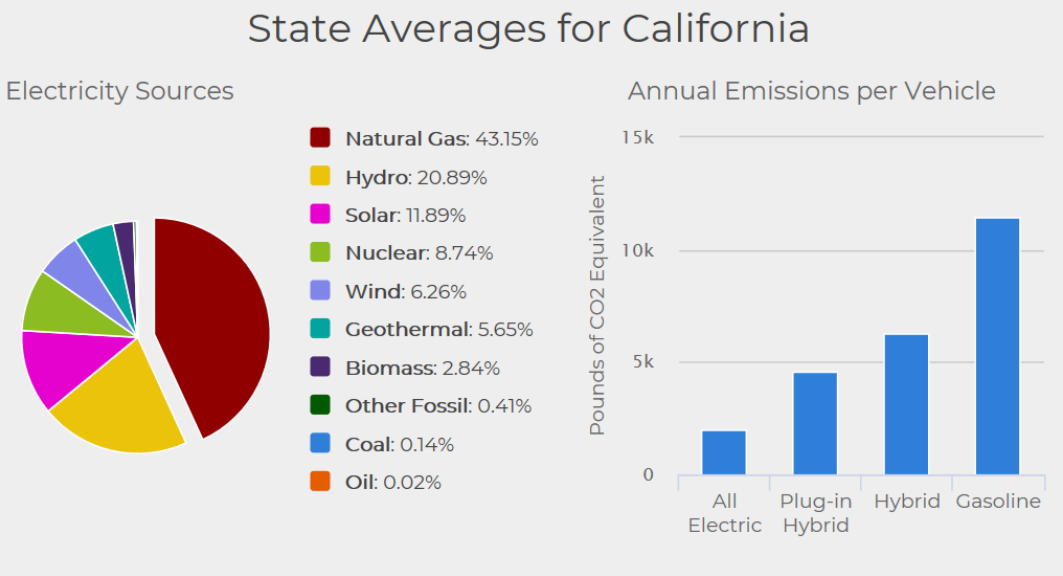


**Figure 6 –** California State average of the source of electricity and the annual emissions per type of vehicle

**Source:** "Alternative Fuels Data Center - Emissions from Hybrid and Plug-In Electric Vehicles". U.S. Department of Energy. Available in: https://www.energy.gov/. Access in: November 16th, 2018. [16]

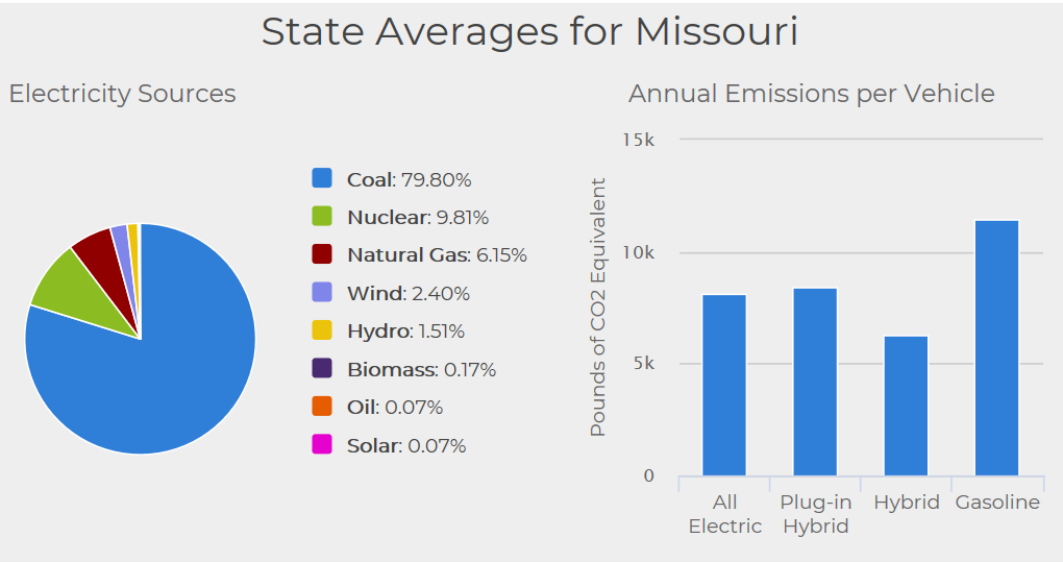


**Figure 7** – Missouri State average of the source of electricity and the annual emissions per type of vehicle

**Source:** "Alternative Fuels Data Center - Emissions from Hybrid and Plug-In Electric Vehicles". U.S. Department of Energy. Available in: https://www.energy.gov/. Access in: November 16th, 2018. [16]

In a study [17] supported by New England University Transportation Center at Massachusetts Institute of Technology (MIT), named “Can today’s EVs make a dent in climate change?”, have reached a conclusion that electric vehicles can make the difference for a sustainable future. According to the study, even if the car must be recharged at least once a day (e.g. probably overnight) in the United States of America, around 90% of personal vehicles necessity in the United States could be met by a “low-cost electric vehicle on the market today”, considering the overall cost of the vehicle and distance range. That is because technology regarding the distance range of the electric vehicle and batteries not only are becoming cheaper, but also it has already overcome the travelled distance of daily commute. This replacement would represent a reduction of 30% in the emissions of the transportation sector and would meet the climate objective targets for personal vehicle travel considering the current energetic matrix of the country. If the United States energetic sources turn into the direction of cleaner and renewable energy, the reduction percentual has the tendency to increase.

## 3. THE CONVERTER

The proposed converter studied in this paper is the unidirectional Multidevice Interleaved Boost Converter (MDIBC), based in [8]. It is a DC/DC converter used to increase the voltage that come from the energy storage system. In this work it is presented a hybrid electric powertrain, where the main source is a Fuel Cell and the auxiliary source is a battery. As the converter is a unidirectional converter, it cannot be used to recover energy from the regenerative braking, then it is suitable for energy storage systems that cannot absorb electric energy from their output terminals.

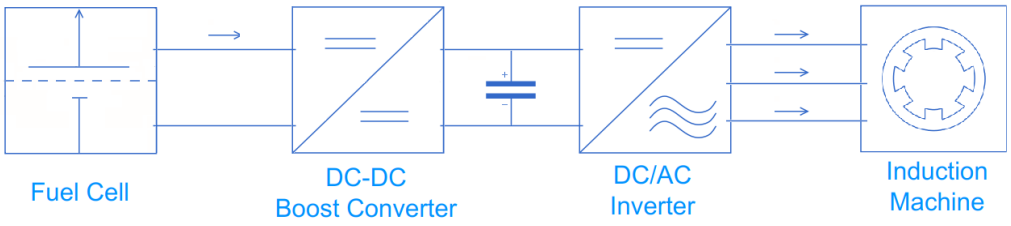


**Figure 8 –** Generic electric block diagram of the fuel cell powertrain

It is assumed that the load current is ripple free, the proposed converter operates in the continuous conduction mode (CCM) and the switches have identical duty cycles ($d_1 = d_2 = d_3 = d_4$).

### 3.1 Proposed converter

The electric circuit of the unidirectional multidevice interleaved boost converter (MDIBC) is presented in the figure 9.

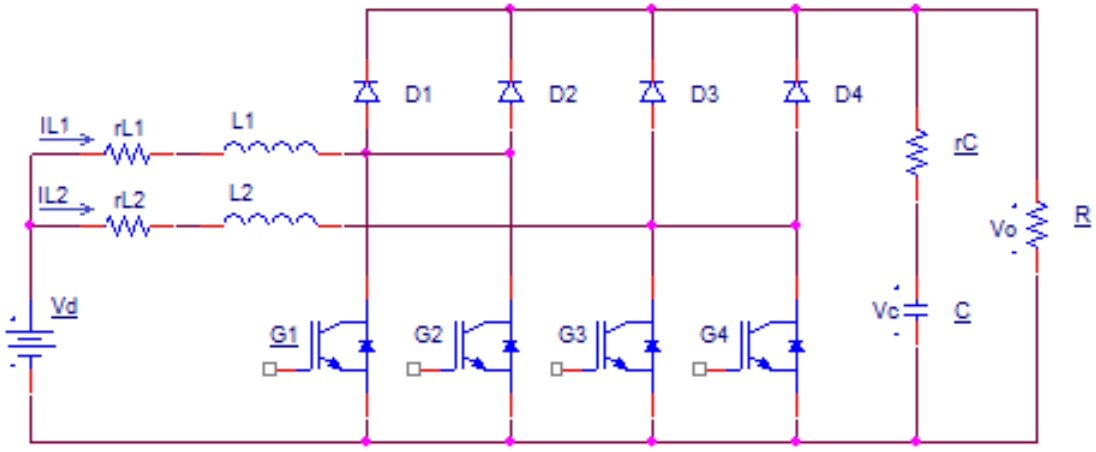


**Figure 9 –** Electric circuit of the Multidevice Interleaved Boost Converter (MDIBC)

The converter is composed of one voltage source, two phases, four legs of diodes in series of IBGTs, a shunt capacitor and the load. Each phase is connected to the same source – through an inductor. From each phase there are two legs of diodes in series with a controllable switch. For example, the first phase ($r_{L1}$ and $L_1$) is connected to $D_1$, $G_1$, $D_2$, $G_2$. The second phase ($r_{L2}$ and $L_2$) is connected to the remaining components (to $D_3$, $G_3$, $D_4$, $G_4$). It is important to notice that the load, represented by a resistance $(R)$, is the DC bus which is connected to a DC/AC inverter that supplies the electric motor (not represented in figure 8). In case of a HEV, connected to the DC link would be the output of another MDIBC.

The circuit presented in the figure 9 can only conduct current from the source to the load, therefore the source cannot absorb energy from the load in order to recharge the source, situation that would happen in case of regenerative braking.

The use of a DC/DC converter is related to the size reduction of the storage system. Theoretically, a high voltage source could be directly connected to the DC/AC inverter, however, it would demand a battery of considerable size which would imply an additional cost. A practical solution (cheaper and lighter) is the use of a low voltage source connected to a DC/DC converter to increase and regulate the voltage value of the DC bus.

The proposed converter, MDIBC, besides the step-up property, for the same switching frequency, increases the inductor current and the output voltage ripple frequency. This frequency increment contributes to a higher system bandwidth and consequently a faster dynamic response for the converter [8]. In order to obtain an increased frequency ripple and a phase-shift interleaved control the gate signal sequence must be chosen properly. Considering that $m$ is the number of parallel power switches per channel and $n$ is the number of channels or phases, the gate sequence for the controllable switches is shifted by $\frac{360^o}{nm}$. The input current ripple and output voltage ripple $mn$ times of the switching frequency. Therefore, according to [8], a reduction of $m$ times in the size of the passive components is expected when the proposed converter is compared with the $n$-phase interleaved DC/DC converters. The reduction of passive components is a key element for the reduction of size, cost and weight of the power converter, as the passive components – specially the power

inductor – are the heaviest components, hence it is preferable a small inductance value in the interest of achieving the size and weight wanted.

Finally, another converter property is the following: if phase-shift interleaved control is used, the sum of the current ripple in both phases results in ripple cancellation, which means that the ripple in energy storage system will be lower than expected when this solution is compared to a non-phase-shift interleaved control.

## 3.2 Switching power converter

As mentioned previously, the drive gate signal sequence is important to achieve a phase-shift interleaved control. In the figure 10, it is shown the gate signal pattern when the duty cycle $(d)$ is equal to 0.25. When the duty cycle assumes this value, as there are four controllable switches, at any moment during one period, there is at least an IGBT conducting. Table 1 describes which IGBT and diodes are conducting during one period and the load situation - powered or not - in each time interval. It is important to notice that the reference name for the diodes are shown in the figure 9.

Next graphs (figures 11, 12 and 13) show the drive gate signals in three different cases, when the duty cycle is equal to 0.1, 0.4 and 0.5. The description of which switches (diodes and IGBTs) are conducting and the load situation is shown in the tables 2, 3 and 4 respectively.

In the first case $(d = 0.1)$, as the duty cycle is lower than 0.25, there are only two possible situations: no switch is powered or only one switch is conducting. Therefore, the load at any interval is being powered. In the second case $(d = 0.4)$, when the duty cycle is greater than 0.25, there are also two different situations: only one switching is conducting or an overlapping of gate signals from different phases. In the first situation, the load is fed as in the previous cases, but when there are two switches from different phases conducting in the same time, the current does not feed the load. The third case, when the duty cycle is $(d = 0.5)$, at any time interval there is an overlapping between switches from different phases, then, the load cannot be fed. This last case is the boundary value that duty cycle can assume. Hence the duty cycle interval is $0 < d < 0.5$.

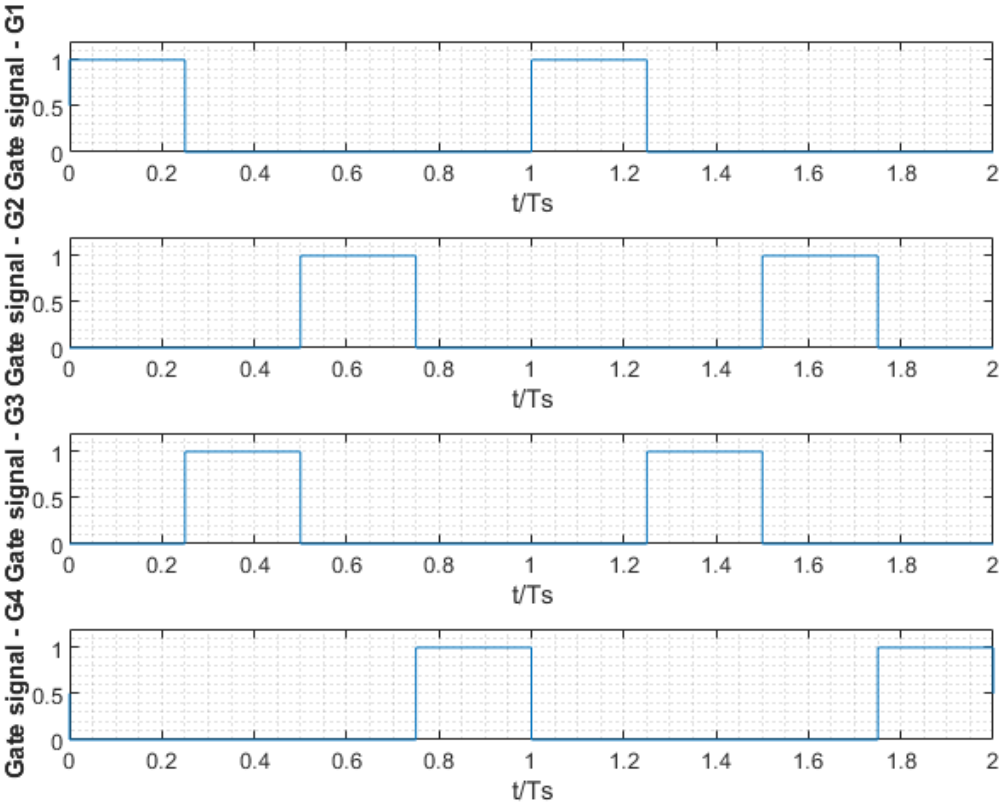


**Figure 10 –** MDIBC gate sequence for the controllable switches when the duty cycle $(d)$ is 0.25

**Table 1 –** Description of the MDIBC conduction of the IGBTs and diodes and load situation when duty cycle $(d)$ is 0.25 during one period

| Time instant | IGBT | Diode | Load |
|---|---|---|---|
| $0 < {}^{t}/_{Ts} < 0.25$ | $G_1$ is conducting | $D_3$, $D_4$ are conducting | Powered |
| $0.25 < {}^{t}/_{Ts} < 0.50$ | $G_3$ is conducting | $D_1$, $D_2$ are conducting | Powered |
| $0.50 < {}^{t}/_{Ts} < 0.75$ | $G_2$is conducting | $D_3$, $D_4$ are conducting | Powered |
| $0.75 < {}^{t}/_{Ts} < 1$ | $G_4$ is conducting | $D_1$, $D_2$ are conducting | Powered |

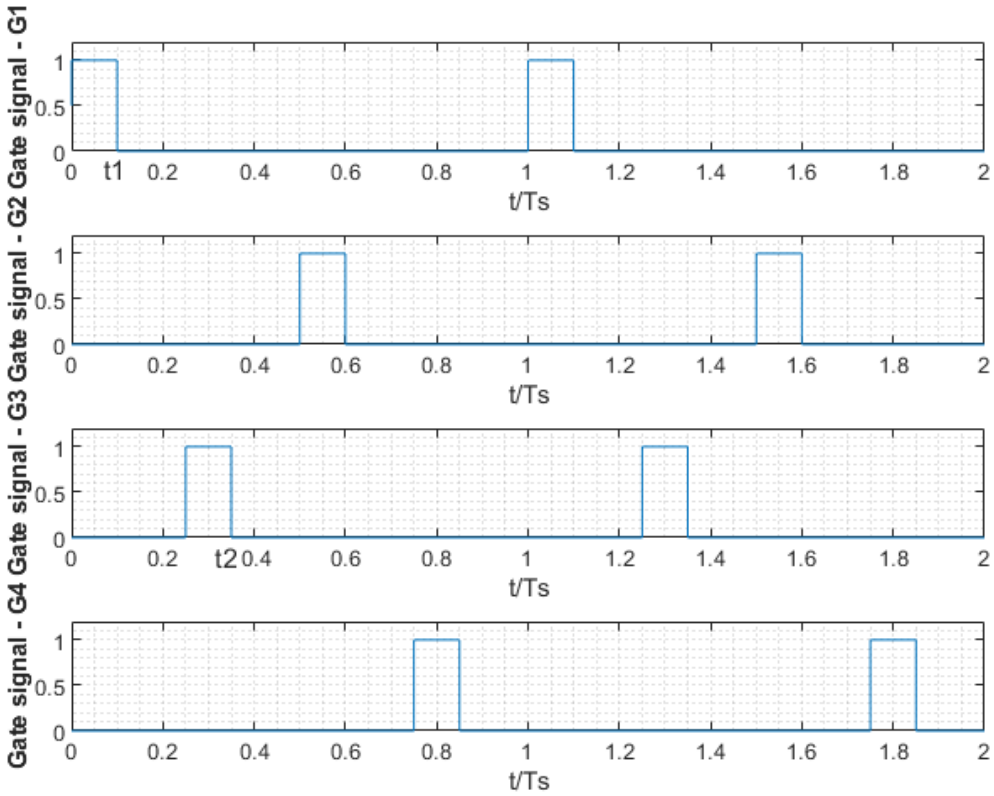


**Figure 11 –** MDIBC Gate sequence for the controllable switches when the duty cycle $(d)$ is 0.10

**Table 2 –** Description of the MDIBC conduction of the IGBTs and diodes and load situation when duty cycle $(d)$ is 0.10 during one period

| Time instant | IGBT | Diode | Load |
|---|---|---|---|
| $0 < {}^{t}/_{Ts} < 0.10$ | $G_1$ is conducting | $D_3$, $D_4$ are conducting | Powered |
| $0.10 < {}^{t}/_{Ts} < 0.25$ | None | $D_1$, $D_2$, $D_3$, $D_4$ are conducting | Powered |
| $0.25 < {}^{t}/_{Ts} < 0.35$ | $G_3$ is conducting | $D_1$, $D_2$ are conducting | Powered |
| $0.35 < {}^{t}/_{Ts} < 0.50$ | None | $D_1$, $D_2$, $D_3$, $D_4$ are conducting | Powered |
| $0.50 < {}^{t}/_{Ts} < 0.60$ | $G_2$ is conducting | $D_3$, $D_4$ are conducting | Powered |

| | | | |
|---|---|---|---|
| $0.60 < {}^{t}/_{Ts} < 0.75$ | None | $D_1, D_2, D_3, D_4$ are conducting | Powered |
| $0.75 < {}^{t}/_{Ts} < 0.85$ | $G_4$ is conducting | $D_1$, $D_2$ are conducting | Powered |
| $0.85 < {}^{t}/_{Ts} < 1$ | None | $D_1$, $D_2$, $D_3$, $D_4$ are conducting | Powered |

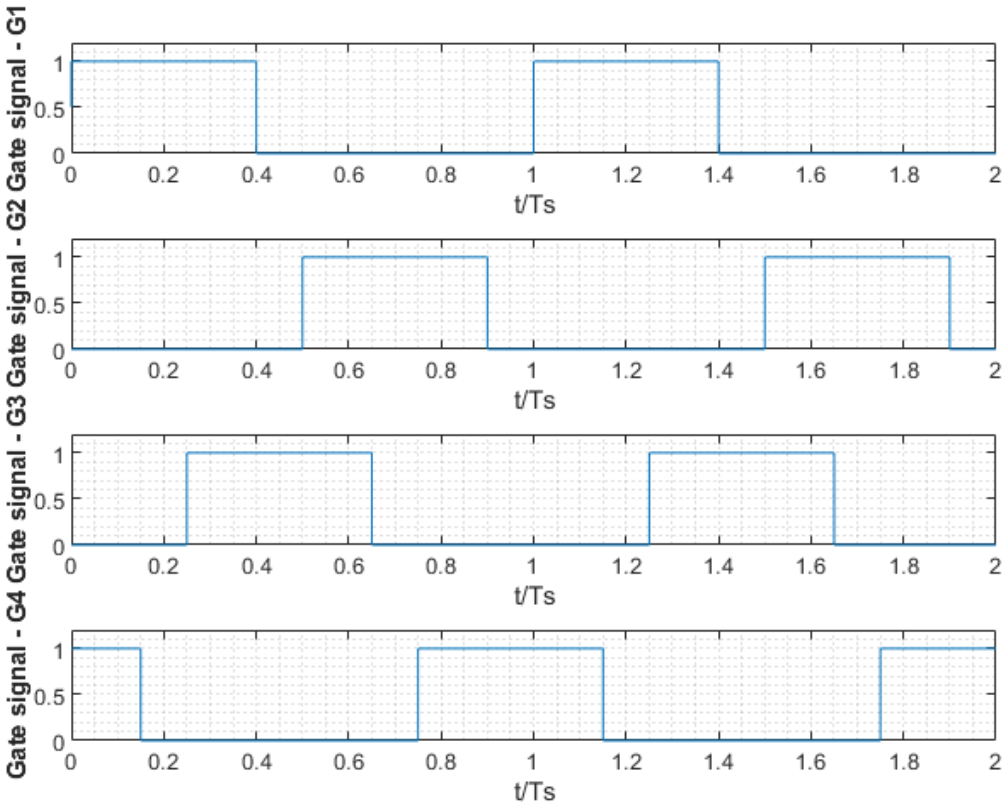


**Figure 12 –** MDIBC Gate sequence for the controllable switches when the duty cycle $(d)$ is 0.40

**Table 3 –** Description of the MDIBC conduction of the IGBTs and diodes and load situation when duty cycle $(d)$ is 0.40 during one period

| Time instant | IGBT | Diode | Load |
|---|---|---|---|
| $0 < {}^{t}/_{Ts} < 0.15$ | $G_4$, $G_1$ are conducting | None | Not powered |

| | | | |
|---|---|---|---|
| $0.15 < {}^{t}/_{Ts} < 0.25$ | $G_1$ is conducting | $D_3$, $D_4$ are conducting | Powered |
| $0.25 < {}^{t}/_{Ts} < 0.40$ | $G_1$, $G_3$ are conducting | None | Not powered |
| $0.40 < {}^{t}/_{Ts} < 0.50$ | $G_3$ is conducting | $D_1$, $D_2$ are conducting | Powered |
| $0.50 < {}^{t}/_{Ts} < 0.65$ | $G_3$, $G_2$ are conducting | None | Not powered |
| $0.65 < {}^{t}/_{Ts} < 0.75$ | $G_2$ is conducting | $D_3$, $D_4$ are conducting | Powered |
| $0.75 < {}^{t}/_{Ts} < 0.90$ | $G_2$, $G_4$ are conducting | None | Not powered |
| $0.90 < {}^{t}/_{Ts} < 1$ | $G_4$ is conducting | $D_1$, $D_2$ are conducting | Powered |

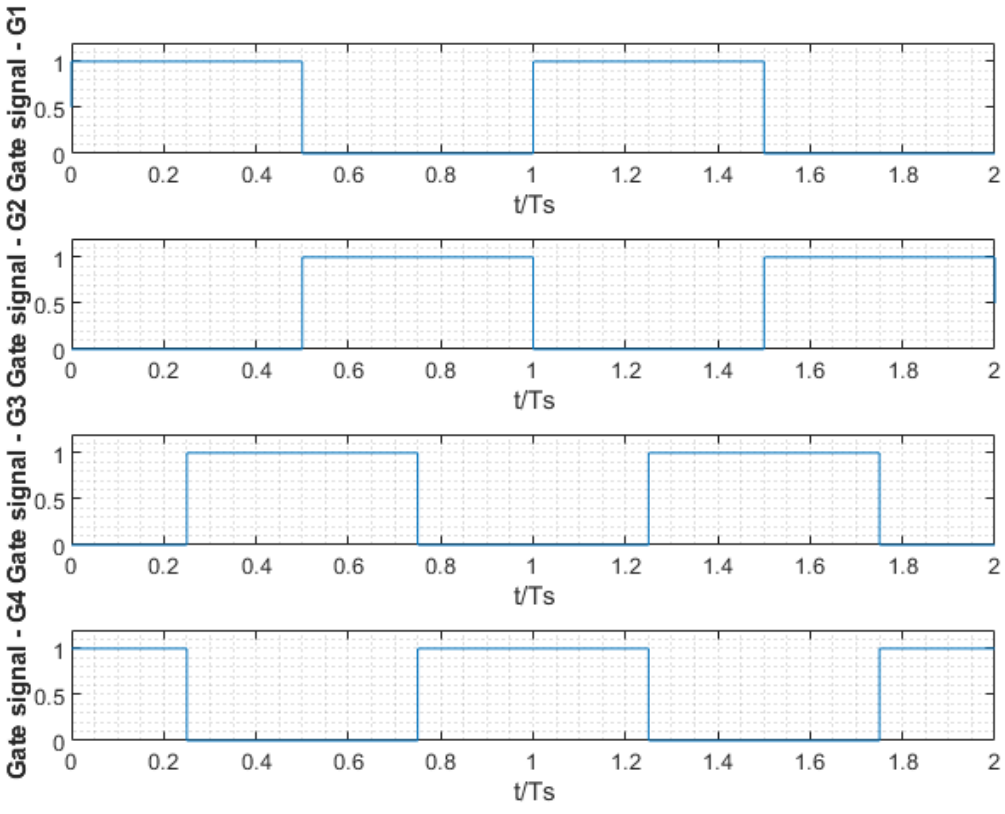


**Figure 13 –** MDIBC Gate sequence for the controllable switches when the duty cycle (d) is 0.50

**Table 4 –** Description of the MDIBC conduction of the IGBTs and diodes and load situation when duty cycle $(d)$ is 0.50 during one period

| Time instant | IGBT | Diode | Load situation |
|---|---|---|---|
| $0 < {}^{t}/_{Ts} < 0.25$ | $G_4$, $G_1$ are conducting | None | Not powered |
| $0.25 < {}^{t}/_{Ts} < 0.50$ | $G_1$, $G_3$ are conducting | None | Not powered |
| $0.50 < {}^{t}/_{Ts} < 0.75$ | $G_3$, $G_2$ are conducting | None | Not powered |
| $0.75 < {}^{t}/_{Ts} < 1$ | $G_2$, $G_4$ are conducting | None | Not powered |

### 3.3 Small signal model

The small signal model was found using the linearization of the power stage using state-space averaging as proposed in [18]. Considering the figures 9 and 11 as the electric circuit and gate signal pattern reference, a null value of capacitance resistance – the output voltage $(v_o)$ is equal to the voltage capacitor $(v_c)$ – it is possible to derive the small signal model. As shown in the table 2, during one period, there are eight possible states that the circuit can assume. However, as there are two switches per phase, the states started after the time interval $\frac{T_s}{m}$ are a repetition of the previous states. Moreover, the duty cycle of every controllable switch in the circuit is assumed identical, hence there are four possible states that the MDIBC can assume.

As can be seen in the figure 9, there are three energy storage passive elements in the circuit – two inductors and one capacitor – therefore, three equations are necessary to describe the circuit: one for each current inductor and another for the voltage capacitor.

The four possible states are described by means of the Kirchhoff voltage law (KVL) and Kirchhoff current law (KCL). Then, the system of equations is written in matrix form and the derivative of inductor current and voltage capacitor are isolated in the left side, i.e., in the same form as: $px = Ax + Bvd$, where $p$ is the derivative

operator, $A$ is a three by three matrix, $B$ is a three by one matrix, $t_1$ and $t_2$are, respectively, the time that the $G_1$ and $G_3$ go to zero.

- Case 1, $0 < t < t_1$, $r_c \approx 0$, $G_1$ is on:

$$\begin{cases} V_d - L.pi_{L1} - r_L.i_{L1} = 0 \\ V_d - L.pi_{L2} - r_L.i_{L2} - v_o = 0 \\ i_{L2} = C.pv_o + \dfrac{v_o}{R} \end{cases}$$

$$px_1 = A_1x_1 + B_1V_d$$

$$p\begin{pmatrix} i_{L1} \\ i_{L2} \\ v_o \end{pmatrix} = \begin{pmatrix} -\dfrac{r_L}{L} & 0 & 0 \\ 0 & -\dfrac{r_L}{L} & -\dfrac{1}{L} \\ 0 & \dfrac{1}{C} & -\dfrac{1}{RC} \end{pmatrix}\begin{pmatrix} i_{L1} \\ i_{L2} \\ v_o \end{pmatrix} + \begin{pmatrix} \dfrac{1}{L} \\ \dfrac{1}{L} \\ 0 \end{pmatrix}V_d \quad (1)$$

- Case 2, $t_1 < t < \frac{T_s}{4}$, $r_c \approx 0$:

$$\begin{cases} V_d - L.pi_{L1} - r_L.i_{L1} - v_o = 0 \\ V_d - L.pi_{L2} - r_L.i_{L2} - v_o = 0 \\ i_{L1} + i_{L2} = C.pv_o + \dfrac{v_o}{R} \end{cases}$$

$$px_2 = A_2x_2 + B_2V_d$$

$$p\begin{pmatrix} i_{L1} \\ i_{L2} \\ v_o \end{pmatrix} = \begin{pmatrix} -\dfrac{r_L}{L} & 0 & -\dfrac{1}{L} \\ 0 & -\dfrac{r_L}{L} & -\dfrac{1}{L} \\ \dfrac{1}{C} & \dfrac{1}{C} & -\dfrac{1}{RC} \end{pmatrix}\begin{pmatrix} i_{L1} \\ i_{L2} \\ v_o \end{pmatrix} + \begin{pmatrix} \dfrac{1}{L} \\ \dfrac{1}{L} \\ 0 \end{pmatrix}V_d \quad (2)$$

- Case 3, $\frac{T_s}{4} < t < t_2$, $r_c \approx 0$, $G_3$ is on:

$$\begin{cases} V_d - L.pi_{L1} - r_L.i_{L1} - v_o = 0 \\ V_d - L.pi_{L2} - r_L.i_{L2} = 0 \\ i_{L1} = C.pv_o + \dfrac{v_o}{R} \end{cases}$$

$$px_3 = A_3x_3 + B_3V_d$$

$$p\begin{pmatrix} i_{L1} \\ i_{L2} \\ v_o \end{pmatrix} = \begin{pmatrix} -\frac{r_L}{L} & 0 & -\frac{1}{L} \\ 0 & -\frac{r_L}{L} & 0 \\ \frac{1}{C} & 0 & -\frac{1}{RC} \end{pmatrix}\begin{pmatrix} i_{L1} \\ i_{L2} \\ v_o \end{pmatrix} + \begin{pmatrix} \frac{1}{L} \\ \frac{1}{L} \\ 0 \end{pmatrix} Vd \quad (3)$$

- Case 4, $t_2 < \mathrm{t} < \frac{\mathrm{T}_s}{2}$, $r_c \approx 0$:

$$\begin{cases} V_d - L.pi_{L1} - r_L.i_{L1} - v_o = 0 \\ V_d - L.pi_{L2} - r_L.i_{L2} - v_o = 0 \\ i_{L1} + i_{L2} = Cpv_o + \frac{v_o}{R} \end{cases}$$

$$px_4 = A_4x_4 + B_4V_d$$

$$p\begin{pmatrix} i_{L1} \\ i_{L2} \\ v_o \end{pmatrix} = \begin{pmatrix} -\frac{r_L}{L} & 0 & -\frac{1}{L} \\ 0 & -\frac{r_L}{L} & -\frac{1}{L} \\ \frac{1}{C} & \frac{1}{C} & -\frac{1}{RC} \end{pmatrix}\begin{pmatrix} i_{L1} \\ i_{L2} \\ v_o \end{pmatrix} + \begin{pmatrix} \frac{1}{L} \\ \frac{1}{L} \\ 0 \end{pmatrix} Vd \quad (4)$$

Described the state matrices, it is necessary to determine the average value of derivative $(p < x >)$ of the state variables. An index will be written in order to identify which case the matrices are from: for example, matrices A and B of the first case, will receive an index 1. As there are a repetition after $\frac{\mathrm{T}_s}{m}$, the integration interval is $0 < \mathrm{t} < \frac{\mathrm{T}_s}{m}$.

$$\mathrm{p} < \mathrm{x} >= \frac{1}{\frac{\mathrm{T}_s}{m}} \int_0^{\frac{\mathrm{T}_s}{m}} px.dt \quad (5)$$

Simplifying the notation, i.e., the $x = < x >$, and substituting the values of px:

$$\mathrm{px} = \frac{m}{\mathrm{T}_s}\left( \int_0^{t_1} px_1.dt + \int_{t_1}^{\frac{\mathrm{T}_s}{4}} px_2.dt + \int_{\frac{\mathrm{T}_s}{4}}^{t_2} px_3.dt + \int_{t_2}^{\frac{\mathrm{T}_s}{m}} px_4.dt \right) \quad (6)$$

The second switch starts to conduct at $\frac{Ts}{mn}$, the number four in the denominator is related to the number of switches in the circuit. Moreover, the number of switches is

related to the number of phases $n$ and to the number of parallel legs per phase $m$. Then, the integration interval is rewritten.

$$\mathrm{px} = \frac{m}{Ts}\left(\int_0^{d.T_s}(A_1x + B_1v_d).dt + \int_{dT_s}^{\frac{\mathrm{T}_s}{mn}}(A_2x + B_2v_d).dt + \int_{\frac{\mathrm{T}_s}{mn}}^{T_s(\frac{1}{mn}+d)}(A_3x + B_3v_d).dt + \int_{T_s(\frac{1}{mn}+d)}^{\frac{\mathrm{T}_s}{m}}(A_4x + B_4v_d).dt\right)$$

$$\mathrm{px} = \frac{m}{\mathrm{T}_s}\left((A_1x + B_1v_d).d\mathrm{T}_s + (A_2x + B_2v_d).\left(\frac{1}{mn} - d\right)\mathrm{T}_s + (A_3x + B_3v_d).d\mathrm{T}_s + (A_4x + B_4v_d).\left(\frac{1}{mn} - d\right)\mathrm{T}_s\right)$$

$$\mathrm{px} = m\left(\left((A_1 + A_3)d + \frac{1}{mn}(A_2 + A_4)(1 - mnd)\right)x + \left((B_1 + B_3)d + \frac{1}{mn}(B_2 + B_4)(1 - mnd)\right)v_d\right) \quad (7)$$

Introducing the separation of AC perturbation and DC component in the variables $x$, $d$. The letter tilde on top represents the AC perturbation and the capital letter the DC component. The input voltage is considered pure DC.

$$\begin{aligned} x &= \tilde{x} + X \\ d &= \tilde{d} + D \\ v_d &= V_d \end{aligned} \quad (8)$$

Substituting the equations in (8) in (7), after algebraic manipulations and neglecting higher order harmonics (e.g.: $\tilde{x}.\tilde{d} \approx 0$).

$$p\tilde{x} = m\left[\left((A_1 + A_3)D + \frac{1}{mn}(A_2 + A_4)(1 - mnD)\right)X + \left((B_1 + B_3)D + \frac{1}{mn}(B_2 + B_4)(1 - mnD)\right)V_d\right] + \left[\left((A_1 + A_3)D + \frac{1}{mn}(A_2 + A_4)(1 - mnD)\right)\tilde{x} + \left((A_1 + A_3 - A_2 - A_4)X + (B_1 + B_3 - B_2 - B_4)V_d\right)\tilde{d}\right] \quad (9)$$

The first bracket in the equation 9, is the steady state response of the circuit and, by definition, its value is zero. The matrices $B_1$, $B_2$, $B_3$ and $B_4$ are equal. Matrices

$A_2$ and $A_4$ are also equal, because they represent the state when there is no switch on, the sum of them is two times the value of $A_2$. In this case, as there are two identical matrices due to the fact that there are two-phases, it is also possible to substitute the value “2” by “n”. Considering these prepositions, (9) can be rewritten.

$$\begin{cases} p\tilde{x} = mA\tilde{x} + m(A_1 + A_3 - nA_2)X\tilde{d} \\ A = (A_1 + A_3)D + \dfrac{1}{m}A_2(1 - mnD) \end{cases} \tag{10}$$

Finally, performing the Laplace transform and isolating the AC perturbations in the left side, it is possible to find the transfer function of the state variables. The matrix “I” is the unit matrix and “s” is the Laplace variable.

$$\begin{cases} \dfrac{\tilde{x}(s)}{\tilde{d}(s)} = (sI - mA)^{-1}m(A_1 + A_3 - nA_2)X \\ A = (A_1 + A_3)D + \dfrac{1}{m}A_2(1 - mnD) \end{cases} \tag{11}$$

Substituting the values, it is possible to find the matrices values.

$$A = \begin{pmatrix} -\dfrac{r_L}{2L} & 0 & -\dfrac{1}{2L}(1-2D) \\ 0 & -\dfrac{r_L}{2L} & -\dfrac{1}{2L}(1-2D) \\ \dfrac{1}{2C}(1-2D) & \dfrac{1}{2C}(1-2D) & -\dfrac{1}{2RC} \end{pmatrix}$$

$$A_1 + A_3 - nA_2 = \begin{pmatrix} 0 & 0 & \dfrac{1}{L} \\ 0 & 0 & \dfrac{1}{L} \\ -\dfrac{1}{C} & -\dfrac{1}{C} & 0 \end{pmatrix}$$

In the matrix $X = (x_1 \quad x_2 \quad x_3)^t$, there are the steady state variables of the current inductors and the output voltage ($x_1 = I_{L1}$, $x_2 = I_{L2}$, $x_3 = V_o$) . This means that the transfer functions $\frac{\tilde{\imath}_L(s)}{\tilde{d}(s)}$ and $\frac{\tilde{v}_o(s)}{\tilde{d}(s)}$ solutions are going to be around the values in the matrix $X$. The current inductor steady state value (equation 12) is calculated considering that the output power $(P_o)$ is equal to the input power $(P_i)$ and the current inductor in both phases are the same. The steady state output voltage is calculated according to the equation 13, in which non-ideal characteristics are neglected.

$$\begin{cases} P_i = P_o \\ P_i = V_d I_{L1} + V_d I_{L2} \\ I_{L1} = I_{L2} = I_L \end{cases}$$

$$I_L = \frac{P_o}{2V_d} \tag{12}$$

$$V_o = \frac{V_d}{1 - mD} \tag{13}$$

Performing some algebraic calculations, it is found the small signal perturbation in the current inductor and the voltage capacitor.

- Current inductor transfer function:

$$G_{id}(s) = \frac{\tilde{\imath}_L(s)}{\tilde{d}(s)} = G_{di} \frac{\left(1 + \frac{s}{\omega_{zi}}\right)}{\Delta(s)} \tag{14}$$

$$\begin{cases} G_{di} = \dfrac{2(x_3 + (x_1 + x_2)(1 - 2D)R)}{r_L + 2R\left(1 - 4D(1 - D)\right)} \\ \omega_{zi} = \dfrac{x_3 + (x_1 + x_2)(1 - 2D)R}{RCx_3} \\ \Delta(s) = \dfrac{s^2}{\omega_0^2} + \dfrac{s}{Q\omega_0} + 1 \\ \omega_0 = \sqrt{\dfrac{r_L + 2R\left(1 - 4D(1 - D)\right)}{RLC}}, Q = \dfrac{\sqrt{RLC\left(r_L + 2R\left(1 - 4D(1 - D)\right)\right)}}{RCr_L + L} \end{cases}$$

- Output voltage state equation:

$$G_{vd}(s) = \frac{\tilde{v}_o(s)}{\tilde{d}(s)} = G_{dv} \frac{\left(1 - \frac{s}{\omega_{zv}}\right)}{\Delta(s)} \tag{15}$$

$$\begin{cases} G_{dv} = \dfrac{2R((1 - 2D)x_3 - (x_1 + x_2)r_L)}{r_L + 2R\left(1 - 4D(1 - D)\right)} \\ \omega_{zv} = \dfrac{2(1 - 2D)x_3 - r_L(x_1 + x_2)}{L(x_1 + x_2)} \end{cases}$$

The value of the input voltage $(V_d)$ is set to 200V and the output power $(P_o)$ to 30 KW. Therefore, considering the duty cycle (D) is 0.25, from the equations 12 and

13, it is possible to calculate the steady state values of $I_L$ and $V_o$, these values are shown in the table 5.

**Table 5 –** Steady state value of $I_L$ and $V_o$ for MDIBC

| Parameter | Value |
|---|---|
| $I_L$ (A) | 75 |
| $V_o$ (V) | 400 |

Two parameters were adopted to choose the components values, the maximum current inductor ripple allowed limited to 9% $\left(\frac{\Delta I_L}{I_L} < 9\%\right)$, and the maximum output voltage ripple limited to 1% $\left(\frac{\Delta V_o}{V_o} < 1\%\right)$. The equations (16) to (19) show the equations that calculate the output resistance $(R)$, the inductor $(L)$, the capacitor $(C)$ and the inductor resistance $(r_L)$. It is important to point out that the value of the inductor resistance was calculated considering a quality factor of $\mathrm{Q}|_{f_s=1500\,Hz} = 100$. The component values are described in the table 6.

$$R = \frac{V_o^2}{P} \tag{16}$$

$$L = \frac{V_{in} D}{f_s \Delta I_L} \tag{17}$$

$$C = \frac{D}{f_s R} \frac{V_o}{\Delta V_o} \tag{18}$$

$$r_L = \frac{\omega L}{Q} \tag{19}$$

**Table 6 –** Value of the converter components.

| Component | Value |
|---|---|
| L | 375 µH/180A |

| | |
|---|---|
| $r_L$ | 34 mΩ |
| C | 320 μF/500V |
| R | 5.33 Ω |

Therefore, in order to understand the transfer function shape and properties, the position of zeros and poles is calculated and described in the table 7. The roots of the numerator and the denominator gives the position of zero and poles respectively. The poles position is equal for both state variables, as their denominator transfer function are the same. Figures 14 and 15 illustrate the position of zero and poles in the complex plane, for the transfer functions $\frac{\tilde{\imath}_L(s)}{\tilde{d}(s)}$ and $\frac{\tilde{v}_o(s)}{\tilde{d}(s)}$.

**Table 7 –** Position of the zero and poles of the state equations in the MDIBC

| **Parameter** | **Value** |
|---|---|
| $Z_i$ | $-1172\,rad/s$ |
| $Z_v$ | $-6930\,rad/s$ |
| $P_1, P_2$ | $-338 \pm 2026j\ rad/s$ |
| $\|P_1\| = \|P_2\|$ | $2054\,rad/s$ |
| $\zeta$ | 0.1668 |

**Note:** Subscript description: $Z$ – zero, $P$ – pole, $i$ – inductor current, $v$ – output voltage, $\zeta$ - damping ratio.

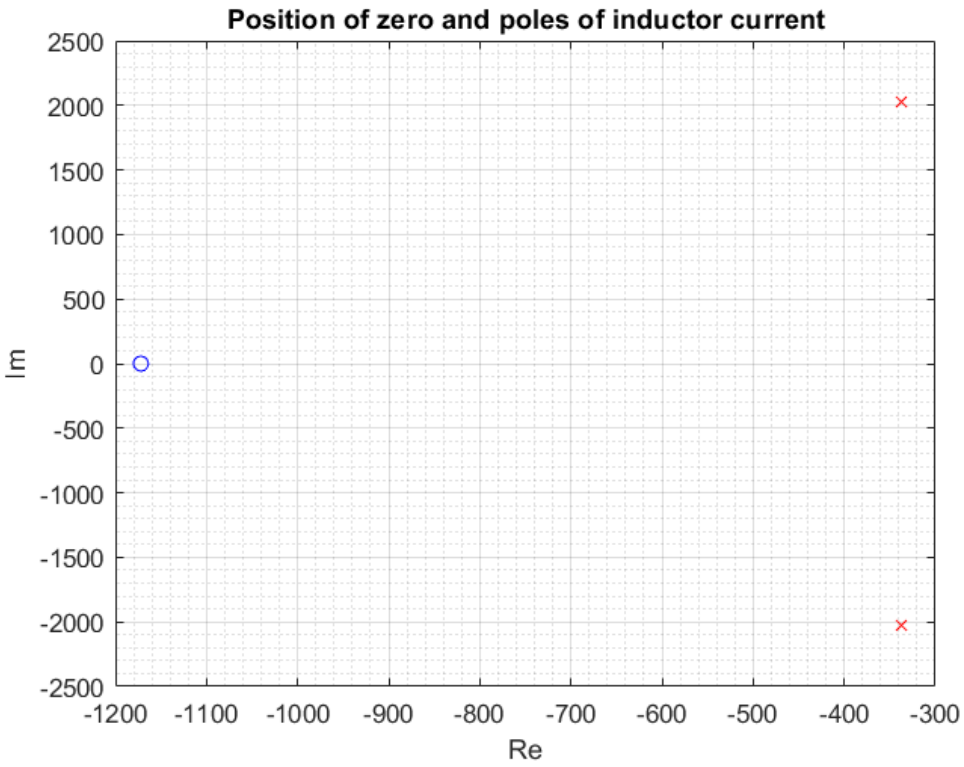


**Figure 14 –** Position of poles and zeros of the transfer function $\frac{\tilde{\imath}_L(s)}{\tilde{d}(s)}$

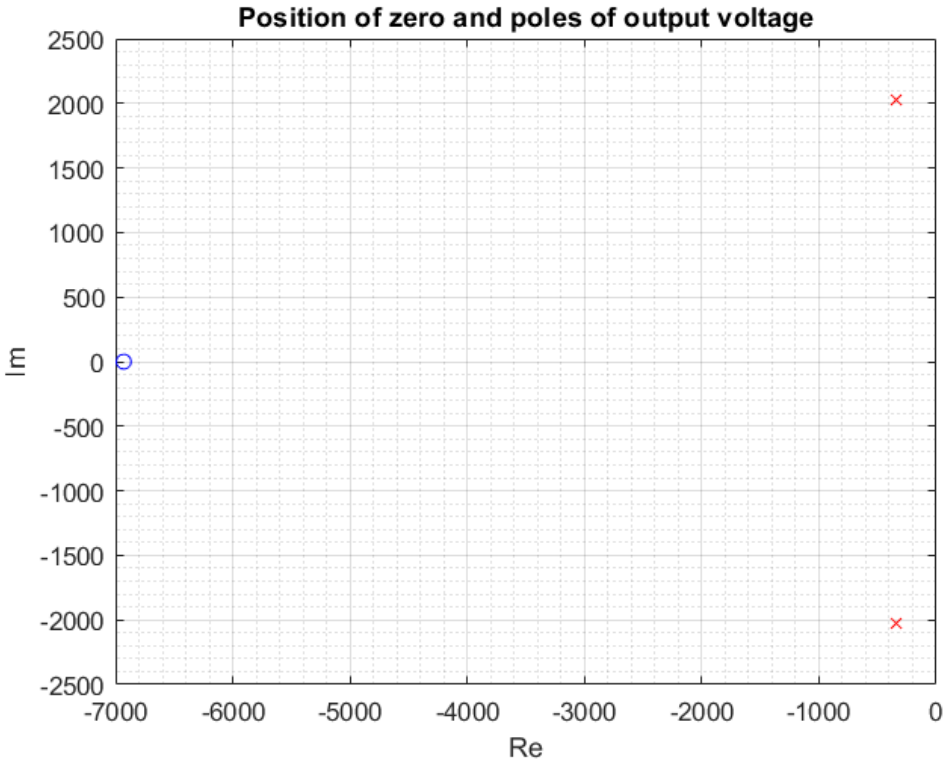


**Figure 15 –** Position of poles and zeros of the transfer function $\frac{\tilde{v}_o(s)}{\tilde{d}(s)}$

Figure 16 shows the Bode diagram of the $\frac{\tilde{\imath}_L(s)}{\tilde{d}(s)}$ (orange curve) and $\frac{\tilde{v}_o(s)}{\tilde{d}(s)}$ (blue curve).

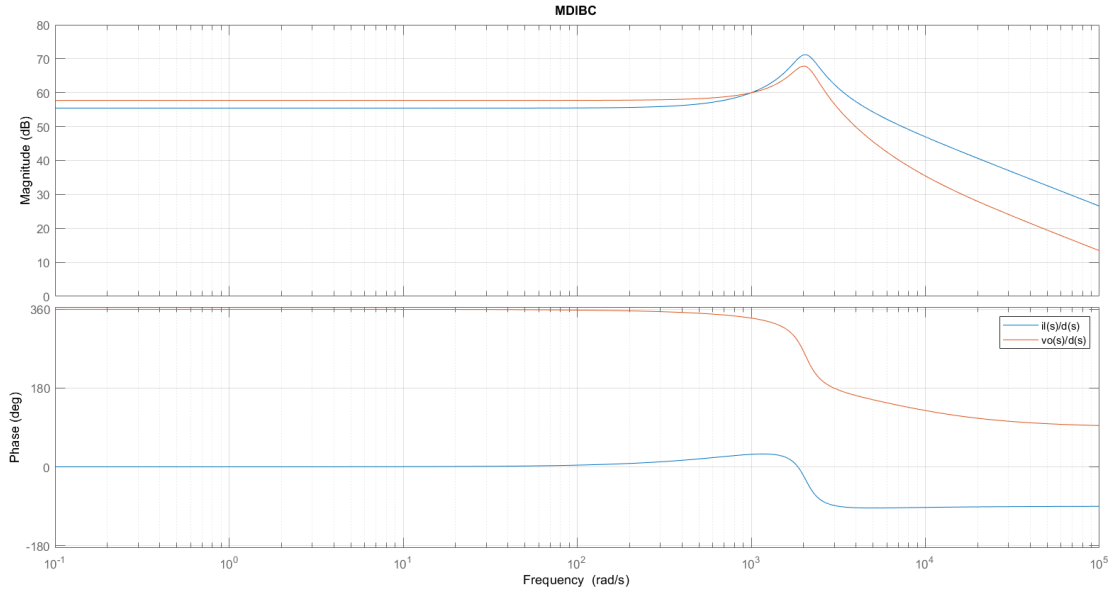


**Figure 16 –** MDIBC Bode diagram transfer function of $\frac{\tilde{\imath}_L(s)}{\tilde{d}(s)}$ and $\frac{\tilde{v}_o(s)}{\tilde{d}(s)}$

Figures 17 and 18 show the normalized Bode diagrams of $G_{id}(s)$ and $G_{vd}(s)$, i.e., $\frac{Gid(s)}{|Gdi|}$ and $\frac{Gvd(s)}{|Gdv|}$. In normalized plot functions, it is easier to identify the shape and properties of the system response.

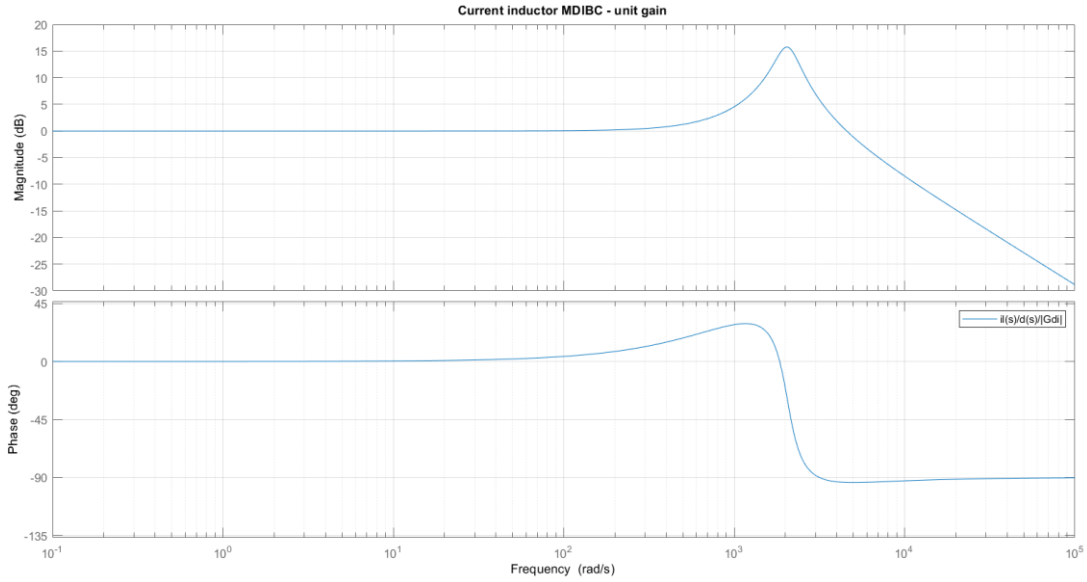


**Figure 17 –** MDIBC Bode diagram of normalized transfer function $\frac{\tilde{\imath}_L(s)}{\tilde{d}(s)}$

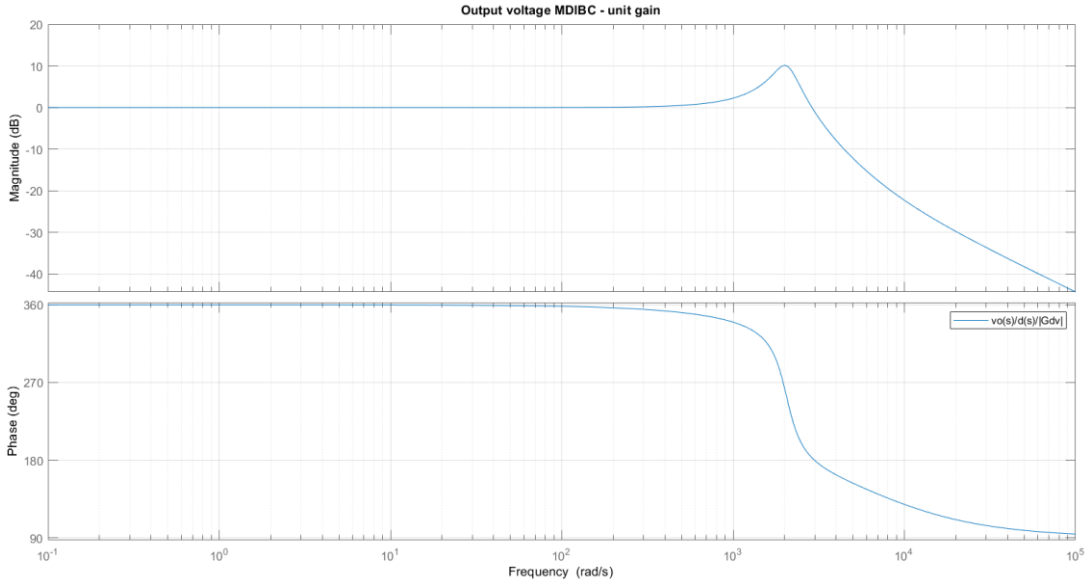


**Figure 18 –** MDIBC Bode diagram of normalized transfer function $\frac{\tilde{v}_o(s)}{\tilde{d}(s)}$

If the load resistance changes $(R)$, it can affect the transfer function response due to the position of current inductor zero and the poles are dependent on it. Figure 19 shows how the absolute value of zeros and poles changes when the load varies from $1\,\Omega$ to $1\,M\Omega$. Moreover, it is possible to notice that both parameters stop to increase when the load resistance reaches the value of $100\,\Omega$.

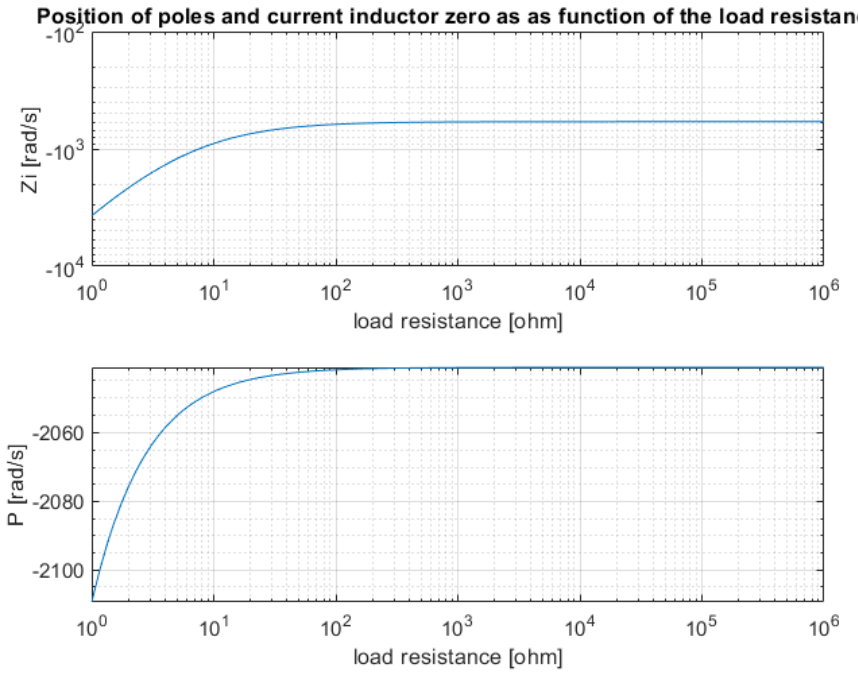


**Figure 19 –** Absolute value of zeros and poles as function of the load resistance $(R)$

It is important to point out that, according to (15), the position of the output voltage zero ($\omega_{zv}$) does not depend on the load resistance. The poles, when $1\,\Omega < \mathrm{R} < 1\,M\Omega$, are pairs of complex conjugate values, figure 20 shows the position of poles and zeros in the complex plane and, as higher is the load, their position is closer to the vertical axis ($s = 0$).

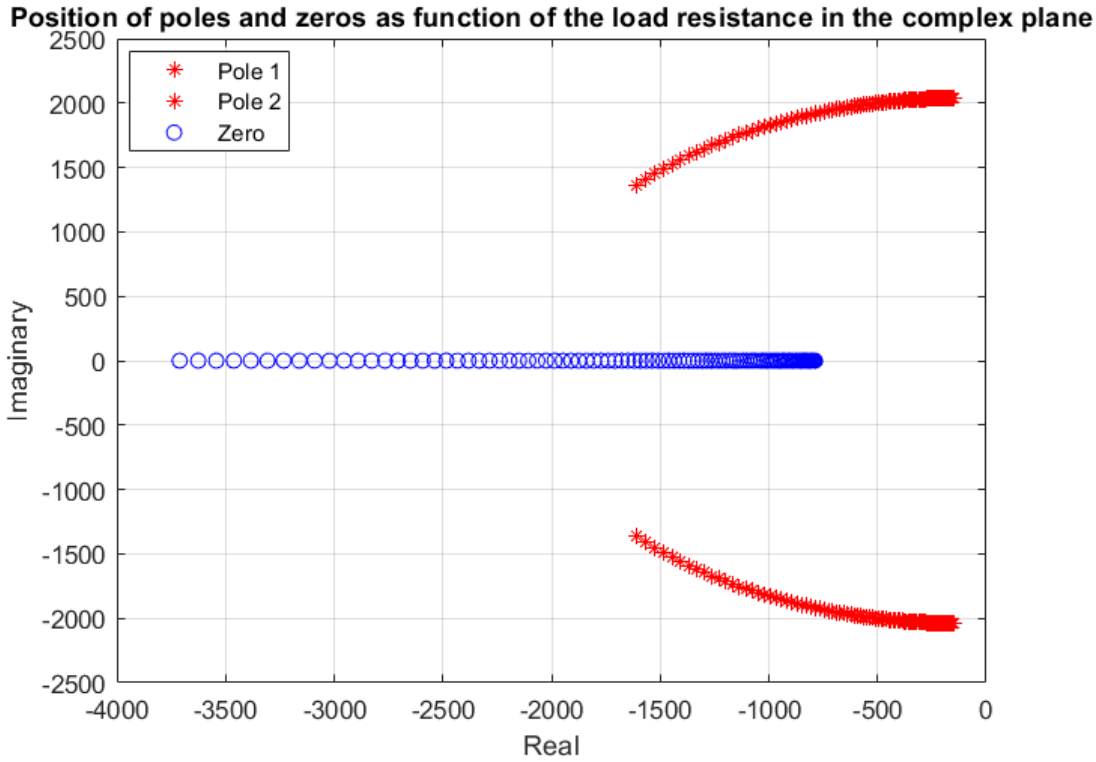


**Figure 20 –** Position of zeros and poles as function of the load resistance in the complex plane.

### 3.4 Current ripple in fuel cells and batteries

An important converter's property is, using the same switching frequency ($f_s$), to increase the frequency of inductor ripple current. A higher frequency of ripple current inductor has mainly two effects. The first effect is the size and weight reduction of the power inductor, as discussed previously. The other effect is related with the battery life span and efficiency [8].

According to the Schneider white paper [19], even if the effects of AC ripple voltage and current in the batteries are distinct, in excessive amounts, they represent a potential damage for the battery. The technical bulletin of C&D Technologies Inc., a battery manufacture [20], relates the AC ripple voltage and current with the

temperature rise. If the operating temperature is greater than the designed one, irreversible damage can occur. The total heat dissipated would be, then, generated from two different sources, not only the DC current, but also an AC ripple current resulting in an additional heating effect. Moreover, according to them, the higher the AC frequency ripple, the lower the impact in the battery.

Regarding the fuel cells, there are disagreements about the effects of current and voltage ripples. In [21], the authors conclude that the influence of current ripple in the inverter input (or fuel cell output) is insignificant when the efficiency is concerned. In [22], the authors could not find any evidence that current ripple – in the frequency range used – accelerate the deterioration of the fuel cells. In [23], differently, the authors could conclude that the reduction of the output power is related with the ripple current content, if the low frequency ripple content in the fuel cell is limited to 15% to 20%, the losses are lower than 1%.

# 4. OTHER CONVERTERS

In this chapter, two other converters topology are presented: the two-phase interleaved boost converter (IBC) and the multidevice boost converter (MDBC). Moreover, for these new converters, it is presented their electric circuit, the working principle when the gate signals are interleaved, the small signal model deduction and analysis. Their transfer function response curves are also shown.

The proposed converter – multidevice interleaved boost converter (MDIBC) – can be seen as the exploitation of the properties of both converters presented in this chapter – two phases and two parallel legs per phase. Reminding that $n$ is the number of phases and $m$ is the number of parallel legs per phase, it is possible to identify the converters studied in this work through the value of these numbers. Other converters types, not analysed in this work, can be also identified by changing the values of $n$ and $m$.

**Table 8 –** Converter type identification through the value of number of phases $(n)$ and the number of parallel legs per phase $(m)$

| **Converter** | **Phases** $(\boldsymbol{n})$ | **Parallel legs per phase** $(\boldsymbol{m})$ |
|---|---|---|
| MDIBC | 2 | 2 |
| IBC | 2 | 1 |
| MDBC | 1 | 2 |

In this chapter, it is also assumed that the converters operate in the continuous conduction mode (CCM), the switches have identical duty cycles and the duty cycle interval is $0 < \mathrm{d} < 0.5$.

## 4.1 Two-phase interleaved boost converter (IBC)

In this converter topology, there are two different phases and only one leg of diode in series with an IGBT per phase. In the output, parallel to the load, there is a shunt capacitor. The electric circuit of the two – phase interleaved boost converter is shown in the figure 21.

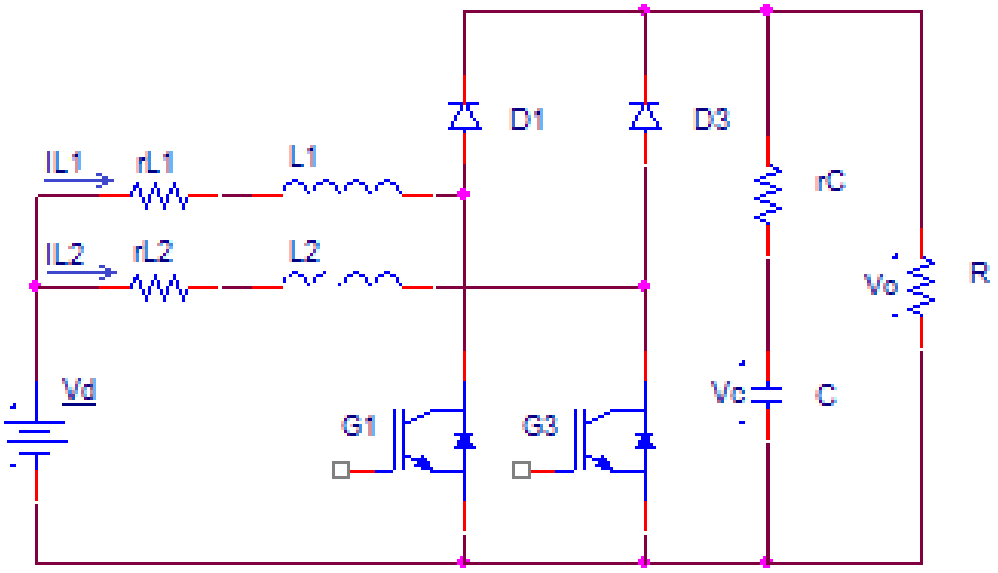


**Figure 21 –** Electric circuit of the Two-Phase of Interleaved Boost Converter (IBC)

### 4.1.1 Switching power converter

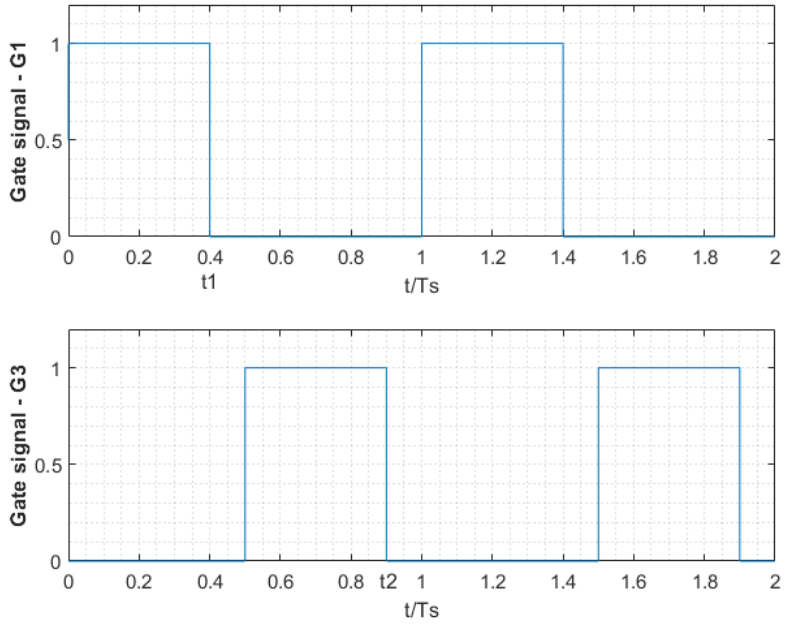


**Figure 22 –** IBC Gate sequence for the controllable switches when the duty cycle $(d)$ is 0.40

**Table 9 –** Description of the IBC conduction of the IGBTs and diodes and load situation the duty cycle $(d)$ is 0.40 during one period

| Time instant | IGBT | Diode | Load situation |
|---|---|---|---|
| $0 < {}^{t}/_{Ts} < 0.40$ | $G_1$ is conducting | $D_3$ is conducting | Powered |
| $0.40 < {}^{t}/_{Ts} < 0.50$ | None | $D_1$, $D_3$ are conducting | Powered |
| $0.50 < {}^{t}/_{Ts} < 0.90$ | $G_3$ is conducting | $D_1$ is conducting | Powered |
| $0.90 < {}^{t}/_{Ts} < 1$ | None | $D_1$, $D_3$ are conducting | Powered |

### 4.1.2 Small signal model

The small signal model procedure is derived similarly to the one presented in the previous chapter. Considering the electric circuit of the figure 21 and the gate signal pattern from the figure 22, the instants that the drive gate signals $\mathrm{G}_1$ and $\mathrm{G}_2$ become zero – $\mathrm{t}_1$, $\mathrm{t}_2$ respectively, a zero-capacitance resistance – the output voltage $(v_o)$ is equal to the voltage capacitor $(v_c)$, it is possible to deduce the small signal model equations.

As shown in the table 9, during one period, there are four possible states that the circuit can assume. There are three energy storage elements in the circuit (two inductors and one capacitor), then three equations are necessary to describe the circuit: one for each current inductor and one for the voltage capacitor.

The system of equations is described by means of the Kirchhoff voltage law (KVL) and Kirchhoff current law (KCL). Then, the system of equations is written in matrix form and the derivative of inductor current and voltage capacitor are isolated in the left side, i.e., in the same form as: $px = Ax + BV_d$, where $p$ is the derivative operator, $A$ is a three by three matrix, $B$ is a three by one matrix.

- Case 1, $0 < t < t_1$, $r_c \approx 0$, $G_1$ is on:

$$\begin{cases} V_d - L.pi_{L1} - r_L.i_{L1} = 0 \\ V_d - L.pi_{L2} - r_L.i_{L2} - v_o = 0 \\ i_{L2} = Cpv_o + \dfrac{v_o}{R} \end{cases}$$

$$px_1 = A_1x_1 + B_1V_d$$

$$p\begin{pmatrix} i_{L1} \\ i_{L2} \\ v_o \end{pmatrix} = \begin{pmatrix} -\dfrac{r_L}{L} & 0 & 0 \\ 0 & -\dfrac{r_L}{L} & -\dfrac{1}{L} \\ 0 & \dfrac{1}{C} & -\dfrac{1}{RC} \end{pmatrix}\begin{pmatrix} i_{L1} \\ i_{L2} \\ v_o \end{pmatrix} + \begin{pmatrix} \dfrac{1}{L} \\ \dfrac{1}{L} \\ 0 \end{pmatrix} V_d \quad (18)$$

- Case 2, $t_1 < t < \frac{T_s}{2}$, $r_c \approx 0$:

$$\begin{cases} V_d - L.pi_{L1} - r_L.i_{L1} - v_o = 0 \\ V_d - L.pi_{L2} - r_L.i_{L2} - v_o = 0 \\ i_{L1} + i_{L2} = Cpv_o + \dfrac{v_o}{R} \end{cases}$$

$$px_2 = A_2x_2 + B_2V_d$$

$$p\begin{pmatrix} i_{L1} \\ i_{L2} \\ v_o \end{pmatrix} = \begin{pmatrix} -\dfrac{r_L}{L} & 0 & -\dfrac{1}{L} \\ 0 & -\dfrac{r_L}{L} & -\dfrac{1}{L} \\ \dfrac{1}{C} & \dfrac{1}{C} & -\dfrac{1}{RC} \end{pmatrix}\begin{pmatrix} i_{L1} \\ i_{L2} \\ v_o \end{pmatrix} + \begin{pmatrix} \dfrac{1}{L} \\ \dfrac{1}{L} \\ 0 \end{pmatrix} V_d \quad (19)$$

- Case 3, $\frac{T_s}{2} < t < t_2$, $r_c \approx 0$, $G_3$ is on

$$\begin{cases} V_d - L.pi_{L1} - r_L.i_{L1} - v_o = 0 \\ V_d - L.pi_{L2} - r_L.i_{L2} = 0 \\ i_{L1} = Cpv_o + \dfrac{v_o}{R} \end{cases}$$

$$px_3 = A_3x_3 + B_3V_d$$

$$p\begin{pmatrix} i_{L1} \\ i_{L2} \\ v_o \end{pmatrix} = \begin{pmatrix} -\dfrac{r_L}{L} & 0 & -\dfrac{1}{L} \\ 0 & -\dfrac{r_L}{L} & 0 \\ \dfrac{1}{C} & 0 & -\dfrac{1}{RC} \end{pmatrix}\begin{pmatrix} i_{L1} \\ i_{L2} \\ v_o \end{pmatrix} + \begin{pmatrix} \dfrac{1}{L} \\ \dfrac{1}{L} \\ 0 \end{pmatrix} V_d \quad (20)$$

- Case 4, $t_2 < \mathrm{t} < \mathrm{T}_s$, $r_c \approx 0$:

$$\begin{cases} V_d - L.pi_{L1} - r_L.i_{L1} - v_o = 0 \\ V_d - L.pi_{L2} - r_L.i_{L2} - v_o = 0 \\ i_{L1} + i_{L2} = Cpv_o + \dfrac{v_o}{R} \end{cases}$$

$$px_4 = A_4x_4 + B_4V_d$$

$$p\begin{pmatrix} i_{L1} \\ i_{L2} \\ v_o \end{pmatrix} = \begin{pmatrix} -\dfrac{r_L}{L} & 0 & -\dfrac{1}{L} \\ 0 & -\dfrac{r_L}{L} & -\dfrac{1}{L} \\ \dfrac{1}{C} & \dfrac{1}{C} & -\dfrac{1}{RC} \end{pmatrix}\begin{pmatrix} i_{L1} \\ i_{L2} \\ v_o \end{pmatrix} + \begin{pmatrix} \dfrac{1}{L} \\ \dfrac{1}{L} \\ 0 \end{pmatrix} V_d \tag{21}$$

Then, the average value of state variables derivative ($\mathrm{p} < \mathrm{x} >$) must be determined. An index will be written in order to identify which case the matrices are from: for example, matrices $A$ and $B$ of the first case will receive an index 1.

$$\mathrm{p} < \mathrm{x} > = \frac{1}{\mathrm{T}_s}\int_0^{\mathrm{T}_s} px.dt \tag{22}$$

Simplifying the notation, i.e., the $x = < x >$, and substituting the values of $px$:

$$\mathrm{px} = \frac{1}{\mathrm{T}_s}\left(\int_0^{t_1} px_1.dt + \int_{t_1}^{\frac{\mathrm{T}_s}{2}} px_2.dt + \int_{\frac{\mathrm{T}_s}{2}}^{t_2} px_3.dt + \int_{t_2}^{\mathrm{T}_s} px_4.dt\right)$$

$$\mathrm{px} = \frac{1}{\mathrm{T}_s}\left(\int_0^{d\mathrm{T}_s} (A_1x + B_1vd).dt + \int_{d\mathrm{T}_s}^{\frac{\mathrm{T}_s}{2}} (A_2x + B_2v_d).dt + \int_{\frac{\mathrm{T}_s}{2}}^{\mathrm{T}_s(\frac{1}{2}+d)} (A_3x + B_3v_d).dt + \int_{\mathrm{T}_s(\frac{1}{2}+d)}^{\mathrm{T}_s} (A_4x + B_4v_d).dt\right)$$

$$\mathrm{px} = \frac{1}{\mathrm{T}_s}\left((A_1x + B_1v_d).d\mathrm{T}_s + (A_2x + B_2v_d).\left(\frac{1}{2} - d\right)\mathrm{T}_s + (A_3x + B_3v_d).d\mathrm{T}_s + (A_4x + B_4v_d).\left(\frac{1}{2} - d\right)\mathrm{T}_s\right)$$

$$\text{px} = \left(\left((A_1 + A_3)d + \frac{1}{2}(A_2 + A_4)(1 - 2d)\right)x + \left((B_1 + B_3)d + \frac{1}{2}(B_2 + B_4)(1 - 2d)\right)v_d\right) \tag{23}$$

By equation analysis, it is possible to notice that the value “2” in the last equation is due to the number of phases in the circuit, then it can be substituted by “n”.

$$\text{px} = \left(\left((A_1 + A_3)d + \frac{1}{n}(A_2 + A_4)(1 - nd)\right)x + \left((B_1 + B_3)d + \frac{1}{n}(B_2 + B_4)(1 - nd)\right)v_d\right) \tag{24}$$

Introduce the separation of AC perturbation and DC component in the variables $x$, $d$. The letter tilde on top represents the AC perturbation and the capital letter the DC component. For the variable input voltage is considered pure DC.

$$\begin{aligned} x &= \tilde{x} + X \\ d &= \tilde{d} + D \end{aligned} \tag{25}$$

Substituting (25) into (24), after algebraic manipulations and neglecting higher harmonics (e.g.: $\tilde{x}.\tilde{d} \approx 0$):

$$\begin{aligned} p\tilde{x} = &\left[\left((A_1 + A_3)D + \tfrac{1}{n}(A_2 + A_4)(1 - nD)\right)X + \left((B_1 + B_3)D + \tfrac{1}{n}(B_2 + B_4)(1 - nD)\right)Vd\right] \\ &+ \left[\left((A_1 + A_3)D + \tfrac{1}{n}(A_2 + A_4)(1 - nD)\right)\tilde{x} + \left((A_1 + A_3 - A_2 - A_4)X + (B_1 + B_3 - B_2 - B_4)V_d\right)\tilde{d}\right] \end{aligned} \tag{26}$$

The first bracket in (26) is the steady state response of the circuit, which, by definition, is zero value. The matrices $B_1$, $B_2$, $B_3$ and $B_4$ are equal. Matrices $A_2$ and $A_4$ are also equal, so the sum of then is two times the value of $A_2$, however, in this case it is also possible to substitute the value “2” by “n”. Rewriting the equation (26):

$$\begin{cases} p\tilde{x} = A\tilde{x} + (A_1 + A_3 - nA_2)X\tilde{d} \\ A = (A_1 + A_3)D + A_2(1 - nD) \end{cases} \tag{27}$$

Finally, performing the Laplace transform and isolating the AC perturbations in the left side it is possible to find the transfer function of the state variables. The matrix "I" is the unit matrix and "s" is the Laplace variable.

$$\begin{cases} \dfrac{\tilde{x}(s)}{\tilde{d}(s)} = (sI - A)^{-1}(A_1 + A_3 - nA_2)X \\ A = (A_1 + A_3)D + A_2(1 - nD) \end{cases} \tag{28}$$

Substituting the values, it is possible to find the matrices values.

$$A = \begin{pmatrix} -\dfrac{r_L}{L} & 0 & -\dfrac{1}{L}(1-D) \\ 0 & -\dfrac{r_L}{L} & -\dfrac{1}{L}(1-D) \\ \dfrac{1}{C}(1-D) & \dfrac{1}{C}(1-D) & -\dfrac{1}{RC} \end{pmatrix}$$

$$A_1 + A_3 - nA_2 = \begin{pmatrix} 0 & 0 & \dfrac{1}{L} \\ 0 & 0 & \dfrac{1}{L} \\ -\dfrac{1}{C} & -\dfrac{1}{C} & 0 \end{pmatrix}$$

To find the values of matrix $X = (x_1 \quad x_2 \quad x_3)^t$, which are the steady state variables ($x_1 = I_{L1}$, $x_2 = I_{L2}$, $x_3 = V_o$), similar equations to the proposed converter are used. As both topologies – IBC and MDIBC – present two-phases, the procedure to calculate the current inductor steady state value is the same (equation 12). is calculated considering that the output power $(P_o)$ is equal to the input power $(P_i)$ and the current inductor in both phases are the same. The steady state output voltage is calculated according to the equation 29, non-ideal characteristics are neglected.

$$V_o = \frac{V_d}{1 - D} \tag{29}$$

Performing some algebraic calculations, it is found the small signal perturbation in the current inductor and the voltage capacitor.

- Current inductor state equation:

$$G_{id}(s) = \frac{\tilde{\imath}_L(s)}{\tilde{d}(s)} = G_{di}\frac{\left(1+\frac{s}{\omega_{zi}}\right)}{\Delta(s)} \tag{30}$$

$$\begin{cases} G_{di} = \dfrac{x_3 + (x_1+x_2)(1-D)R}{r_L + 2R(1-D)^2} \\ \omega_{zi} = \dfrac{x_3 + (x_1+x_2)(1-D)R}{RCx_3} \\ \Delta(s) = \dfrac{s^2}{\omega_0^2} + \dfrac{s}{Q\omega_0} + 1 \\ \omega_0 = \sqrt{\dfrac{r_L + 2R(1-D)^2}{RLC}}, Q = \dfrac{\sqrt{RLC(r_L + 2R(1-D)^2)}}{RCr_L + L} \end{cases}$$

- Output voltage state equation:

$$G_{vd}(s) = \frac{\tilde{v}_o(s)}{\tilde{d}(s)} = G_{dv}\frac{\left(1-\frac{s}{\omega_{zv}}\right)}{\Delta(s)} \tag{31}$$

$$\begin{cases} G_{dv} = \dfrac{R(2(1-D)x_3 - (x_1+x_2)r_L)}{r_L + 2R(1-D)^2} \\ \omega_{zv} = \dfrac{2R(1-D)x_3 - Rr_L(x_1+x_2)}{RL(x_1+x_2)} \end{cases}$$

Considering the input voltage ($V_d$) is 200V, the output power ($P_o$) is 30 KW, the duty cycle (D) is 0.25 and the equations 12 and 29, steady state values of $I_L$ and $V_o$ are calculated and described in the table 10.

**Table 10 –** Steady state value of $I_L$ and $V_o$ for IBC

| **Parameter** | **Value** |
|---|---|
| $I_L$ (A) | 75 |
| $V_o$ (V) | 267 |

The component values ($r_L$, $L$, $C$ and $R$) are substituted according to the table 6, then numerical transfer functions are found. The position of the zeros in (30) and (31) is given by $\omega_{zi}$ and $\omega_{zv}$. The poles position, which are the roots of the function $\Delta(s)$.

These parameters are described in the table 11. Moreover, figures 23 and 24 illustrate the position of zero and poles in the complex plan for $\frac{\tilde{\imath}_L(s)}{\tilde{d}(s)}$ and $\frac{\tilde{v}_o(s)}{\tilde{d}(s)}$ transfer functions.

**Table 11 –** Position of the zero and poles of the state equations in the IBC

| Parameter | Value |
|---|---|
| $Z_i$ | $-1903\,rad/s$ |
| $Z_v$ | $-7029\,rad/s$ |
| $P_1,\ P_2$ | $-338 \pm 3053j\,rad/s$ |
| $\lvert P_1 \rvert = \lvert P_2 \rvert$ | $3071\,rad/s$ |
| $\zeta$ | $0.1101$ |

**Note:** The subscript description: $Z$ – zero, $P$ – pole, $i$ – inductor current, $v$ – output voltage, $\zeta$ - damping ratio

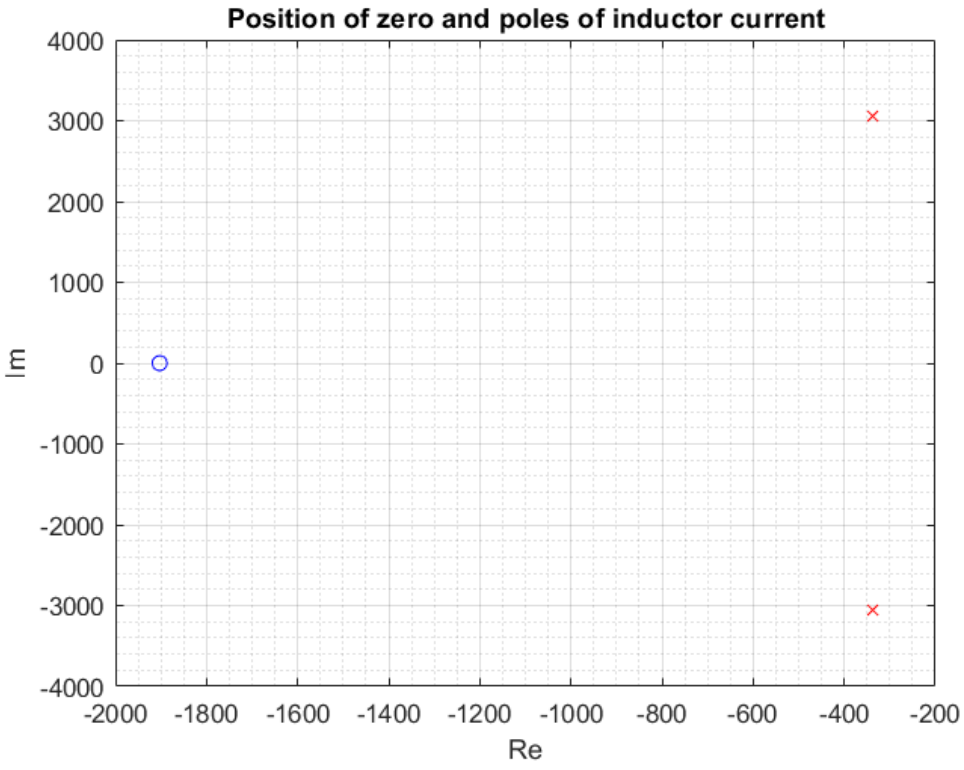


**Figure 23 –** Position of poles and zeros of the transfer function $\frac{\tilde{\imath}_L(s)}{\tilde{d}(s)}$

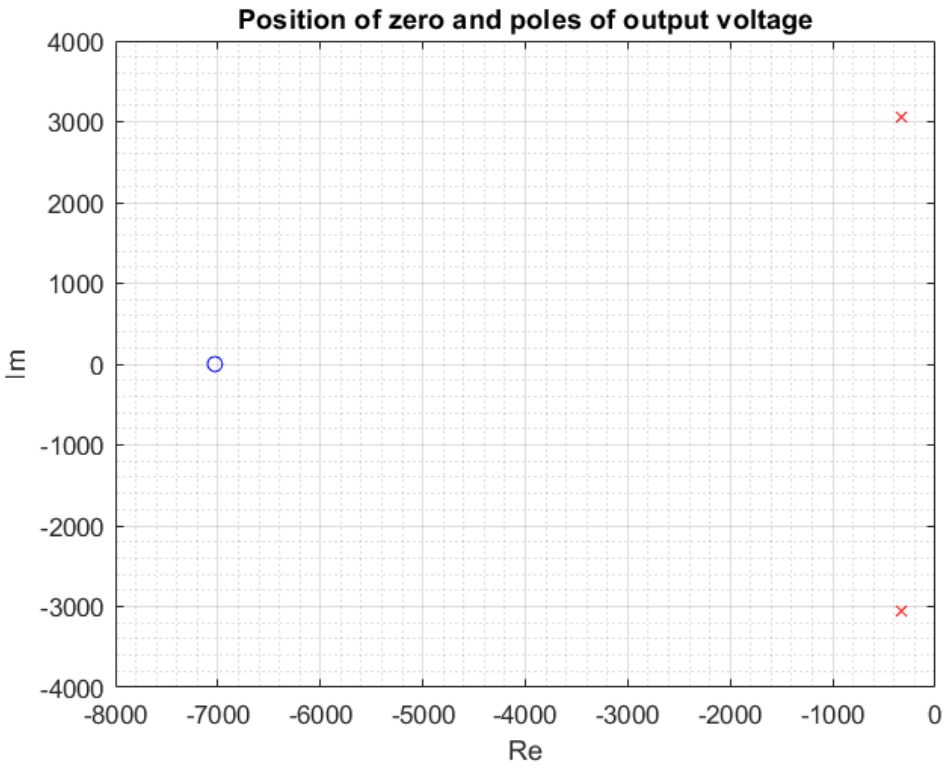


**Figure 24 –** Position of poles and zeros of the transfer function $\frac{\tilde{v}_o(s)}{\tilde{d}(s)}$

The transfer function response of $\frac{\tilde{\imath}_L(s)}{\tilde{d}(s)}$ (blue curve) and $\frac{\tilde{v}_o(s)}{\tilde{d}(s)}$ (orange curve) is illustrated with their respective Bode diagrams in figure 25.

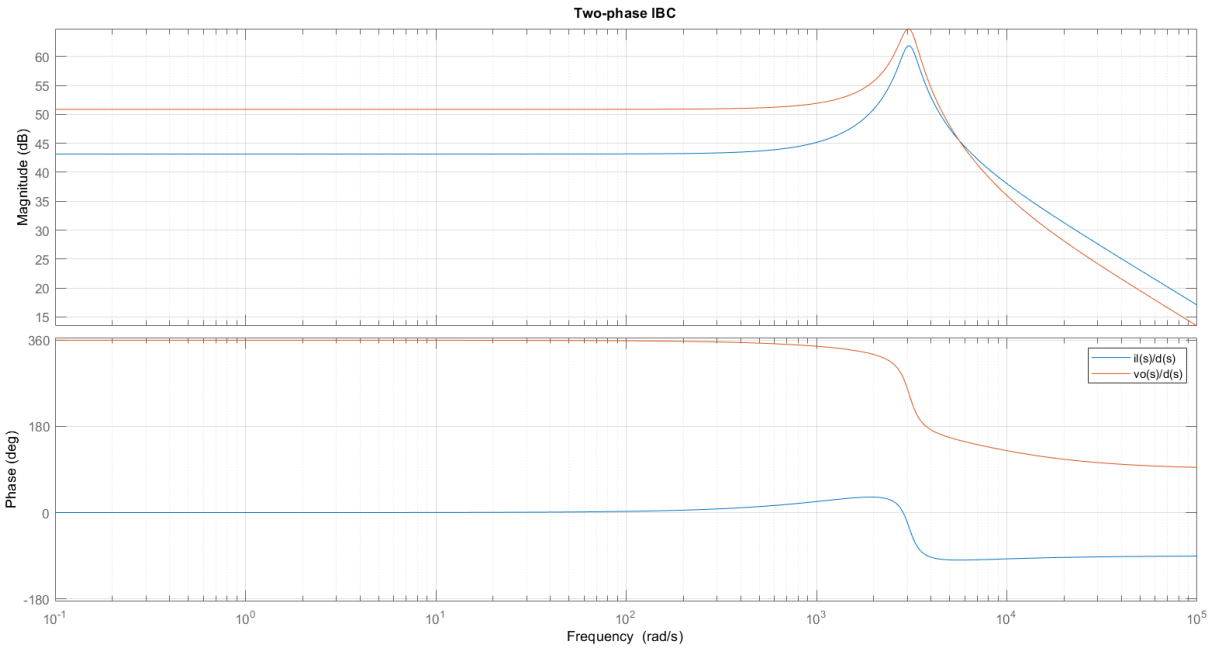


**Figure 25 –** IBC Bode diagram of the inductor current and output voltage

Figures 26 and 27 show the Bode diagrams of normalized transfer functions: $\frac{Gid(s)}{|Gdi|}$ and $\frac{Gvd(s)}{|Gdv|}$.

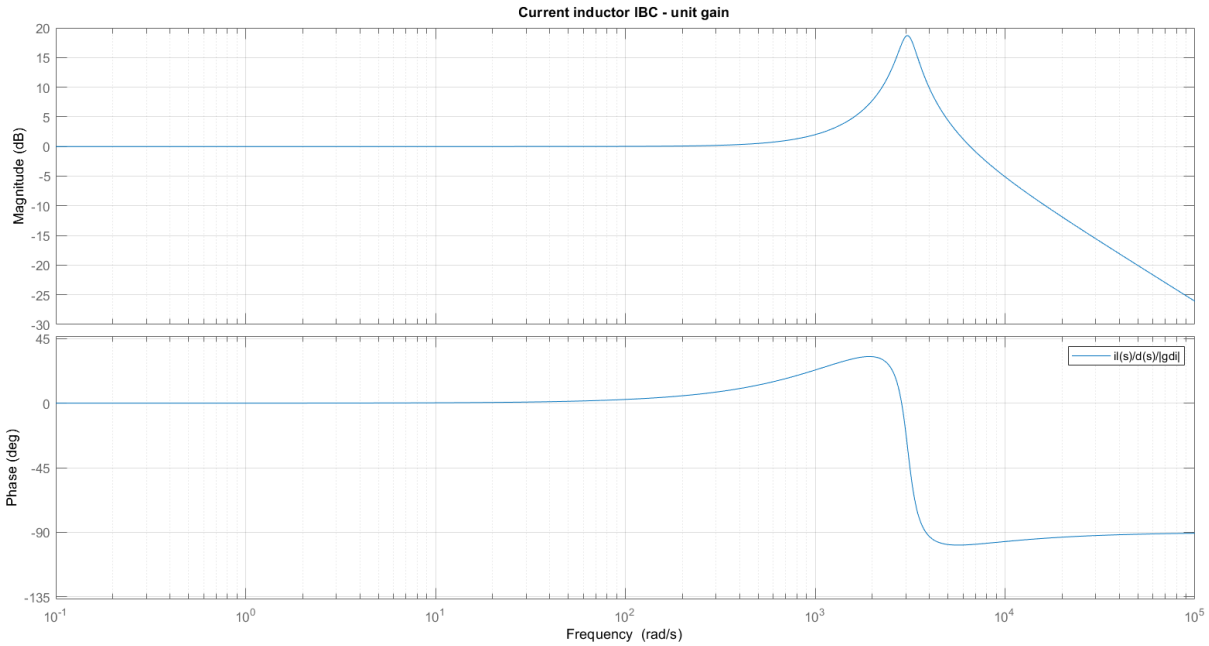


**Figure 26 –** IBC Bode diagram of inductor current normalized – unit gain

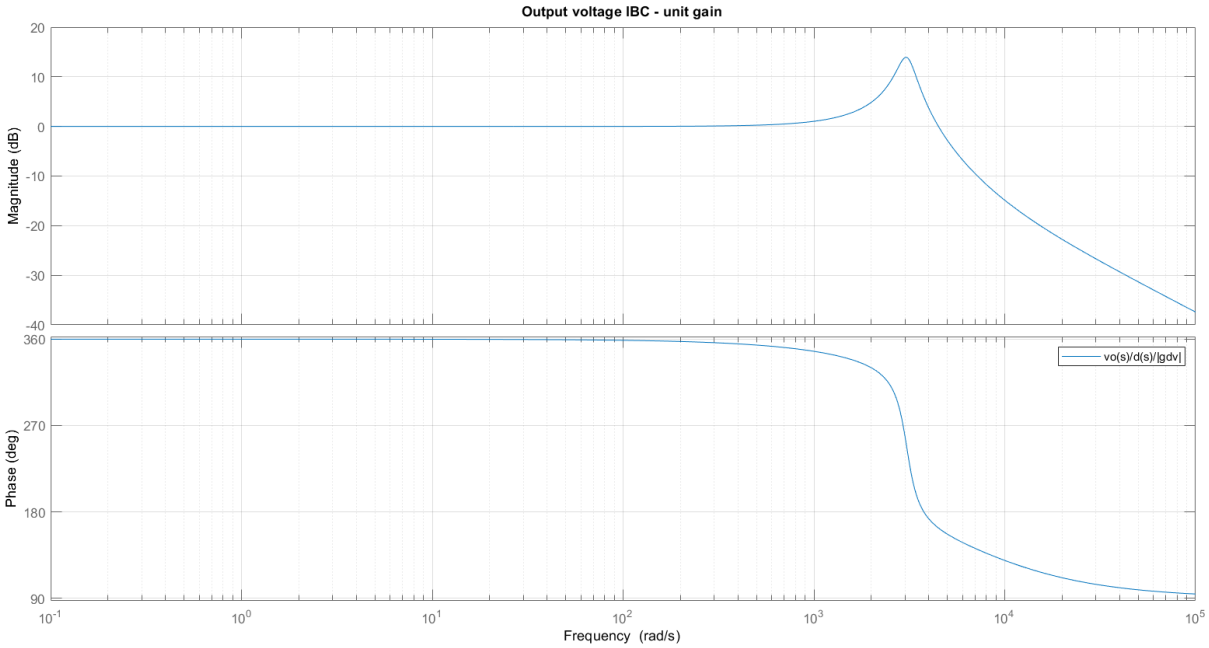


**Figure 27 –** IBC Bode diagram of output voltage normalized – unit gain

## 4.2 Multidevice boost converter (MDBC)

In this converter topology, there are one phase and two parallel legs of diode in series with an IGBT per phase. In the output, parallel to the load, there is an ideal capacitor in series with the capacitance resistance. The electric circuit of the multidevice boost converter (MDBC) is shown in the figure 28.

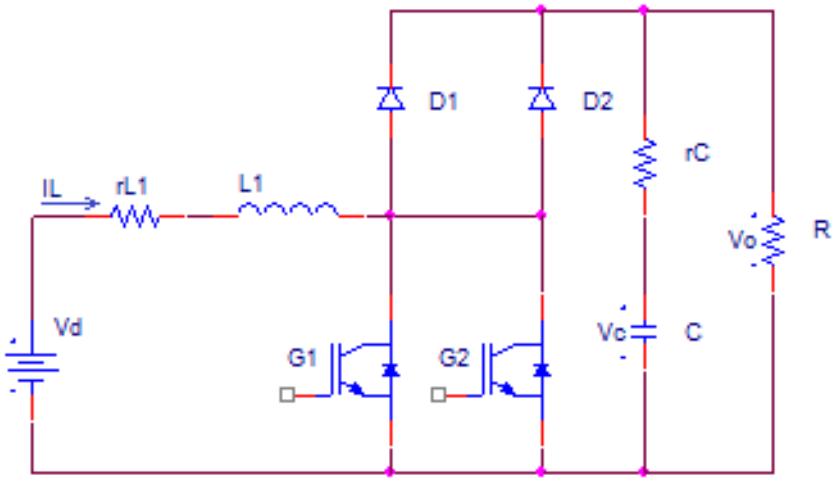


**Figure 28 –** Electric circuit of the Multidevice boost converter (MDBC)

### 4.2.1 Switching power converter

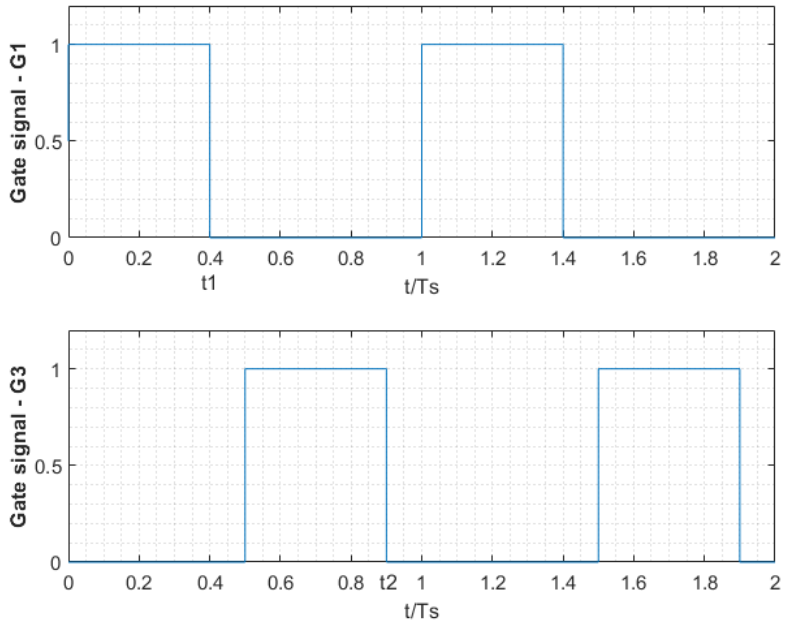


**Figure 29 –** MDBC Gate sequence for the controllable switches when the duty cycle $(d)$ is 0.40

**Table 12 –** Description of the MDBC conduction of the IGBTs and diodes and load situation when the duty cycle $(d)$ is 0.40 during one period

| Time instant | IGBT | Diode | Load situation |
|---|---|---|---|
| $0 < {}^{t}/_{Ts} < 0.40$ | $G_1$ is conducting | None | Not Powered |
| $0.40 < {}^{t}/_{Ts} < 0.50$ | None | $D_1$, $D_2$ are conducting | Powered |
| $0.50 < {}^{t}/_{Ts} < 0.90$ | $G_2$ is conducting | None | Not Powered |
| $0.90 < {}^{t}/_{Ts} < 1$ | None | $D_1$, $D_2$ are conducting | Powered |

### 4.2.2 Small signal model

Considering the electric circuit and the gate signal pattern (figures 28 and 29), and the following assumptions the small signal model is deduced. The time $t_1$ and $t_2$ are, respectively, the time instants that drive gate signals $G_1$ and $G_2$ become zero. The capacitance resistance is zero: this means that the output voltage ($v_o$) is equal to the voltage capacitor.

According to the table 12, during one period, there are four possible states that the circuit can assume. However, as the switches are in the same phase and the duty cycles of both switches are assumed identical, there are only two possible states that the MDBC can assume. The states started after the time interval $\frac{T_s}{m}$ are a repetition of the previous states.

In this case, there are two energy storage elements in the circuit (an inductor and a capacitor), hence two equations are necessary to describe the circuit: one for the current inductor and another for the voltage capacitor.

The system of equations, obtained by means of the Kirchhoff voltage law (KVL) and Kirchhoff current law (KCL), and the system of equations in matrix form are shown in the following. In matrix form, the system of equations is written according to $px = Ax + BV_d$, where $p$ is the derivative operator, $A$ is a two by two matrix, $B$ is a two by one matrix.

- Case 1, $0 < t < t_1$, $r_c \approx 0$, $G_1$ is on:

$$\begin{cases} V_d - r_L i_L - L.pi_L = 0 \\ -RCpv_o - v_o = 0 \end{cases}$$

$$px_1 = A_1 x_1 + B_1 V_d$$

$$p\begin{pmatrix} i_L \\ v_o \end{pmatrix} = \begin{pmatrix} -\frac{r_L}{L} & 0 \\ 0 & -\frac{1}{RC} \end{pmatrix}\begin{pmatrix} i_L \\ v_o \end{pmatrix} + \begin{pmatrix} \frac{1}{L} \\ 0 \end{pmatrix} V_d \tag{32}$$

- Case 2, $t_1 < t < \frac{T_s}{m}$, $r_c \approx 0$:

$$\begin{cases} V_d - r_L i_L - L.pi_L - v_o = 0 \\ i_L = Cpv_o - \frac{v_o}{R} \end{cases}$$

$$px_2 = A_2 x_2 + B_2 V_d$$

$$p\begin{pmatrix} i_L \\ v_o \end{pmatrix} = \begin{pmatrix} -\frac{r_L}{L} & -\frac{1}{L} \\ \frac{1}{C} & -\frac{1}{RC} \end{pmatrix}\begin{pmatrix} i_L \\ v_o \end{pmatrix} + \begin{pmatrix} \frac{1}{L} \\ 0 \end{pmatrix} V_d \tag{33}$$

Next, the state-space averaging procedure is derived. The matrices with index 1 and 2 are related to the first case and the second case respectively. As there are a repetition after $\frac{T_s}{m}$, the integration interval is $0 < t < \frac{T_s}{m}$.

$$p < x >= \frac{1}{\frac{T_s}{m}} \int_0^{\frac{T_s}{m}} px.dt \tag{34}$$

Simplifying the notation, i.e., the $x = < x >$, and substituting the values of $px$:

$$px = \frac{1}{T_s/m}\left( \int_0^{t1} px_1.dt + \int_{t1}^{\frac{T_s}{m}} px_2.dt \right)$$

$$px = \frac{m}{T_s}\left( \int_0^{dT_s} (A_1 x + B_1 v_d).dt + \int_{dT_s}^{\frac{T_s}{m}} (A_2 x + B_2 v_d).dt \right)$$

$$px = \frac{m}{T_s}\left( (A_1 x + B_1 v_d).dT_s + (A_2 x + B_2 v_d).\left(\frac{1}{m} - d\right)T_s \right)$$

$$\text{px} = \big(A_1 mD + A_2(1 - mD)\big)X + \big(B_1 mD + B_2(1 - mD)\big)V_d \tag{35}$$

Introduce the separation of AC perturbation and DC component in the variables $x$, $d$. The letter tilde on top represents the AC perturbation and the capital letter the DC component. For the variable of the input voltage is considered pure DC.

$$\begin{aligned} x &= \tilde{x} + X \\ d &= \tilde{d} + D \end{aligned} \tag{36}$$

Substituting (36) into (35), after algebraic manipulations and neglecting higher harmonics (e.g.: $\tilde{x}.\tilde{d} \approx 0$):

$$p\tilde{x} = [AX + BVd] + \left[A\tilde{x} + \big((A_1 - A_2)mX + (B_1 - B_2)mV_d\big)\tilde{d}\right] \tag{37}$$

The first bracket in (37), is the steady state response of the circuit, which, by definition, is zero. The matrices $B_1$, $B_2$ are equal. Considering these prepositions, the equation 19 can be rewritten.

$$\begin{cases} p\tilde{x} = A\tilde{x} + m(A_1 - A_2)X\tilde{d} \\ A = (A_1 - A_2)mD + A_2 \end{cases} \tag{38}$$

Finally, performing the Laplace transform and isolating the AC perturbations in the left side it is possible to find the transfer function of the state variable. The matrix "$I$" is the unit matrix and "$s$" is the Laplace variable.

$$\begin{cases} \dfrac{\tilde{x}(s)}{\tilde{d}(s)} = m(sI - A)^{-1}(A_1 - A_2)X \\ A = (A_1 - A_2)mD + A_2 \end{cases} \tag{38}$$

Calculating the matrices $A$ and $(A_1 - A_2)$:

$$A = \begin{pmatrix} -\dfrac{r_L}{L} & -\dfrac{1}{L}(1 - 2D) \\ \dfrac{1}{C}(1 - 2D) & -\dfrac{1}{RC} \end{pmatrix}$$

$$A_1 - A_2 = \begin{pmatrix} 0 & \dfrac{1}{L} \\ -\dfrac{1}{C} & 0 \end{pmatrix}$$

To find the values of matrix $X = (x_1 \quad x_2)^t$, which are the steady state variables ($x_1 = I_L,\ x_2 = V_o$), similar equations to the proposed converter are used. To calculate the current inductor steady state value the input $(P_i)$ and the output power $(P_o)$ are considered equal. As both topologies – MDBC and MDIBC – present two parallel legs per phase, and neglecting non-ideal characteristics, the procedure to calculate output voltage is the same, i.e., equation 13.

$$\begin{cases} P_i = P_o \\ P_i = V_d I_L \end{cases}$$

$$I_L = \frac{P_o}{V_d} \tag{39}$$

Substituting the matrices $A$ and $(A_1 - A_2)$ in (38) and performing some algebraic calculations, it is found the small signal perturbation for both variables.

- Current inductor state equation

$$G_{id}(s) = \frac{\tilde{\imath}_L(s)}{\tilde{d}(s)} = G_{di}\frac{\left(1 + \frac{s}{\omega_{zi}}\right)}{\Delta(s)} \tag{40}$$

$$\begin{cases} G_{di} = 2\dfrac{x_2 + x_1(1-2D)R}{r_L + R\left(1 - 4D(1-D)\right)} \\ \omega_{zi} = \dfrac{x_2 + x_1(1-2D)R}{RCx_2} \\ \Delta(s) = \dfrac{s^2}{\omega_0^2} + \dfrac{s}{Q\omega_0} + 1 \\ \omega_0 = \sqrt{\dfrac{r_L + R\left(1 - 4D(1-D)\right)}{RLC}},\ Q = \dfrac{\sqrt{RLC\left(1 - 4D(1-D)\right)}}{RCr_L + L} \end{cases}$$

- Output voltage state equation:

$$G_{vd}(s) = \frac{\tilde{v}_o(s)}{\tilde{d}(s)} = G_{dv}\frac{\left(1 - \frac{s}{\omega_{zv}}\right)}{\Delta(s)} \tag{41}$$

$$\begin{cases} G_{dv} = \dfrac{2R\big((1-2D)x_2 - x_1 r_L\big)}{r_L + R\big(1-4D(1-D)\big)} \\ \omega_{zv} = \dfrac{2R\big((1-2D)x_2 - r_L x_1\big)}{x_1 L} \end{cases}$$

Considering the input voltage $(V_d)$ is 200V, the output power $(P_o)$ is 30 KW, the duty cycle (D) is 0.25 and the equations 13 and 39, steady state values of $I_L$ and $V_o$ are calculated and described in the table 10.

**Table 13 –** Steady state value of $I_L$ and $V_o$ for MDBC

| Parameter | Value |
|---|---|
| $I_L$ (A) | 150 |
| $V_o$ (V) | 400 |

The component values ($r_L$, $L$, $C$ and $R$) are substituted according to the table 6 in (40) and (41). The position of the zeros and poles are described in table 14. Figures 30 and 31 the it is illustrated the position of zero and poles in the complex plan.

**Table 14 –** Position of the zero and poles of the state equations in the MDBC

| Parameter | Value |
|---|---|
| $Z_i$ | $-1171\ rad/s$ |
| $Z_v$ | $-3465\ rad/s$ |
| $P_1, P_2$ | $-338 \pm 1422j\ rad/s$ |
| $\lvert P_1 \rvert = \lvert P_2 \rvert$ | $1461\ rad/s$ |
| $\zeta$ | 0.2313 |

**Note:** The subscript description: $Z$ – zero, $P$ – pole, $i$ – inductor current, $v$ – output voltage, $\zeta$ - damping ratio

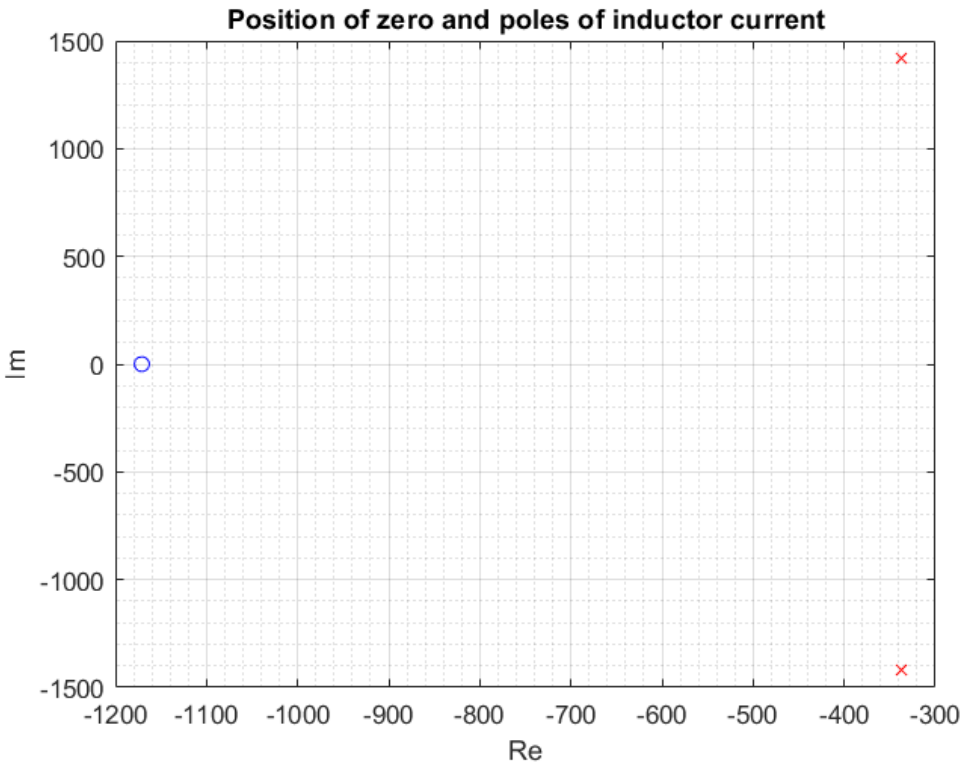


**Figure 30 –** Position of poles and zeros of the transfer function $\frac{\tilde{\imath}_L(s)}{\tilde{d}(s)}$ for the MDBC

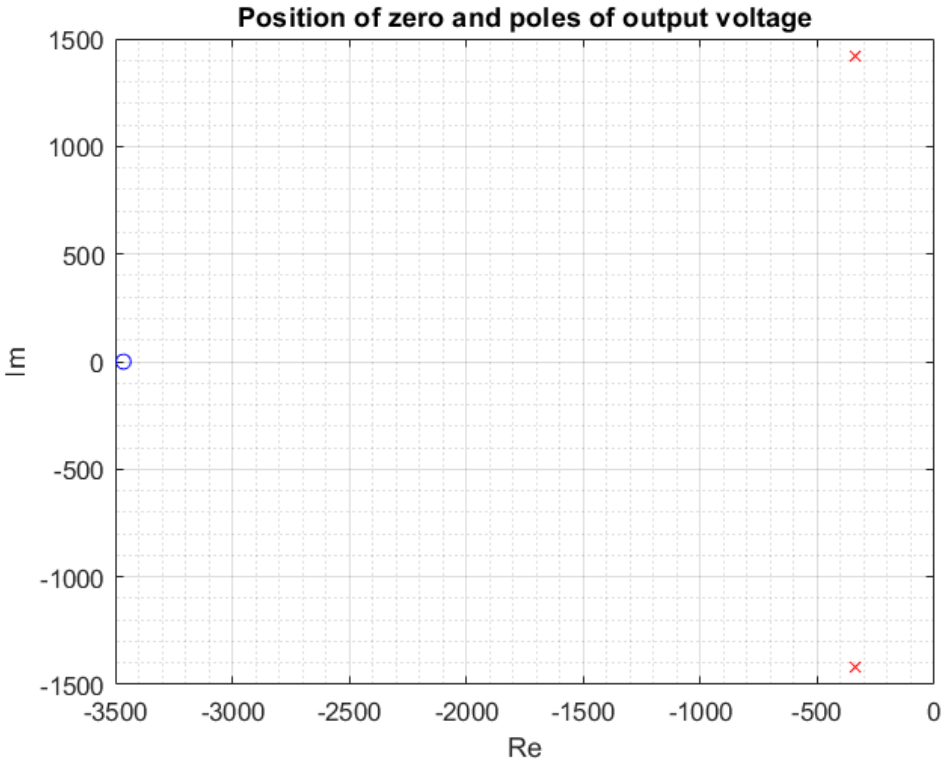


**Figure 31 –** Position of poles and zeros of the transfer function $\frac{\tilde{v}_o(s)}{\tilde{d}(s)}$ for the MDBC

Figure 32 shows the Bode diagram of the two transfer functions: the blue curve represents the $\frac{\tilde{\imath}_L(s)}{\tilde{d}(s)}$ and the orange curve the $\frac{\tilde{v}_o(s)}{\tilde{d}(s)}$ of MDBC.

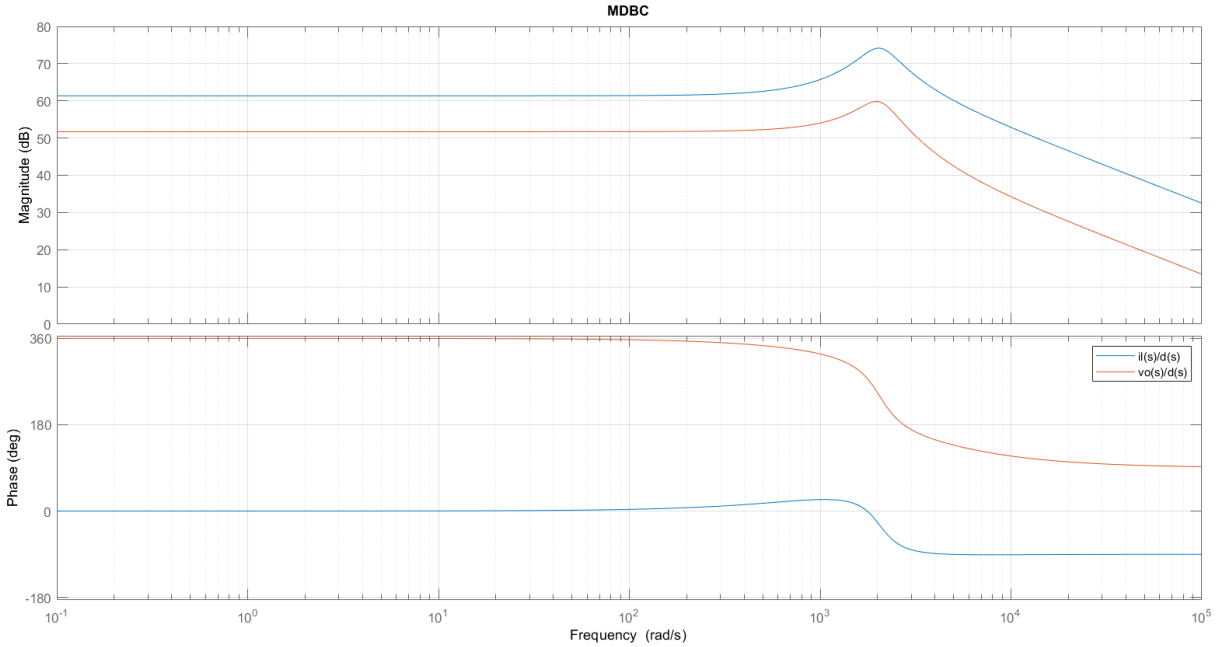


**Figure 32 –** MDBC Bode diagram of the inductor current and output voltage

In the figures 33 and 34, it is shown the normalized Bode diagrams $\frac{Gid(s)}{|Gdi|}$ and $\frac{Gvd(s)}{|Gdv|}$.

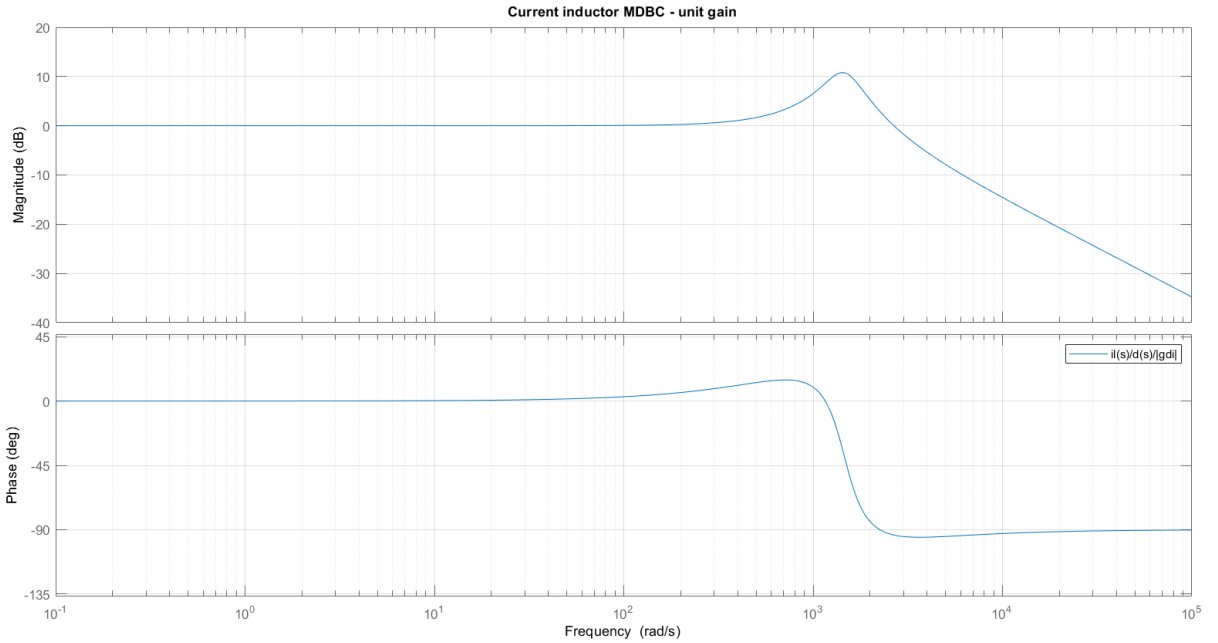

**Figure 33 –** MDBC Bode diagram of inductor current normalized – unit gain

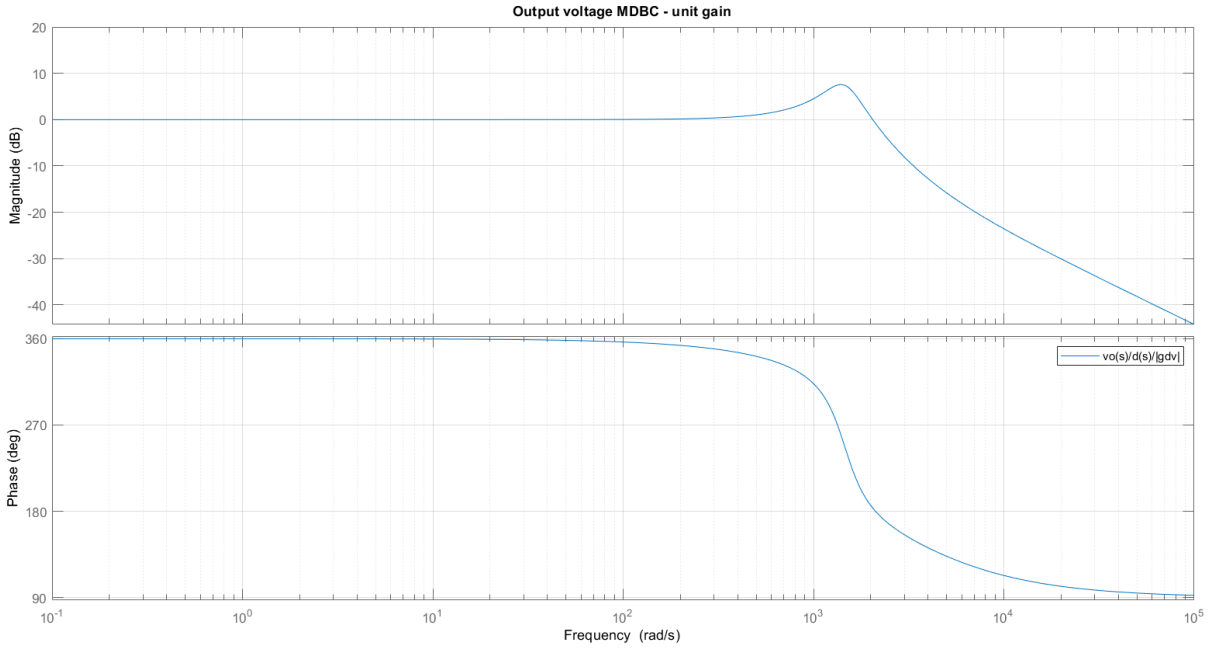


**Figure 34 –** MDBC Bode diagram of output voltage normalized – unit gain

## 5. LOSSES

The evaluation of the losses is important to estimate the overall efficiency of the converter (42). In this work, it is considered that in the proposed converter there are three sources of losses: the switching losses ($P_{sw}$), the diode losses ($P_D$) and the passive component losses ($P_c$). Their respective equations (43), (44) and (45) are taken from [8]. Moreover, to perform the loss calculation, manufacture's datasheets are need.

$$Efficiency\ (\eta) = \frac{P_{out}}{P_{out} + P_{losses}} \tag{42}$$

$$P_{sw} = \left( I_{Srms}^2 r_{CE} + V_{CE} I_{sav} + \frac{V_o}{V_{CC} I_C} \left( E_{off} \left( I_{Sav} + \frac{\Delta I}{2} \right) + E_{on} \left( I - \frac{\Delta I}{2} \right) \right) \right) \tag{43}$$

$$P_D = I_{Drms}^2 r_f + V_{F0} I_{Dav} + \frac{V_o}{V_{CC} I_C} [E_{rr}(I_{Dav})] F_s \tag{44}$$

$$P_C = I_{Lrms}^2 r_L \tag{45}$$

For the three converters studied, all the components are considered equal and then they are able to be compared. The value of the losses and their efficiency are shown in the table 15. It is important to point out that the output voltage is equal to $30\ kW$. Moreover, it is assumed that only one switch is conducting, and for the MDIBC there are two diodes conducting at the same time.

**Table 15 –** Efficiency and converter losses

| **Converter** | **Switching losses** $(P_{sw})$ | **Diode losses** $(P_D)$ | **Passive component losses** $(P_C)$ | **Efficiency** $(\eta)$ |
|---|---|---|---|---|
| MDIBC | $167.8\ W$ | $271.7\ W$ | $382.5\ W$ | 0.97 |
| IBC | $167.8\ W$ | $135.8\ W$ | $382.5\ W$ | 0.98 |
| MDBC | $371.2\ W$ | $360.8\ W$ | $765\ W$ | 0.95 |

# 6. SWITCHING POWER CONTROL

The control strategy used in this work is the dual-loop control, whose control diagram can be seen in the figure 35. The dual loop control is preferred when compared to the single loop because it improves stability and increases the system pass band. The inner loop controls the current inductor and the outer loop the output voltage.

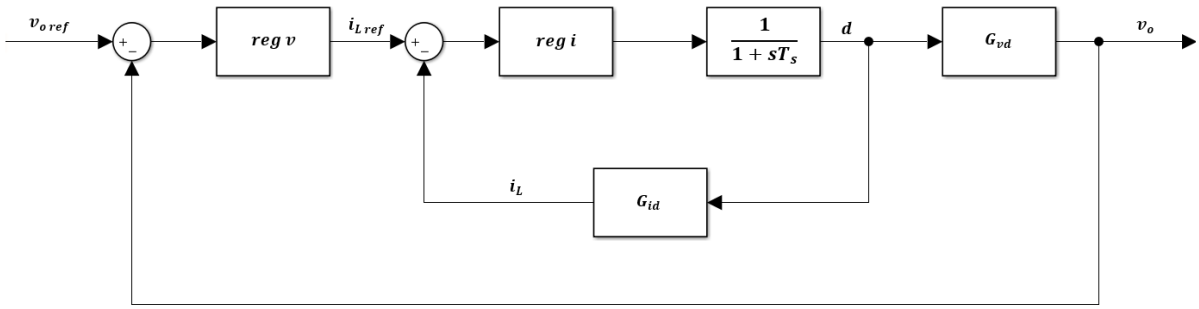


**Figure 35 –** Dual loop control strategy adopted.

The control diagram can be split in two different parts, the circuit to be controlled and the controller. The controlled circuit is represented by the block diagrams $G_{vd}$ and $G_{id}$ – output voltage and current inductor state variables – and the block diagram that considers the switching frequency. The controller is made by the regulators ($reg_v$ and $reg_i$) which are PI controllers, their characteristic equation is shown in (46).

$$reg_{v\,or\,i}(s) = k_p + \frac{k_I}{s} \tag{46}$$

The controller design is divided in two parts: firstly, the inner loop is studied – figure 36 – and the $reg_i$ parameters are calculated, then the outer loop and the $reg_v$ are also derived.

The procedure and the equations derived in this chapter, shown in the following, will be determined for a general case that uses a dual loop control strategy. Hence, it is valid for the three converters studied in this work, i.e., MDIBC, IBC and MDBC. In the end of the chapter there are the diagrams that illustrate and justify the parameters choice.

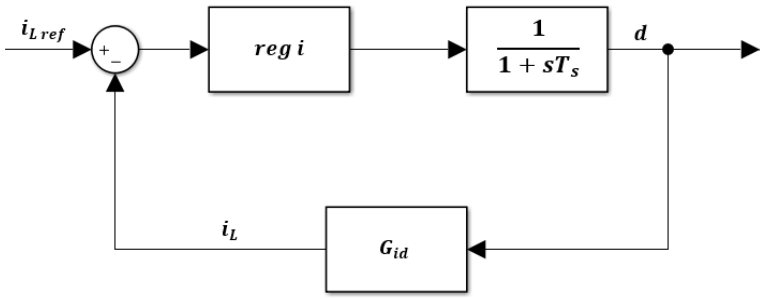


**Figure 36 –** Inner loop control – current inductor control

## 6.1 Inner loop control

The parameters of $reg_i$ is determined through the open loop current transfer function ($LI(s)$), which is the product of the three blocks. The mathematical representation is shown in the (47).

$$LI(s) = \left(k_{pI} + \frac{k_{II}}{s}\right)\left(\frac{1}{1+sT_s}\right)G_{id} \tag{47}$$

The equations that represent the circuit to be controlled are merged in one product $GI$ (48) and its Bode diagram is plotted. Then, parameters are identified such as: the position of zeros, poles and the theoretical cut-off frequency, i.e., frequency value when the transfer function response *LI*(*s*) crosses the 0dB axis.

$$GI(s) = \left(\frac{1}{1+sT_s}\right)G_{id} \tag{48}$$

The cut-off frequency, theoretically, can assume any value, however, in order to have a good response and a stable control some design practice must be considered. The cut-off frequency $(\omega_{cI})$ must be at least one decade before the switching frequency. It is interesting that $\omega_{cI}$ is not positioned in a band that the gain is $-40\ dB/dec$, due to the transfer function phase converges quickly to $-180\ deg$ which can imply in a positive feedback, hence a non-stable function. Finally, a phase-margin $(\varphi_m)$ must be at least $45\ deg$, i.e., the minimum phase distance from $-180\ deg$ at the cut-off frequency $\omega_c$, must be $45\ deg$.

Therefore, with the choice of $\omega_{cI}$ and $\varphi_{mI}$, it is possible to derive the $reg_i$ parameters. It is imposed that, at $\omega_{cI}$, the open loop transfer function magnitude will be 1 (or $0\ dB$) and the phase will be $-\pi + \varphi_{mI}$, as can be seen in the (49).

$$\begin{cases} |L(j\omega_{cI})| = 1 \\ \measuredangle L(j\omega_{cI}) = -\pi + \varphi_{mI} \end{cases} \tag{49}$$

Substituting (47) in (49) and isolating the parameters $k_{pI}$ and $k_{iI}$ in the left side, we have:

$$\begin{cases} \left|\left(k_{pI} + \dfrac{k_{II}}{j\omega_{cI}}\right)\right| |GI(j\omega_{cI})| = 1 \\ \measuredangle\left(k_{pI} + \dfrac{k_{II}}{j\omega_{cI}}\right) + \measuredangle GI(j\omega_{cI}) = -\pi + \varphi_{mI} \end{cases}$$

$$\begin{cases} \left|\left(k_{pI} - j\dfrac{k_{II}}{\omega_{cI}}\right)\right| = \dfrac{1}{|GI(j\omega_{cI})|} \\ \measuredangle\left(k_{pI} - j\dfrac{k_{II}}{\omega_{cI}}\right) = -\pi + \varphi_{mI} - \measuredangle GI(j\omega_{cI}) \end{cases} \tag{50}$$

The vector in (50) can be interpreted in two different ways, using the Cartesian from, i.e., $z = a + jb$, and in the polar form, i.e., $z = |z|\cos\varphi + j|z|\sin\varphi$. Comparing the (50) with the Cartesian form and the polar form, the values of $a$, $b$, $|z|$ and $\varphi$ are found. Finally, comparing the cartesian and the polar equations, it is possible to determine the values of $k_{pI}$ and $k_{iI}$, as shown in the equation 51.

$$\begin{cases} a = k_{pI} \\ b = -\dfrac{k_{II}}{\omega_{cI}} \\ |z| = \dfrac{1}{|GI(j\omega_{cI})|} \\ \varphi = -\pi + \varphi_m - \measuredangle GI(j\omega_{cI}) \end{cases}$$

$$\begin{cases} k_{pI} = \dfrac{1}{|GI(j\omega_{cI})|}\cos\left(-\pi + \varphi_{mI} - \measuredangle GI(j\omega_{cI})\right) \\ k_{iI} = -\dfrac{\omega_c}{|GI(j\omega_{cI})|}\sin\left(-\pi + \varphi_{mI} - \measuredangle GI(j\omega_{cI})\right) \end{cases} \tag{51}$$

As the parameters of $reg_i$ have already been calculated, it is necessary to calculate the closed loop transfer function. In the figure 37 (a), it is shown the simplification of the inner loop block diagram (figure 36). If two blocks diagram is used, it is easier to derive the closed loop current transfer function ($KI(s)$) using this strategy. The figure 37 (b) shows another block simplification, with the interpretation of the inner closed loop when the outer loop is analysed.

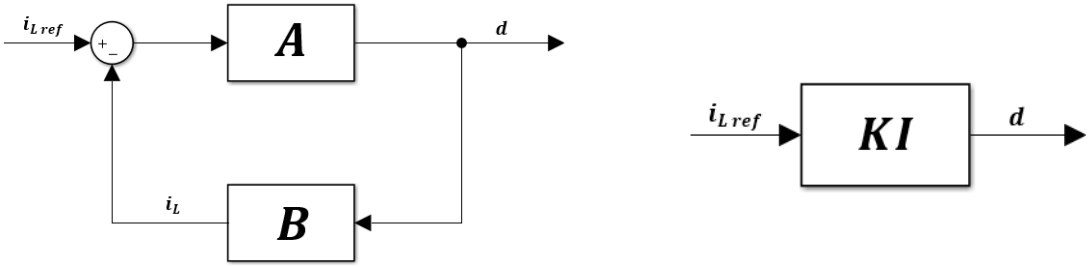


(a) (b)

**Figure 37 –** Simplification of the inner loop control

From the figure 37 (a), it is possible to find a relation between the output ($d$) and the input ($i_{L\,ref}$), as illustrated in the (52).

$$\tilde{d}(s) = A(s)(i_{L\,ref}(s) - \tilde{d}(s)B(s))$$

$$\begin{cases} \tilde{d}(s) = \dfrac{A(s)}{1 + A(s)B(s)}\, i_{L\,ref}(s) \\ KI(s) = \dfrac{A(s)}{1 + A(s)B(s)} \end{cases} \tag{52}$$

If the same notation of the figure 37 (a) is used, the open loop current transfer function ($LI(s)$) is the product of the two blocks $AB$. Hence, it is possible to relate the closed loop transfer function ($KI(s)$) and the open loop transfer function ($LI(s)$), as shown in the (53).

$$KI(s) = \frac{A(s)}{1 + A(s)B(s)}$$

$$KI(s) = \frac{\dfrac{A(s)B(s)}{B(s)}}{1 + A(s)B(s)}$$

$$KI(s) = \frac{\dfrac{LI(s)}{G_{id}(s)}}{1 + LI(s)} \tag{53}$$

## 6.2 Outer loop control

The procedure to calculate the parameters of $reg_v$ is similar to the calculation for the inner loop control. As previously, it is necessary to calculate the open loop voltage transfer function ($LV(s)$). The inner loop is represented by the KI block diagram

– figure 37 (b), the value of the $KI(s)$ is shown in the (53). The equation (54) shows the open loop voltage transfer function.

$$LV(s) = \left(k_{pV} + \frac{k_{IV}}{s}\right) KV(s) G_{vd} \tag{54}$$

The bode diagram of (55) is plotted, and the position of poles and zeros are analysed in order to choose a cut-off frequency ($\omega_{cV}$).

$$GV(s) = KI(s) G_{vd} \tag{55}$$

However, besides the design practices pointed out for the design of the inner loop control, the voltage cut-off frequency was chosen according to the (56).

$$\omega_{cV} = \frac{\omega_{cI}}{10} \tag{56}$$

If the parameters $\omega_{cV}$ and $\varphi_{mV}$ are chosen, it is possible to derive the $reg_v$ parameters using the same step-by-step from the inner loop – equations (49) to (51).

Finally, it is necessary to calculate the closed loop voltage transfer function; as it is a simple feedback loop it is easy to determine, as can be shown in the (57).

$$KV(s) = \frac{LV(s)}{1 + LV(s)} \tag{57}$$

The values of the voltage and current cut-off frequency for the three converter topologies is shown in the table 16.

**Table 16 –** Values of current and voltage cut-off frequency for each converter type.

| **Converter** | **Current cut-off frequency ($\omega_{cI}$)** | **Voltage cut-off frequency ($\omega_{cV}$)** |
|---|---|---|
| MDIBC | $6280\ rad/s$ | $628\ rad/s$ |
| IBC | $6280\ rad/s$ | $628\ rad/s$ |
| MDBC | $3140\ rad/s$ | $314\ rad/s$ |

The value of the phase-margin ($\varphi_m$), for a given $\omega_c$, changes the value of $k_p$ and $k_I$; therefore, to avoid negative values of $k_p$ and $k_I$ the graphs $k_p\ vs.\ \varphi_m$ and $k_i\ vs.\ \varphi_m$ are plotted. The tables 14, 15 and 16 show the values of the controller

proportional and integral parameters $(k_{pI}, k_{iI}\ k_{pV}, k_{iV})$ for, respectively, the MDIBC, IBC and MDBC.

**Table 17 –** Value of the controller proportional and integral parameters $(k_{pI}, k_{iI}\ k_{pV}, k_{iV})$ for the MDIBC when $\varphi_{mI} = 60\ deg$, $\varphi_{mV} = 70\ deg$

| Parameter | Value |
|---|---|
| $k_{pI}$ | 0.0027 |
| $k_{iI}$ | 2.64 |
| $k_{pV}$ | 0. 384 |
| $k_{iV}$ | 626 |

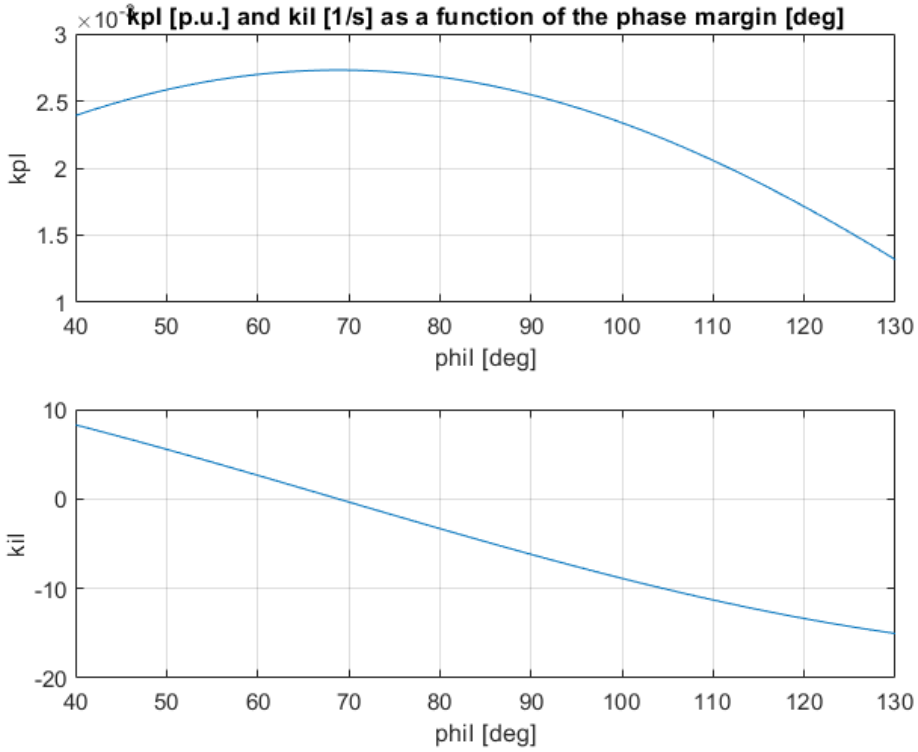


**Figure 38 –** $k_{pI}\ vs.\ \varphi_{mI}$ and $k_{iI}\ vs.\ \varphi_{mI}$ – MDIBC

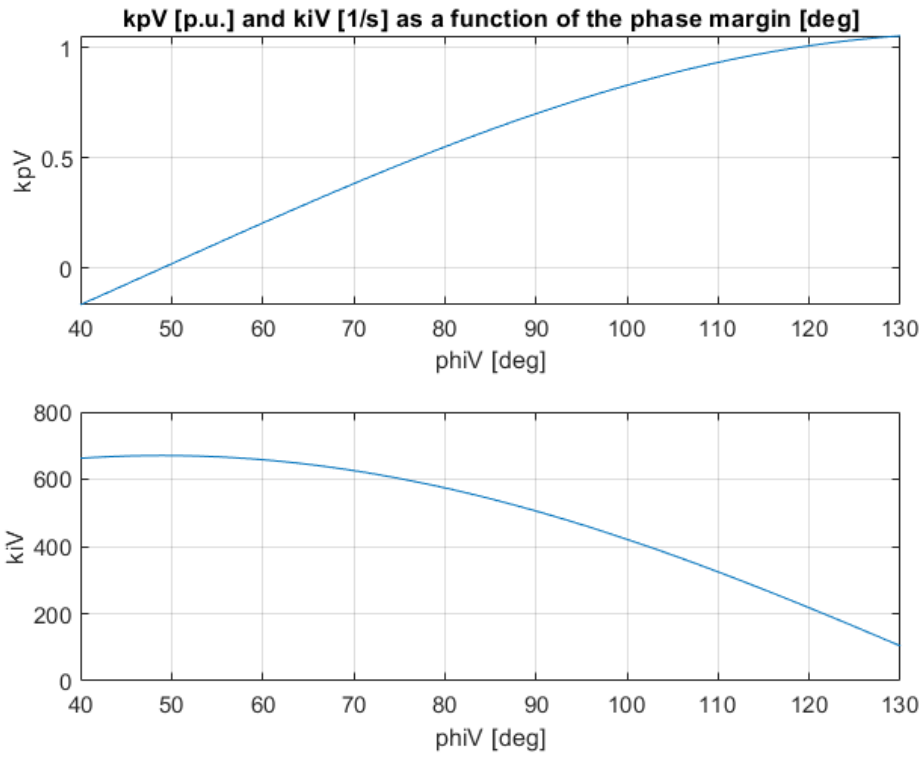


**Figure 39 –** $k_{pV}\ vs.\varphi_{mV}$ and $k_{iV}\ vs.\varphi_{mV}$ – MDIBC

**Table 18 –** Value of the controller proportional and integral parameters $(k_{pI}, k_{iI}\ k_{pV}, k_{iV})$ for the IBC when $\varphi_{mI} = 60\ deg$, $\varphi_{mV} = 60\ deg$

| Parameter | Value |
|---|---|
| $k_{pI}$ | 0.0068 |
| $k_{iI}$ | 2.81 |
| $k_{pV}$ | 0.0257 |
| $k_{iV}$ | 475 |

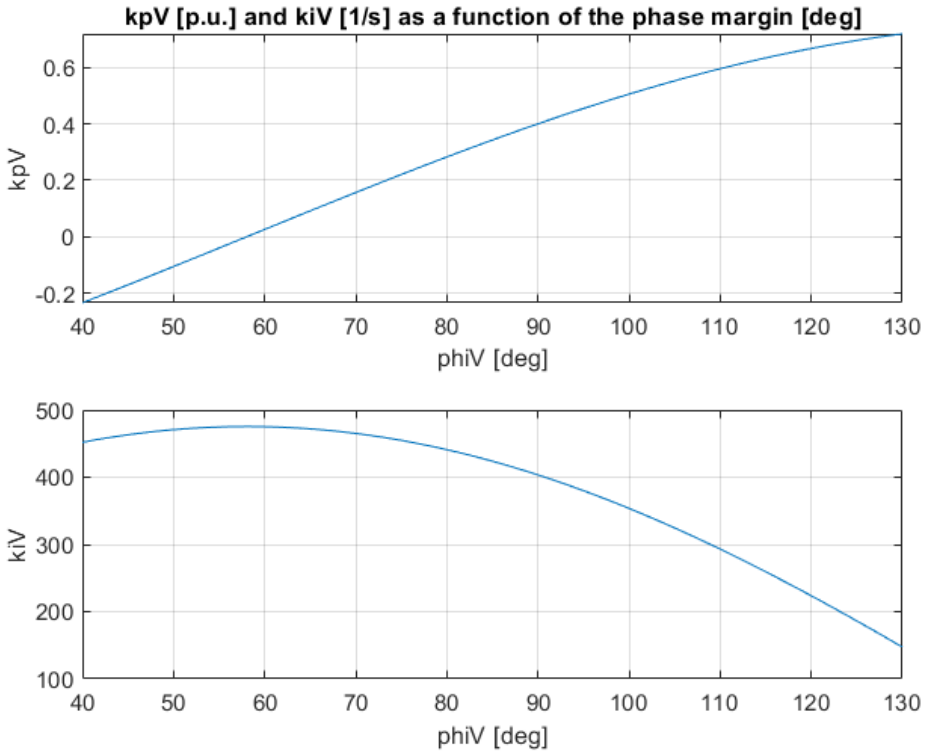


**Figure 40 –** $k_{pI}\ vs.\ \varphi_{mI}$ and $k_{iI}\ vs.\ \varphi_{mI}$ – IBC

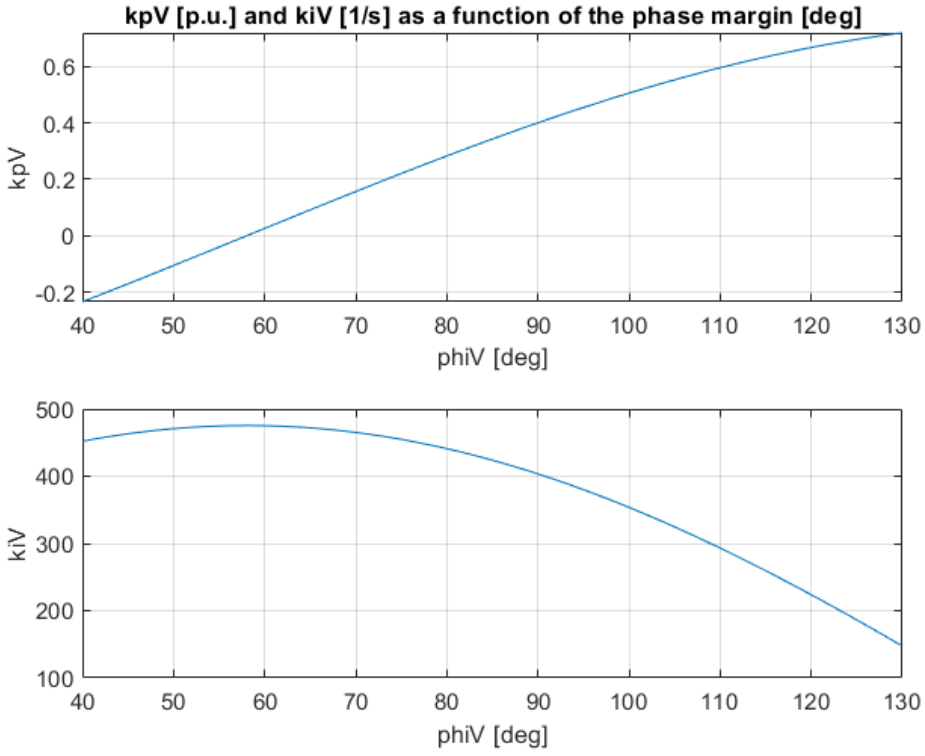


**Figure 41 –** $k_{pV}\ vs.\ \varphi_{mV}$ and $k_{iV}\ vs.\ \varphi_{mV}$ – IBC

**Table 19 –** Value of the controller proportional and integral parameters $(k_{pI}, k_{iI}\ k_{pV}, k_{iV})$ for the MDBC when $\varphi_{mI} = 70\ deg$, $\varphi_{mV} = 70\ deg$

| Parameter | Value |
|---|---|
| $k_{pI}$ | 0.0011 |
| $k_{iI}$ | 0.372 |
| $k_{pV}$ | 0.175 |
| $k_{iV}$ | 250 |

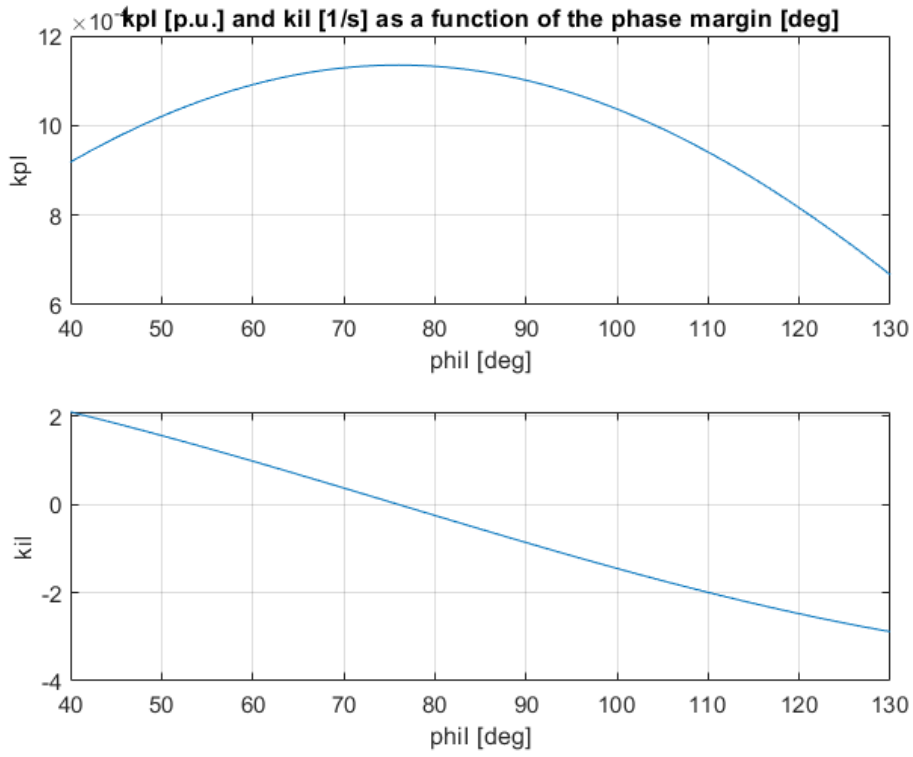


**Figure 42 –** $k_{pI}\ vs.\ \varphi_{mI}$ and $k_{iI}\ vs.\ \varphi_{mI}$ – MDBC

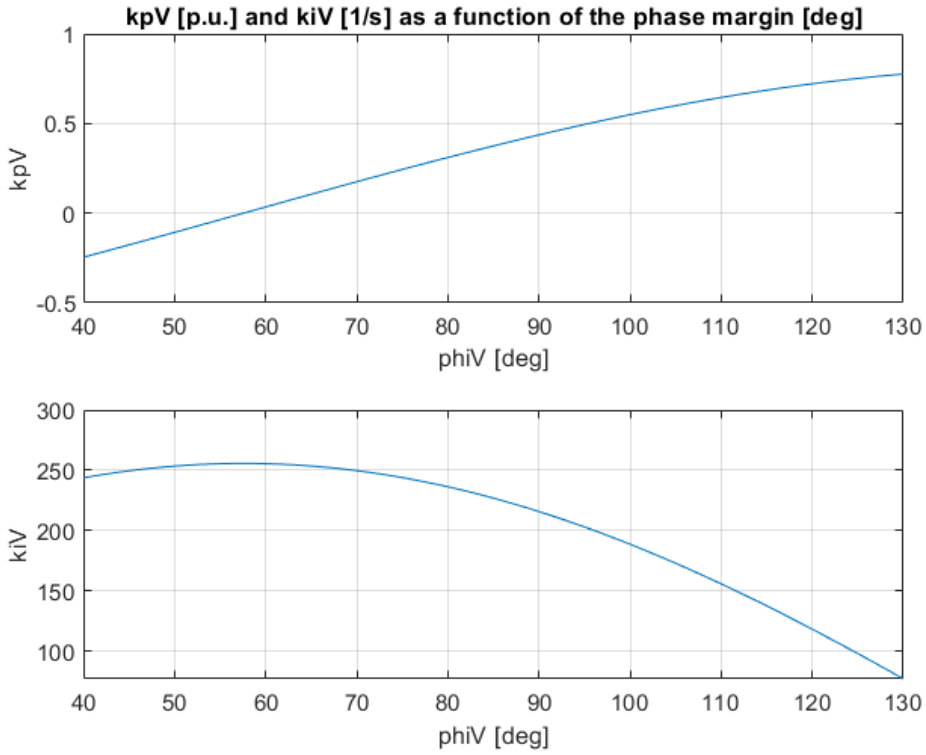


**Figure 43 –** $k_{pV}\ vs.\ \varphi_{mV}$ and $k_{iV}\ vs.\ \varphi_{mV}$ – MDBC

The Bode diagram of the transfer functions: $GI(s)$, $LI(s)$, $KI(s)$, $GV(s)$, $LV(s)$, $KV(s)$, for each converter topology, are shown in the figures 44 to 55. These figures illustrate the procedure described in this chapter to find the controller parameters ($k_p$ and $k_i$) for each controller ($reg_i$ and $reg_v$).

- MDIBC

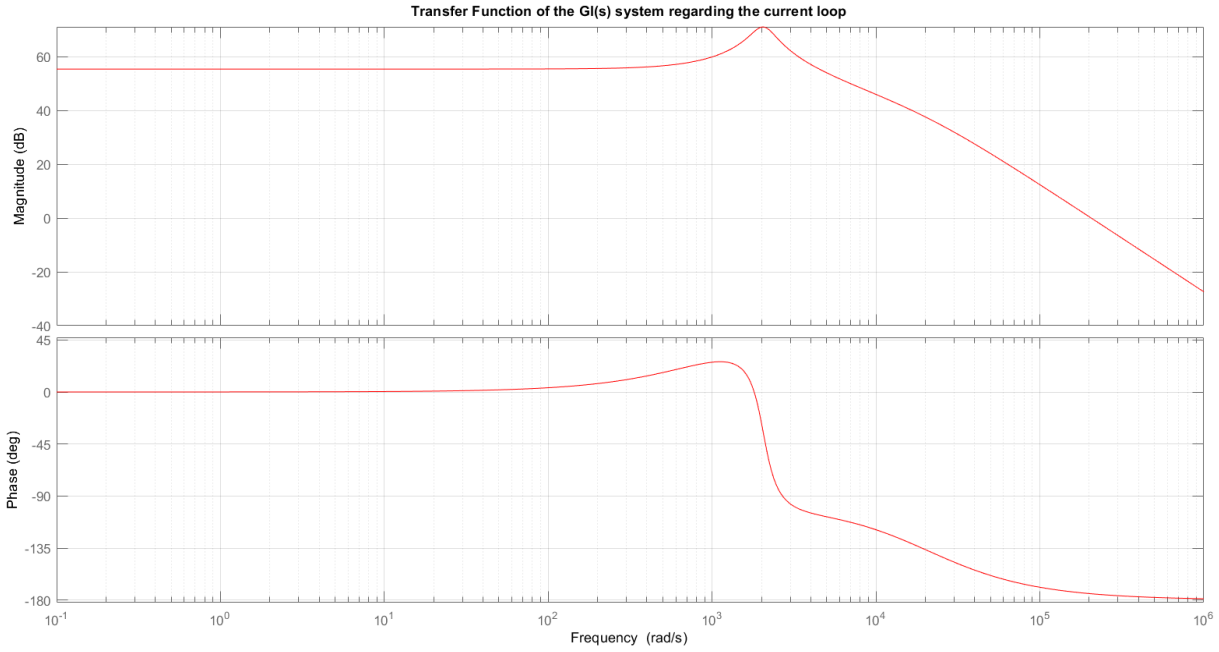


**Figure 44 –** Transfer function GI – MDIBC

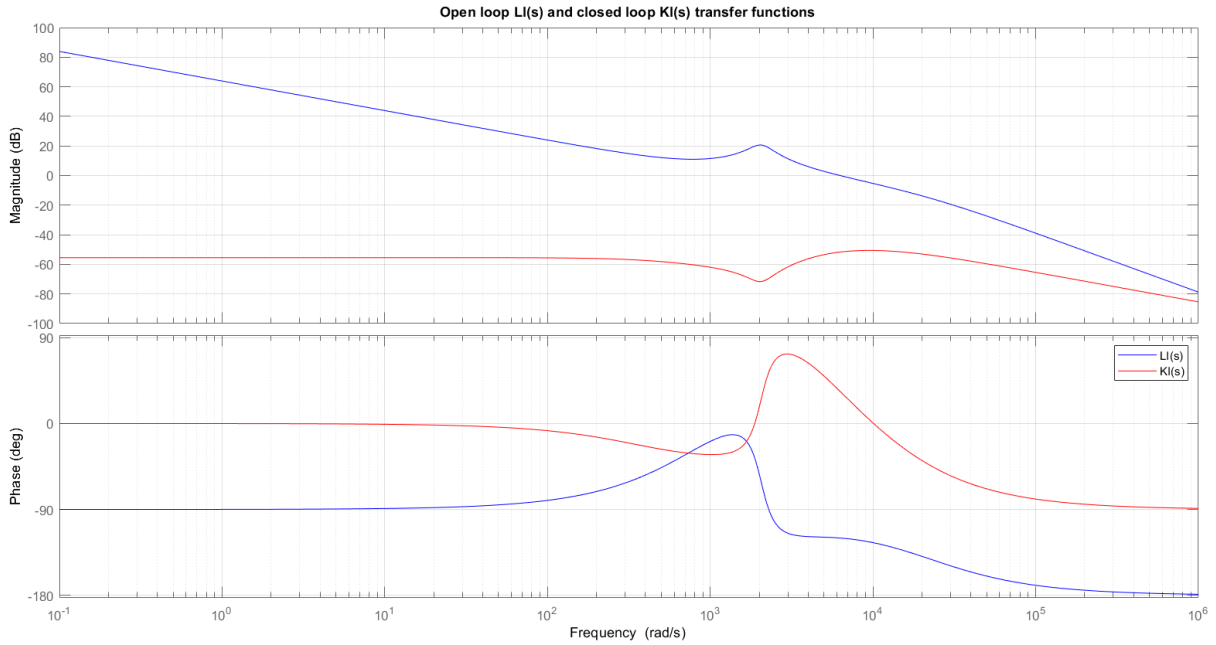


**Figure 45 –** Open loop LI(s) and closed loop KI(s) transfer functions – MDIBC

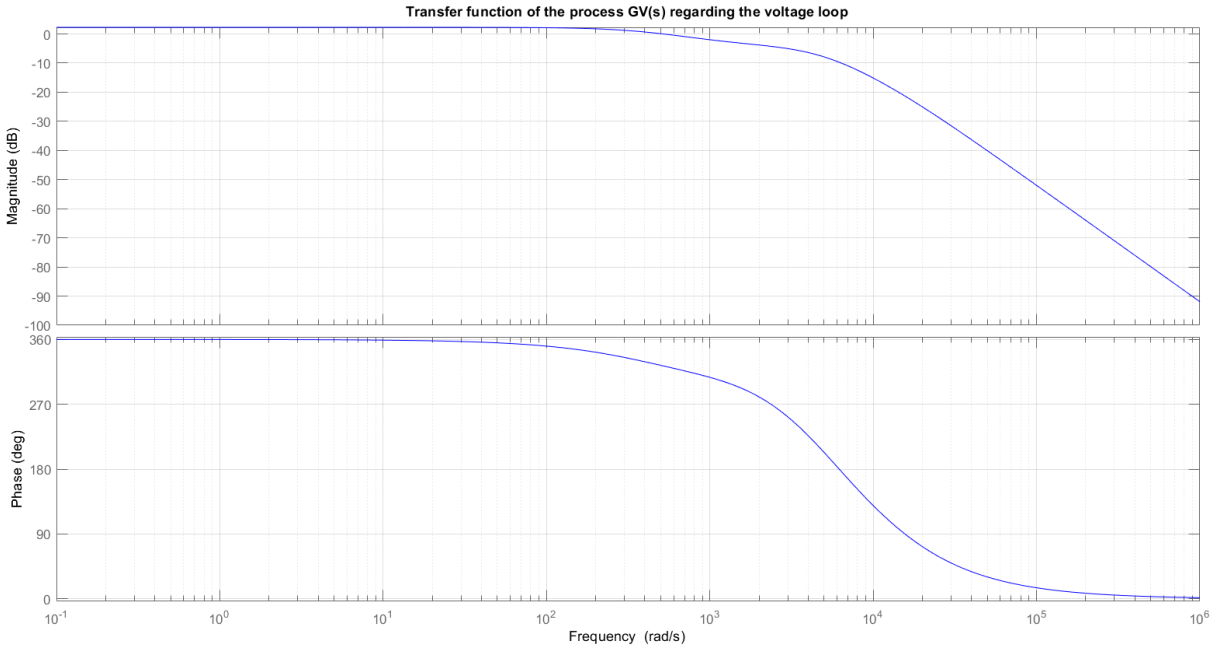


**Figure 46 –** Transfer function GV – MDIBC

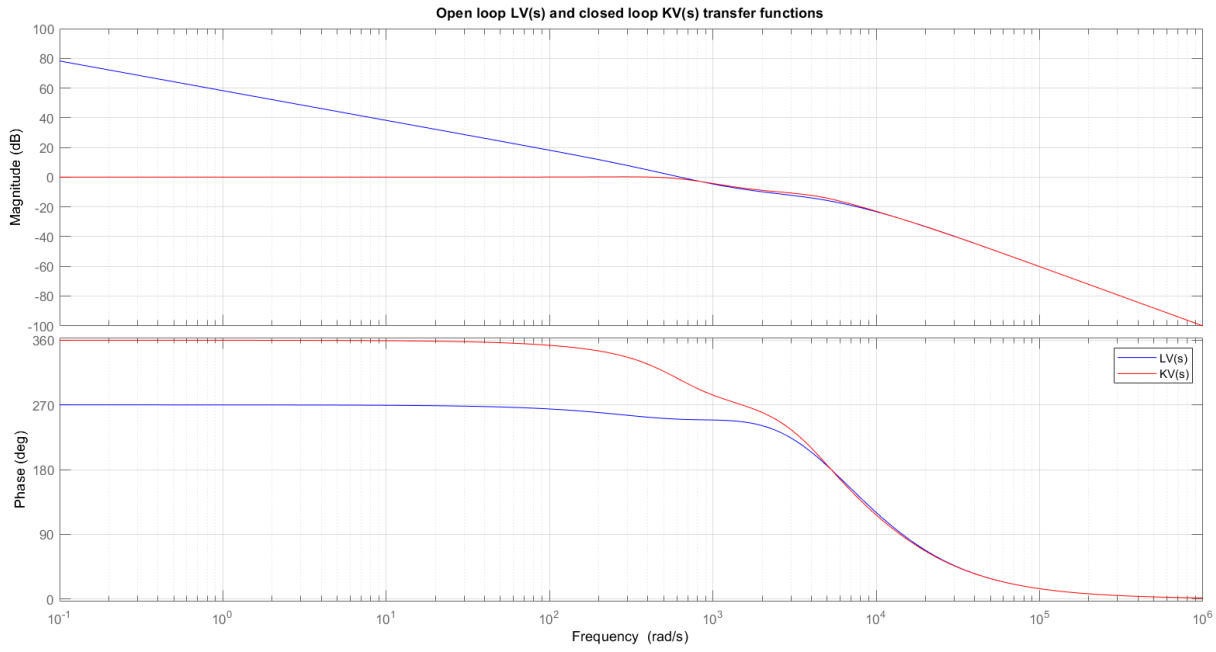


**Figure 47 –** Open loop LV(s) and closed loop KV(s) transfer functions – MDIBC

- IBC

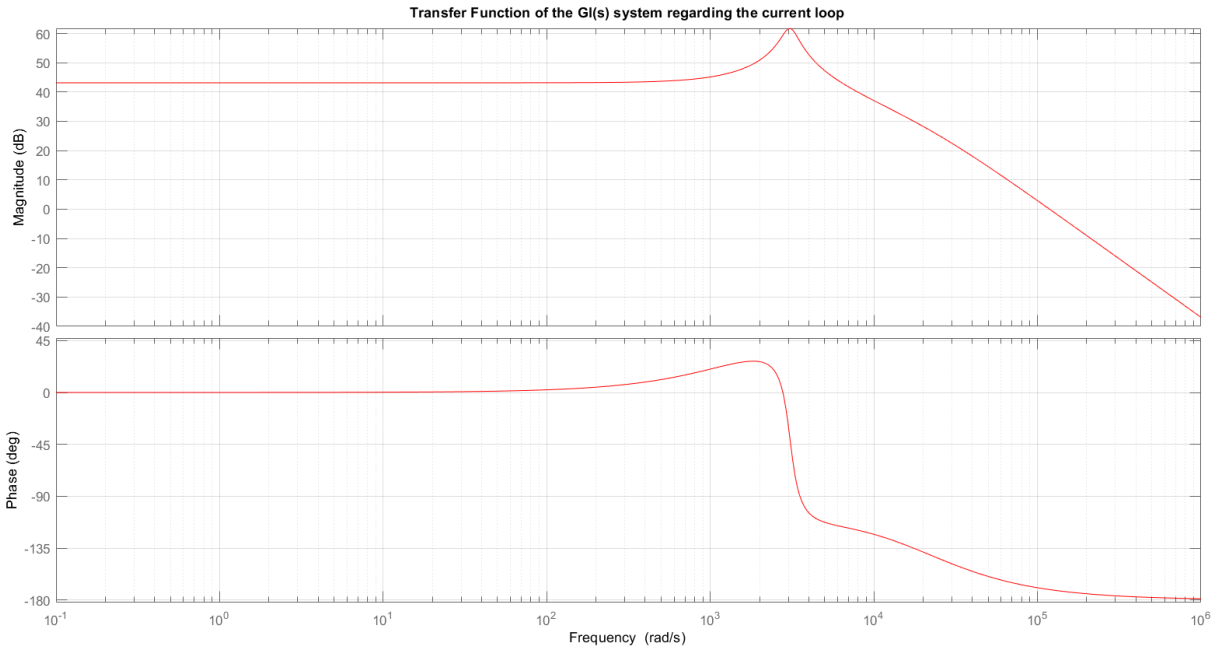


**Figure 48 –** Transfer function GI – IBC

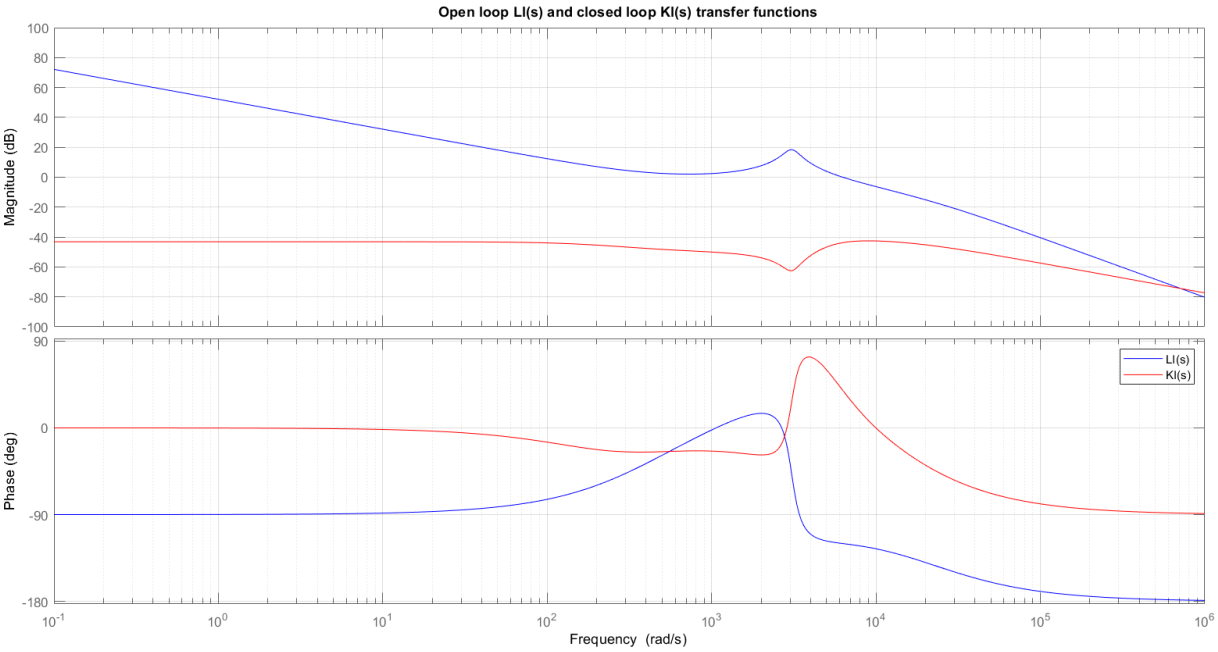


**Figure 49 –** Open loop LI(s) and closed loop KI(s) transfer functions – IBC

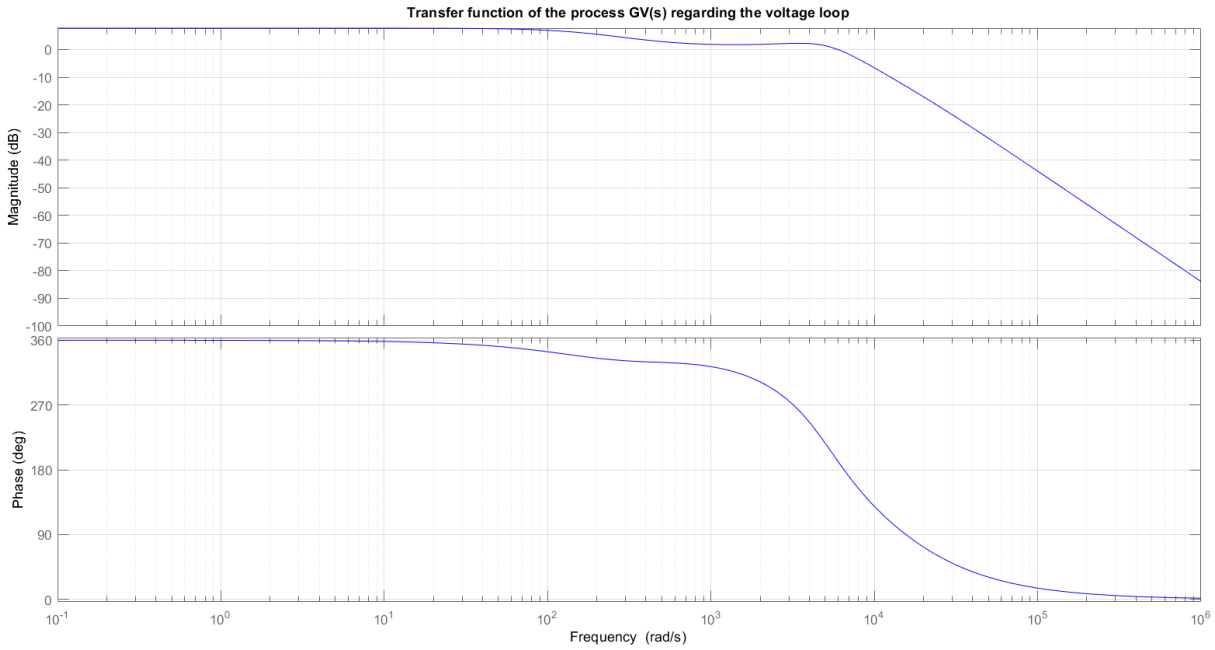


**Figure 50 –** Transfer function GV – IBC

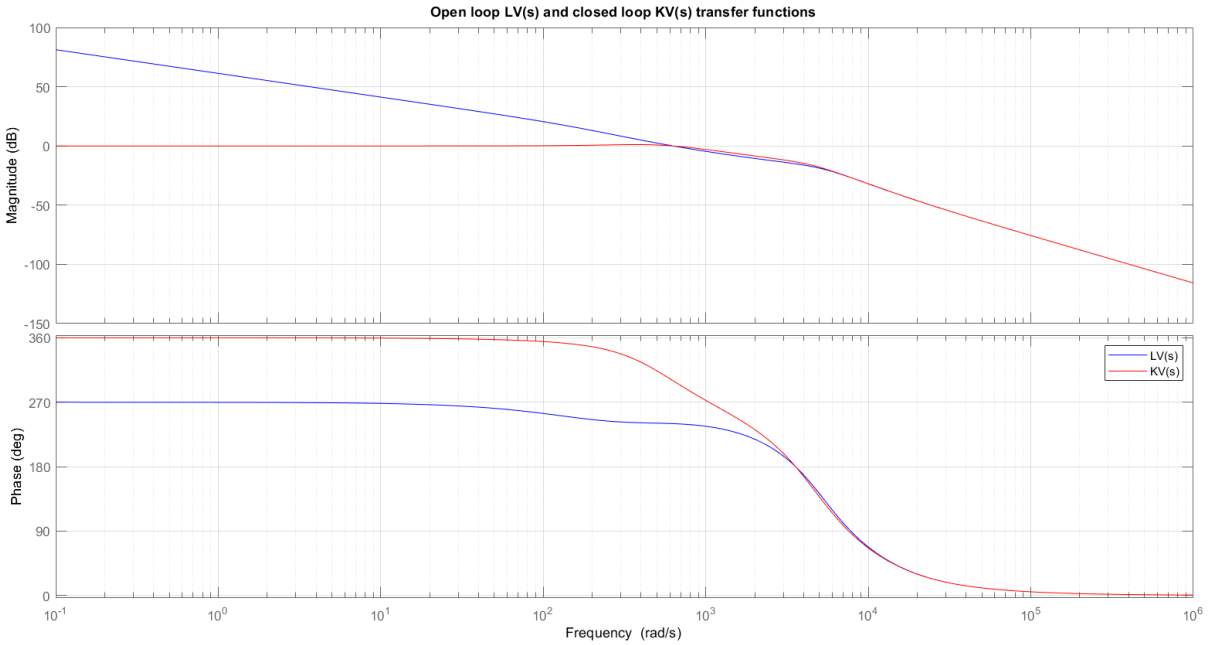


**Figure 51 –** Open loop LV(s) and closed loop KV(s) transfer functions – IBC

- MDBC

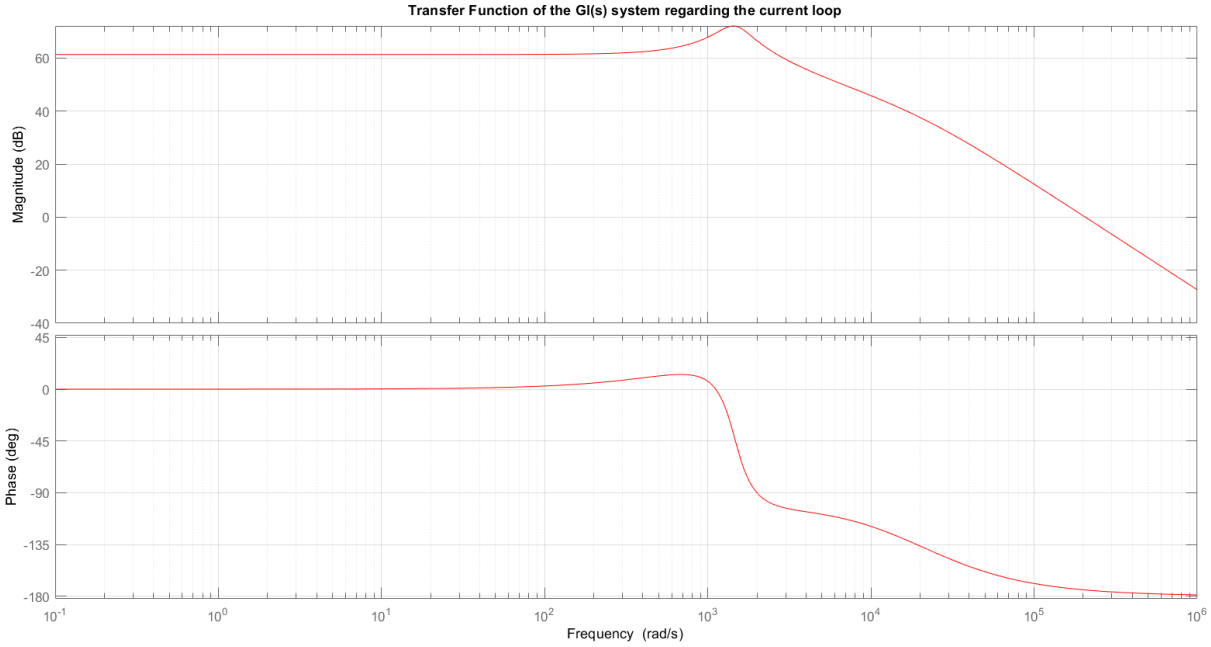


**Figure 52 –** Transfer function GI – MDBC

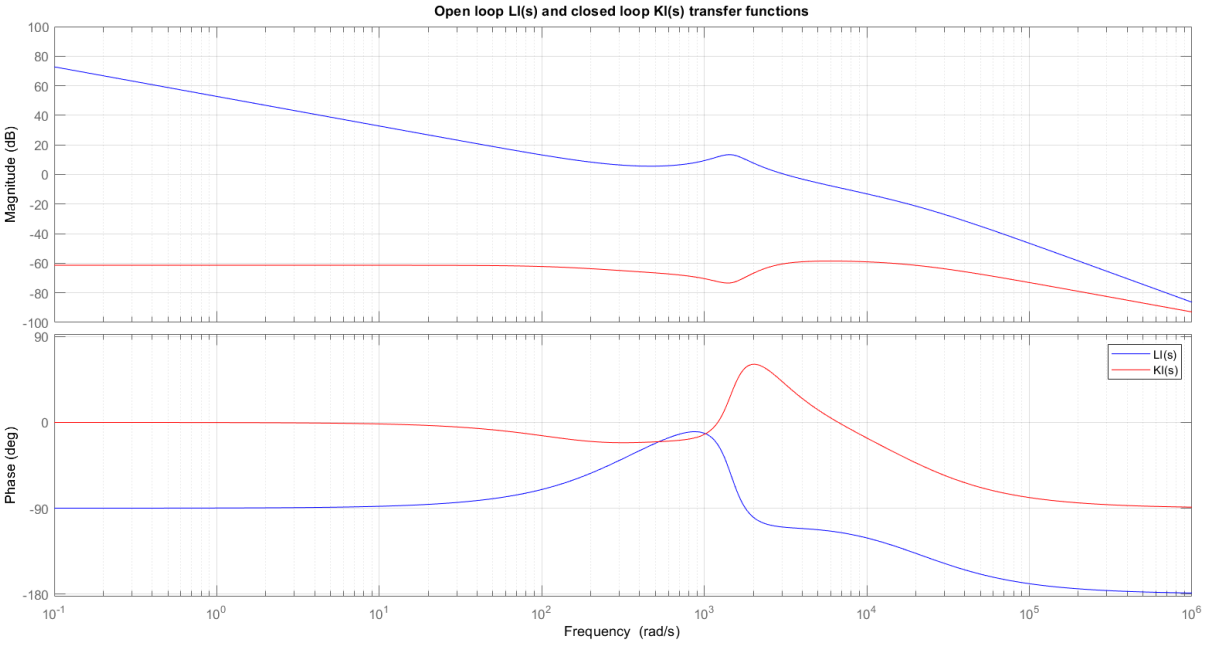


**Figure 53 –** Open loop LI(s) and closed loop KI(s) transfer functions – MDBC

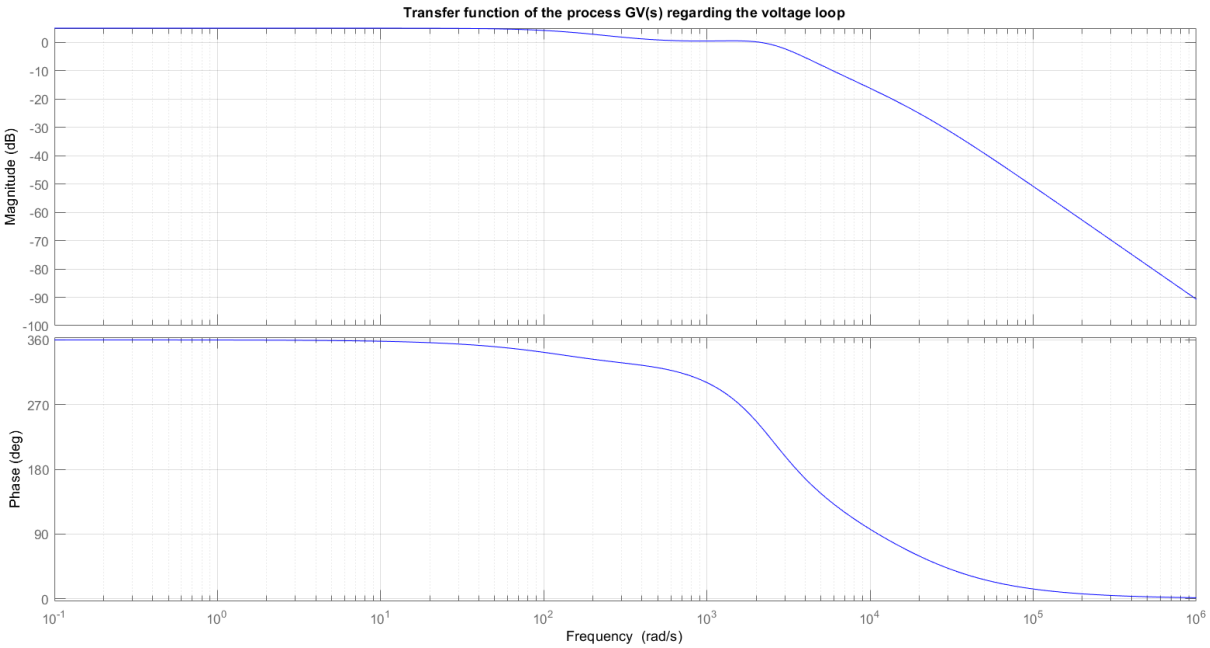


**Figure 54 –** Transfer function GV – MDBC

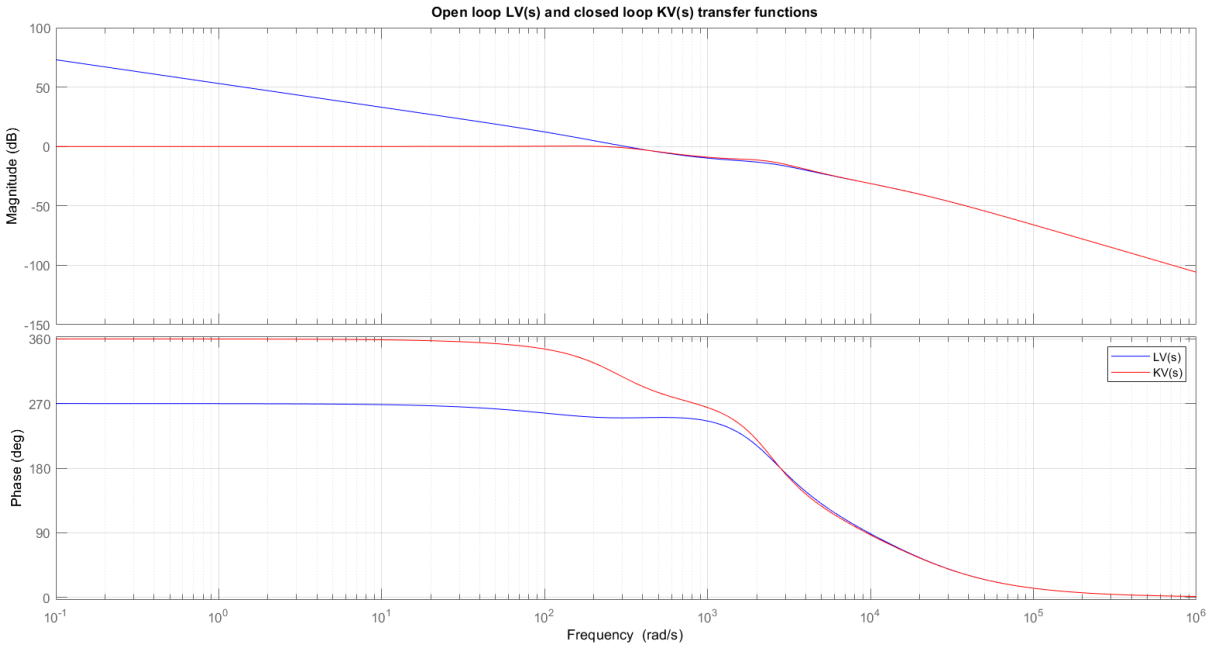


**Figure 55 –** Open loop LV(s) and closed loop KV(s) transfer functions – MDBC

# 7. SIMULATION AND RESULTS

The simulations are performed in Matlab/Simulink. The simulation can be divided in two parts, the electric circuit and the controller. In the electric circuit two circuit breakers are included: one between the capacitor and the diode outputs, the other circuit breaker is between the capacitor and the load. These circuit breakers are used to charge the capacitor before to be connected to the load, as illustrated in the electric circuit of the MDIBC (figure 56).

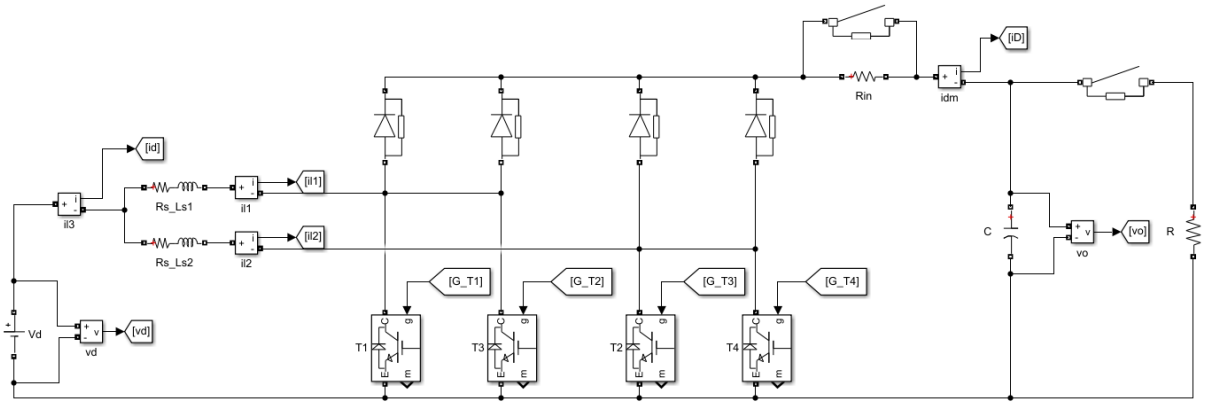


**Figure 56 –** Electric circuit of the MDIBC in Simulink

To guarantee that the switching will start only after the capacitor is charged, the enable block starts only after the signal $t\_start$, as can be seen in the figure 57. Moreover, after each output from the regulation block there is a 2-input Logic AND Gate, in which the second input is the signal $t\_start$. The output of the logic gate AND is the gate signal of the IGBTs; this logic is illustrated in the figure 58. This means that the drive gate signals will only be different than zero after the time $t\_start$.

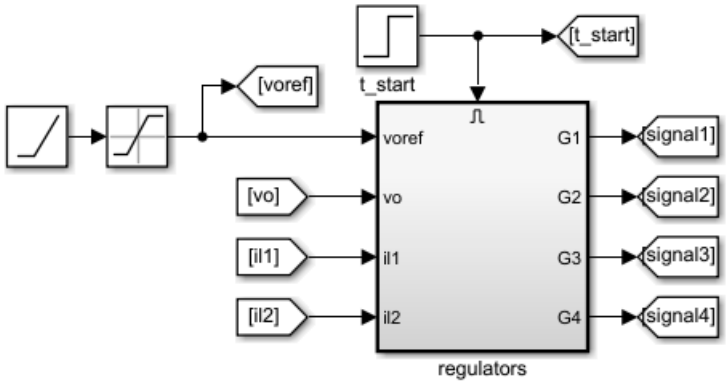


**Figure 57 –** Regulator block

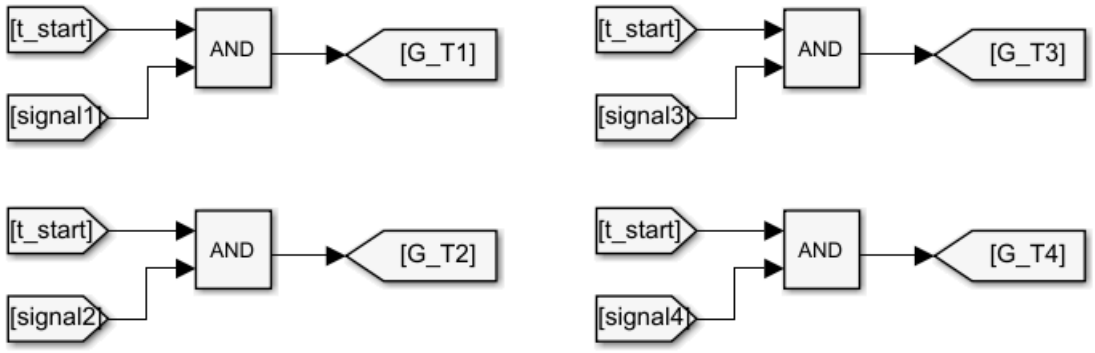


**Figure 58 –** Start logic for the drive gate signal

The controller part is shown in the figure 59.

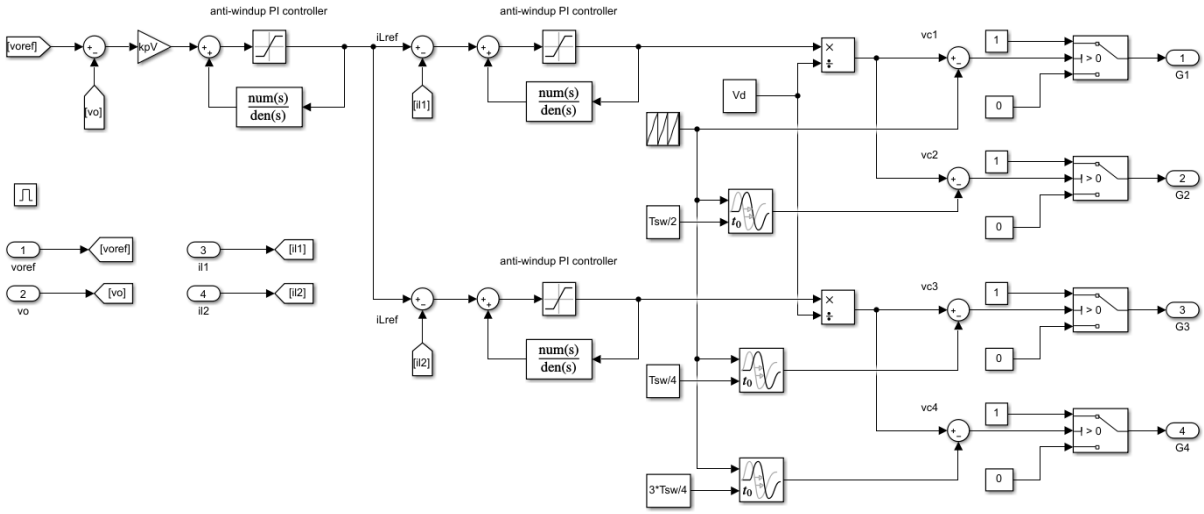


**Figure 59 –** Controller diagram MDIBC in Simulink

From the figure 59, it is possible to identify properties and the blocks from the controller part. Firstly, the regulators are not simple PI transfer functions blocks, but anti-windup PI controllers as shown in the figure 60. This solution was chosen because it guarantees stability. As a saturation block is added to the controller diagram, the output is limited, and it avoids the divergence of the integral error, hence the integral error is kept small. For the voltage controller, in the saturation block the limit value is set at the steady stated current value $(I_L)$. For the current controller, the saturation block limit is the input voltage $(V_d)$.

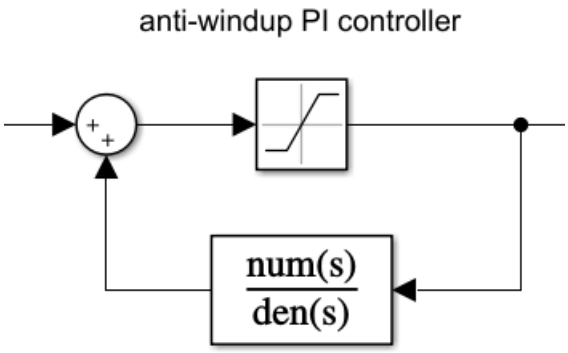


**Figure 60 –** Anti-windup PI controller

From the output of the voltage regulator, two branches are derived, one for each current inductor ($i_{L1}$ and $i_{L2}$). The output of the current regulator is divided by a constant value, in this case, the input voltage $V_d$. This ratio is the voltage control and it is limited to $0 < v_c < 1$. From the output of the ratio block, two control signals are originated, one for each parallel leg per phase. Finally, these voltages control are compared to the same saw-tooth wave ($v_{st}$), but time delayed in $\frac{T_{sw}}{4}$ from each other, i.e., $v_{c1}$ is compared to $v_{st}$, the $v_{c3}$ is compared to the $v_{st}$ delayed by $\frac{T_{sw}}{4}$, the $v_{c2}$ is compared to $v_{st}$ delayed by $\frac{T_{sw}}{2}$ and $v_{c4}$ is compared to $v_{st}$delayed by $\frac{3}{4}T_{sw}$. If $v_c > v_{st}$, it is applied a logic signal equal to one to the gate, if $v_c < v_{st}$, a logic signal equal to zero is applied. It is important to notice that the index of the $v_c$ represents which IGBT is being controlled, for example: $v_{c1}$ controls the gate signal of $G_1$. The comparison of the control voltage $v_c$ with $v_{st}$ delayed in $\frac{360^o}{mn}$ provides the interleaved control strategy.

The other converters, IBC (figures 61 and 62) and MDBC (figures 63 and 64), have the similar work principle.

In the case of converter which presents two phases, MDIBC and IBC, the output of the voltage regulator, $i_{L\,ref}$, is divided in two branches, one for each phase. For the converters which presents two parallel legs per phase, MDIBC and MDBC, the control voltage is the same, but they are compared to different carrier signals.

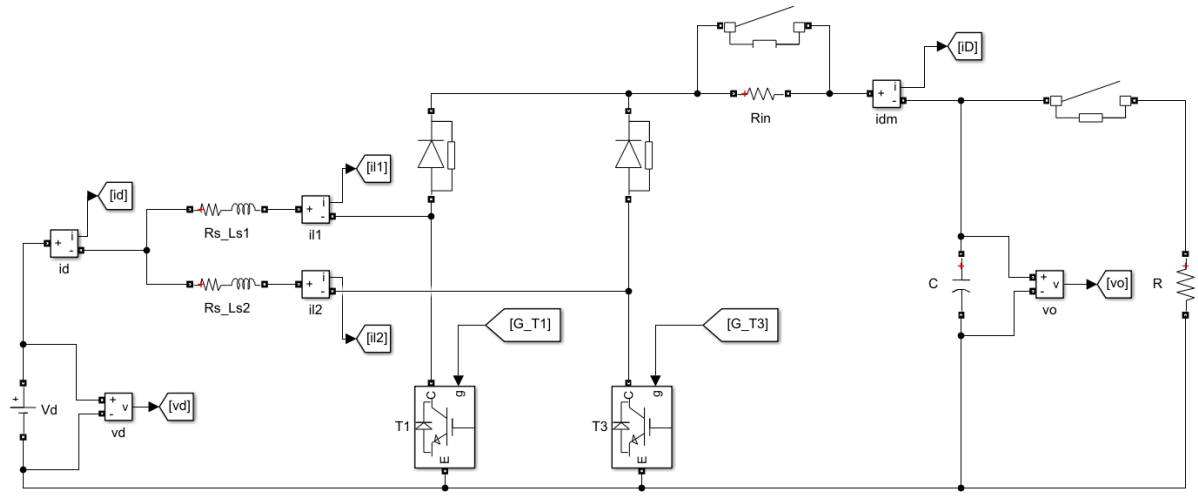


**Figure 61 –** Electric circuit of the IBC in Simulink

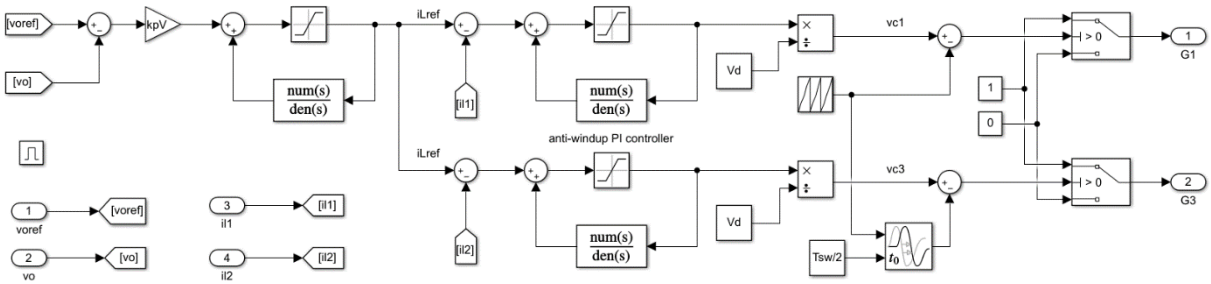


**Figure 62 –** Controller diagram MDIBC in Simulink

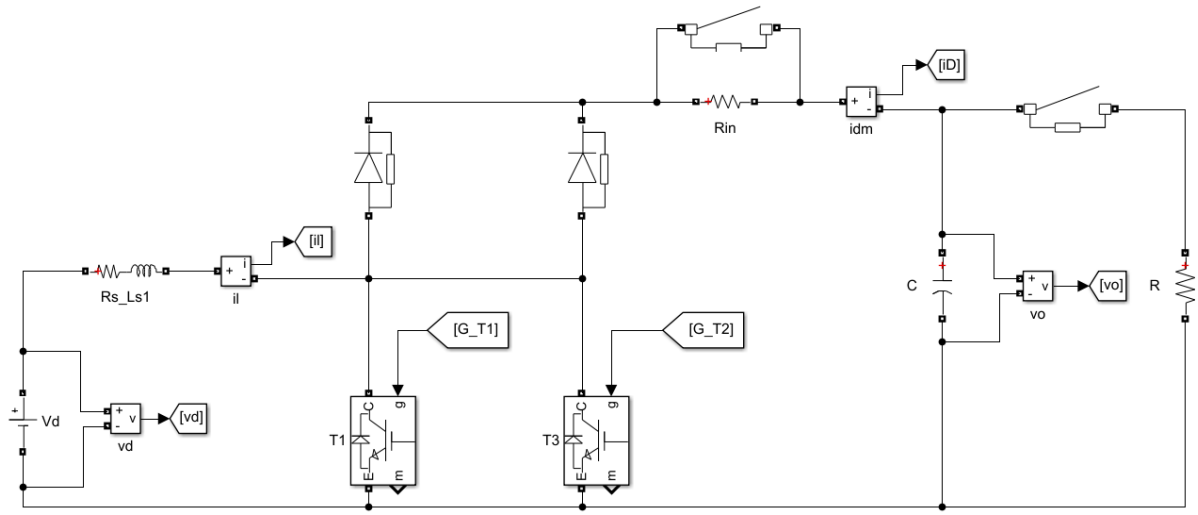

**Figure 63 –** Electric circuit of the IBC in Simulink

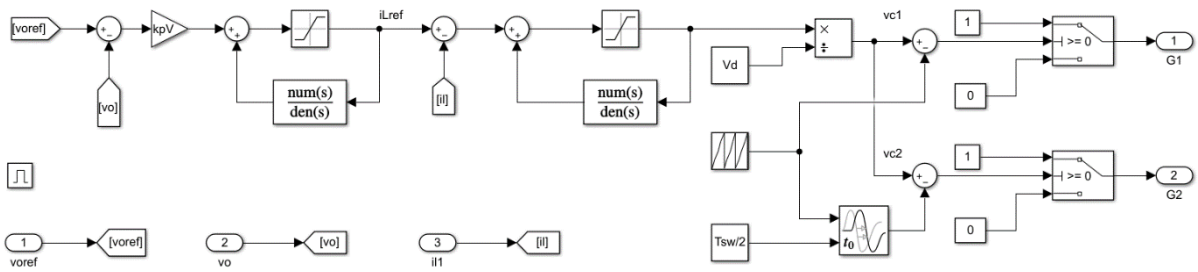


**Figure 64 –** Controller diagram MDIBC in Simulink

To observe the behaviour of the output voltage, the output voltage reference $(v_{o\,ref})$ is simulated as ramp source voltage. A saturation block is connected to the ramp source, upper limit is set as the steady state output voltage. This limit is different for each converter topology as shown in the tables 5, 10 and 13.

Figure 65 shows the variation of $v_{o\,ref}$ (orange curve) and $v_o$ (blue curve) with respect to time $(t)$.

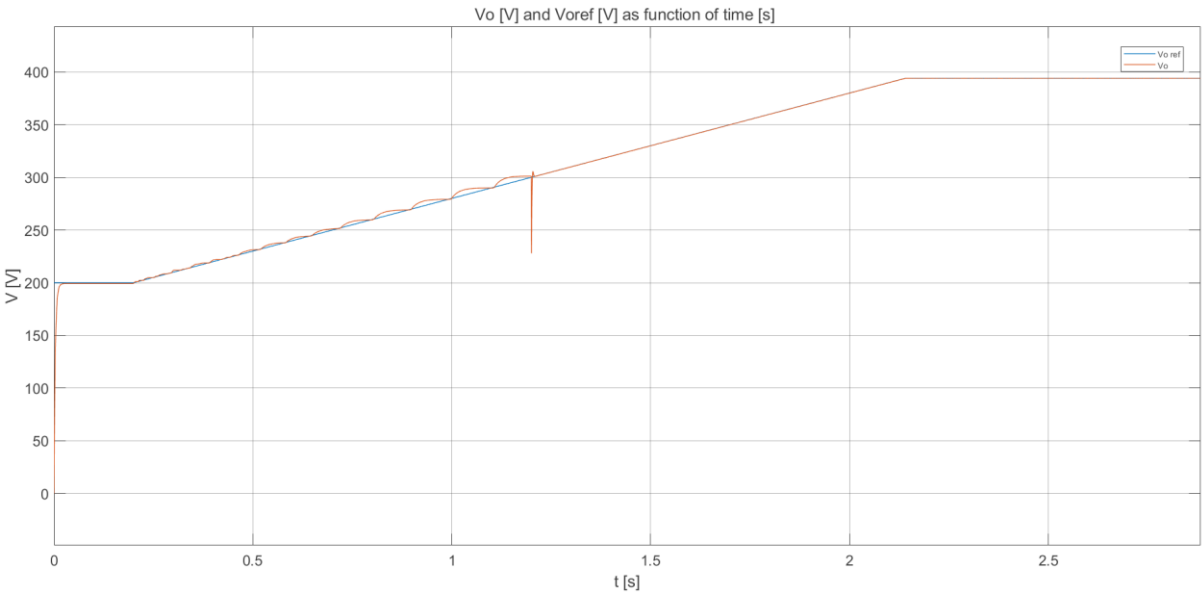


**Figure 65 –** $v_o$ vs. t (orange curve) and $v_{o\,ref}$ vs. t (blue curve) for the MDIBC

It is possible to notice that the $v_o$ does not reach the 400 V as indicated $v_{o\,ref}$. This can be explained from (13), in which to calculate $v_o$ non-ideal parameters were neglected, such as the line resistance, the IGBTs and diodes resistance. Observe that the orange line reaches a value close to $V_d$ in 0.025 seconds, which is the time to

charge the shunt capacitor. When the time is equal to 0.2 seconds, $v_o$ starts to increase and the regulators are enabled. Then, after one second, the circuit breaker between the shunt capacitor and the load closes, in this time instant, a ripple in the $v_o$ is observed. Figure 66 shows $v_o$ in the steady state condition, from the graph $v_o = 394.72 \pm 0.02\ [V]$, hence, the voltage ripple is equal to 0.0051%.

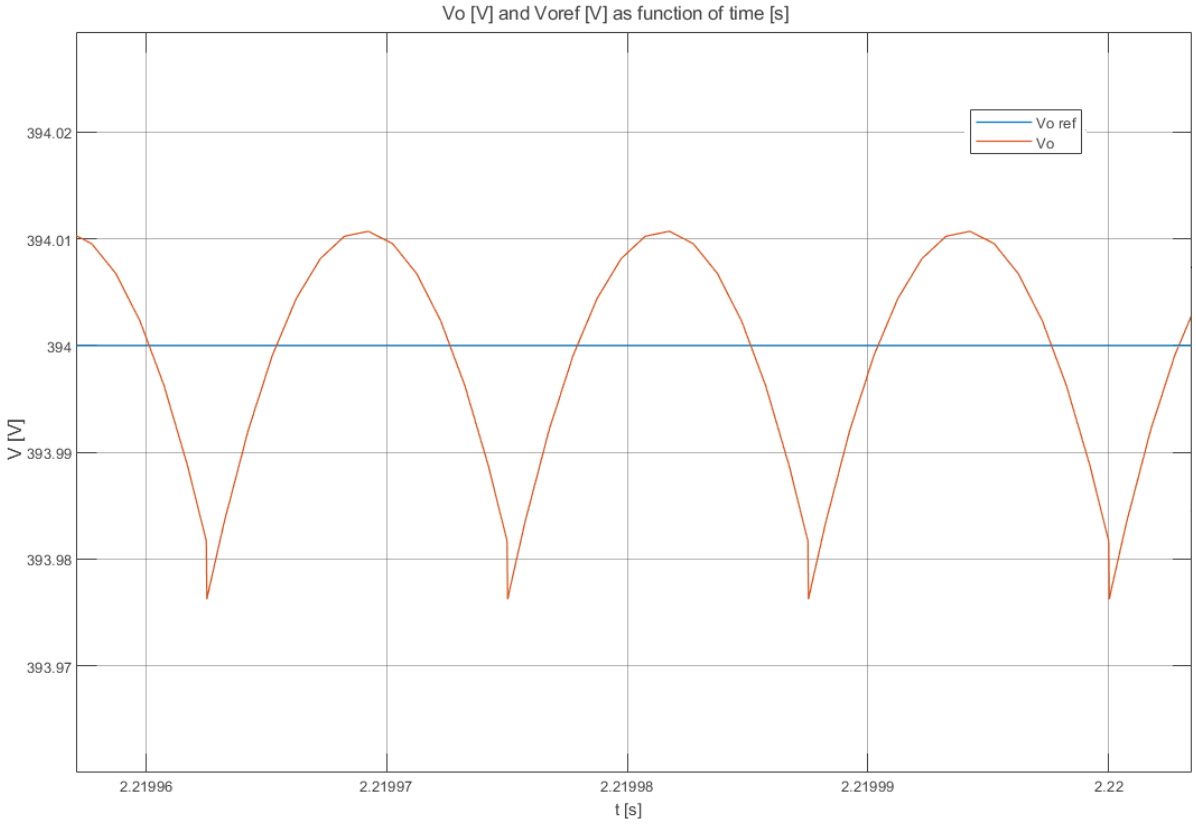


**Figure 66 –** $v_o \text{vs.t}$ (orange curve) and $v_{o\,ref}$ vs.t (blue curve) for the MDIBC in steady state condition for the MDIBC

In the figure 67, it is shown the current from the source (green curve) and the inductor currents (orange curve). The average value of the source current $(i_d)$ is, as predicted, the double of the current inductor $(i_L)$ value. To calculate the ripple of the current inductor, it is considered the period in which the switch is off and the resistances are neglected. For the three configurations the equation from KVL is the same (equation 58). The main difference among the three configurations is the integration interval.

$$V_d - L\frac{di_L}{dt} - V_o = 0 \tag{58}$$

Then, isolating the variation of the current inductor in the left side and integrating it with respect to time, it is possible to calculate the current ripple for the three cases. The equations 59, 60 and 61 show the formulas to calculate the current ripple for the MDIBC, IBC and MDBC respectively.

$$\Delta i_L^- = \frac{V_d - V_o}{L}\int_{d.T_s}^{\frac{T_s}{mn}} dt = \frac{V_d - V_o}{mnLf_s}(1 - mnd) \tag{59}$$

$$\Delta i_L^- = \frac{V_d - V_o}{L}\int_{d.T_s}^{\frac{T_s}{n}} dt = \frac{V_d - V_o}{nLf_s}(1 - nd) \tag{60}$$

$$\Delta i_L^- = \frac{V_d - V_o}{L}\int_{d.T_s}^{\frac{T_s}{m}} dt = \frac{V_d - V_o}{mLf_s}(1 - md) \tag{61}$$

Moreover, it is possible to notice from the figures that the source current ripple is lower than the inductor current ripple. This phenomenon can be explained from the interleaved current between the two phases, as shown in the figure 68. The reduction of current inductor ripples has a benefit effect in batteries or fuel cells, due to a lower current ripple implies in a lower heat source, which could damage the source, and, hence, a higher the life span.

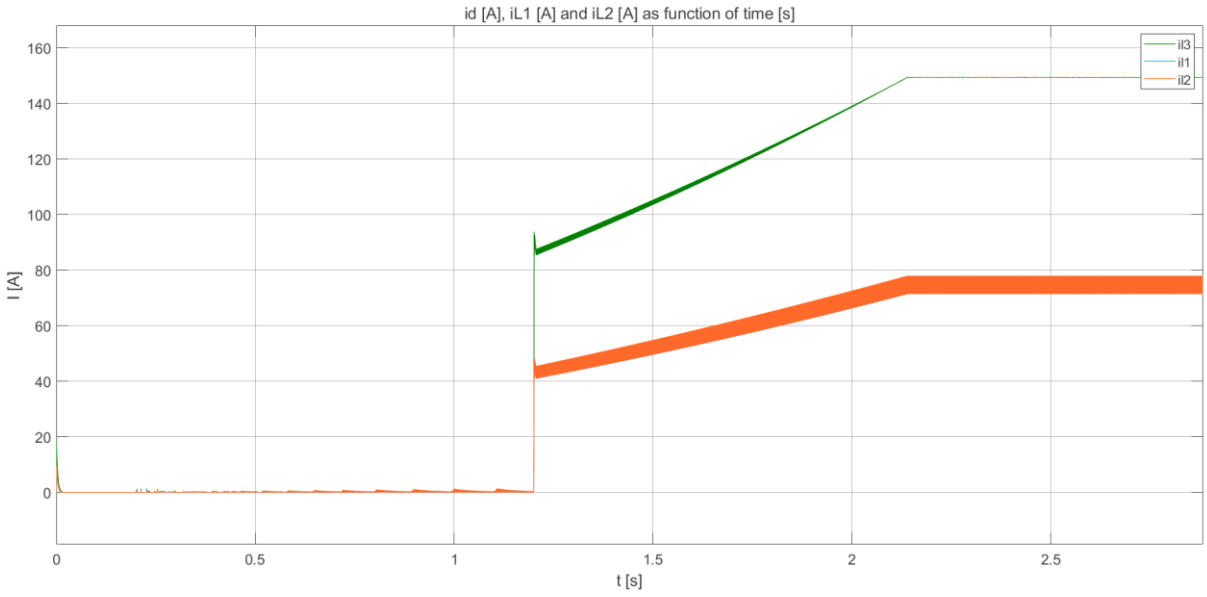

**Figure 67 –** $i_d\ vs.t$ (green curve), $i_{L1}vs.t$ (blue curve) and $i_{L2}vs.t$ (orange curve) for MDIBC

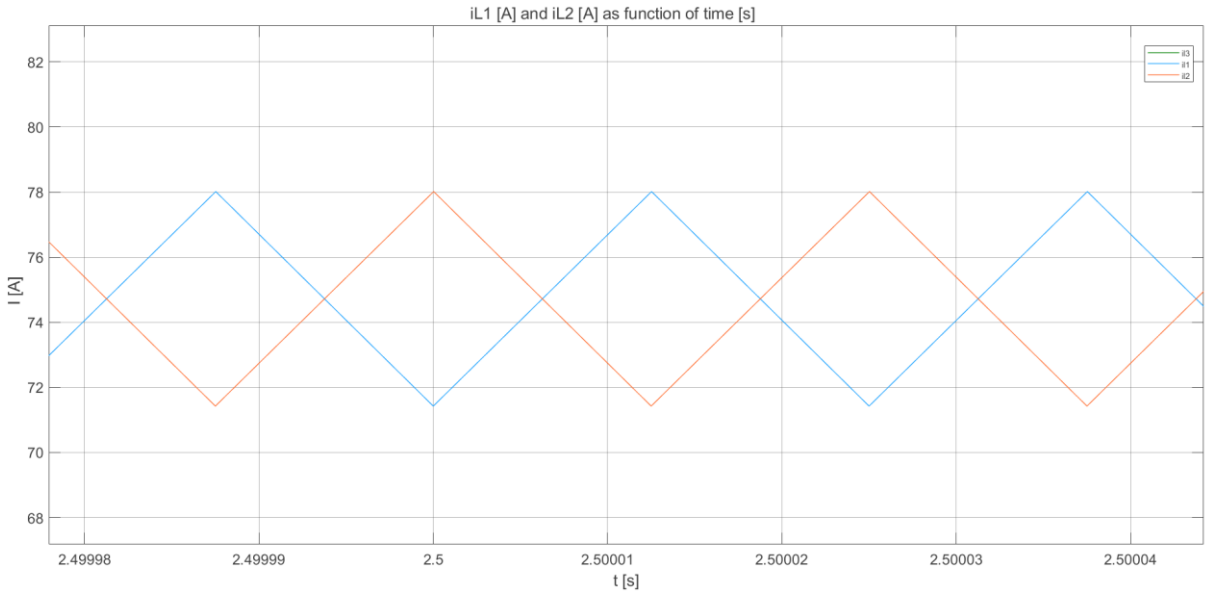


**Figure 68 –** $i_{L1}vs.t$ (blue curve) and $i_{L2}vs.t$ for MDIBC (orange curve) for MDIBC

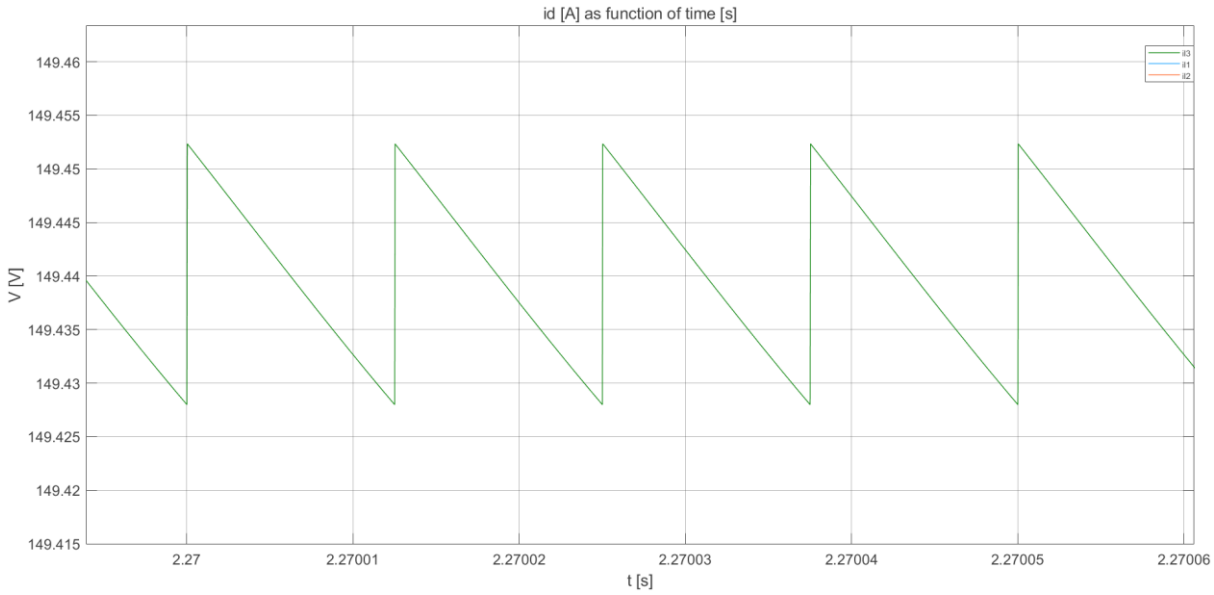


**Figure 69 –** $i_d\ vs.t$ for MDIBC

Comparing the figures 68 and 69, the frequency of the source current is twice the frequency of the inductor, as predicted in chapter 3. Moreover, from the same

figures, $i_{L1} = i_{L2} = 75.0 \pm 3.5$ [A] and $i_d = 150 \pm 0.025\,[A]$. Therefore, the inductor current ripple is limited to $4.6\%$ and the source current ripple to $0.02\%$.

Figure 70 to 73 show the graphs of the output voltage and current inductor to the IBC.

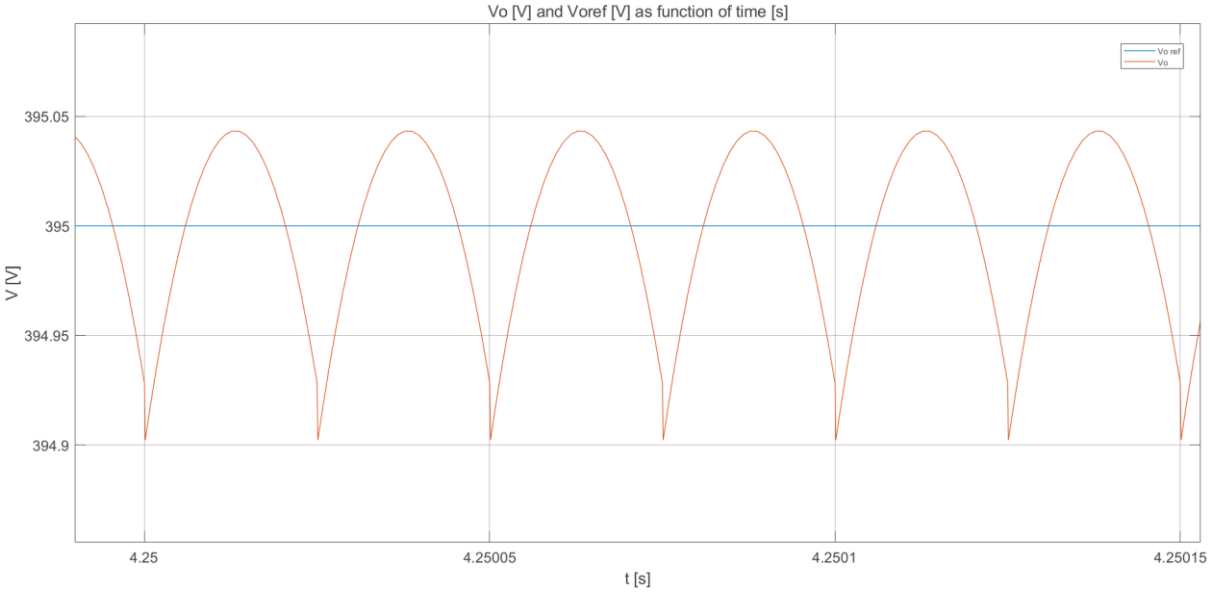


**Figure 70 –** $v_o$vs.t (orange curve) and $v_{o\,ref}$ vs.t (blue curve) for the IBC in steady state condition

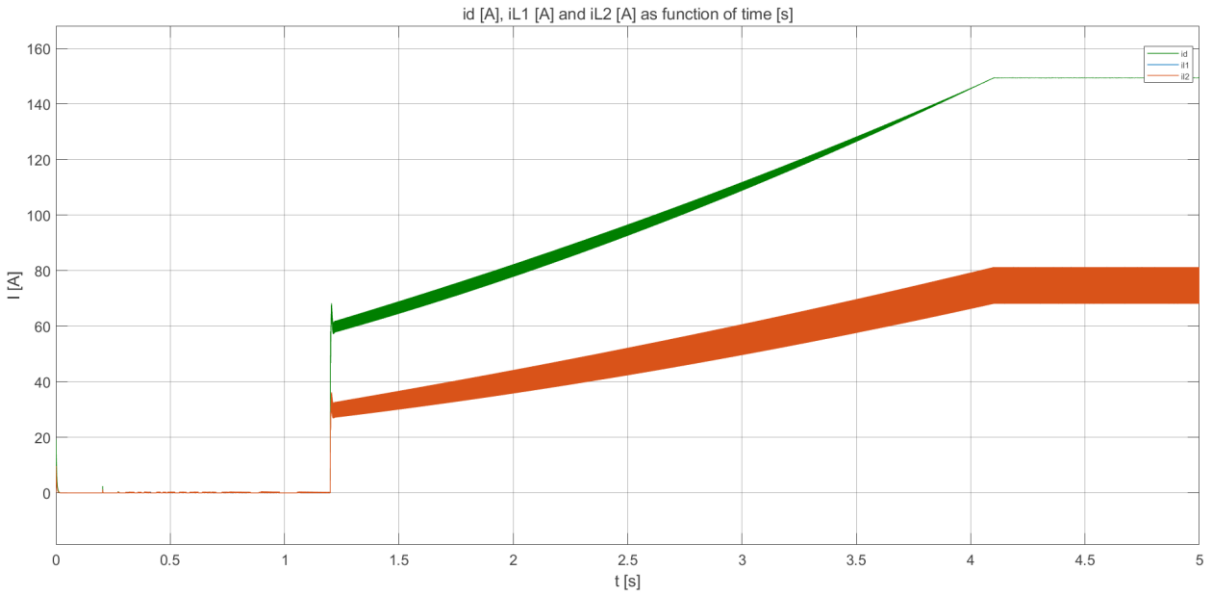


**Figure 71 –** $i_d\ vs.t$ (green curve), $i_{L1}vs.t$ (blue curve) and $i_{L2}vs.t$ (orange curve) for IBC

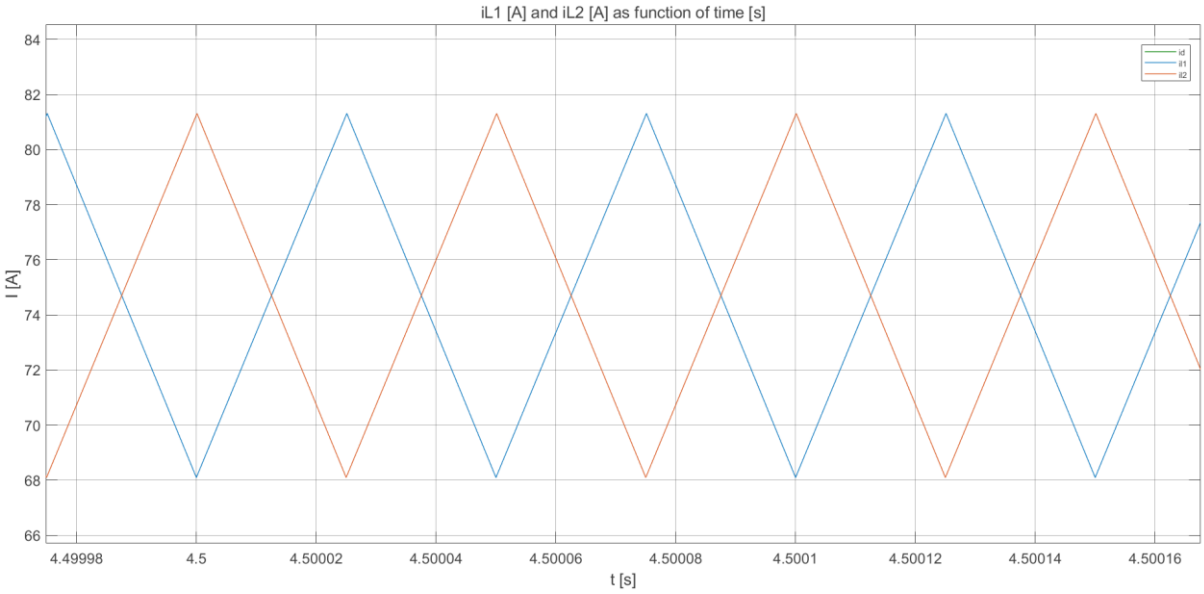


**Figure 72 –** $i_{L1} vs. t$ (blue curve) and $i_{L2} vs. t$ for MDIBC (orange curve) for IBC

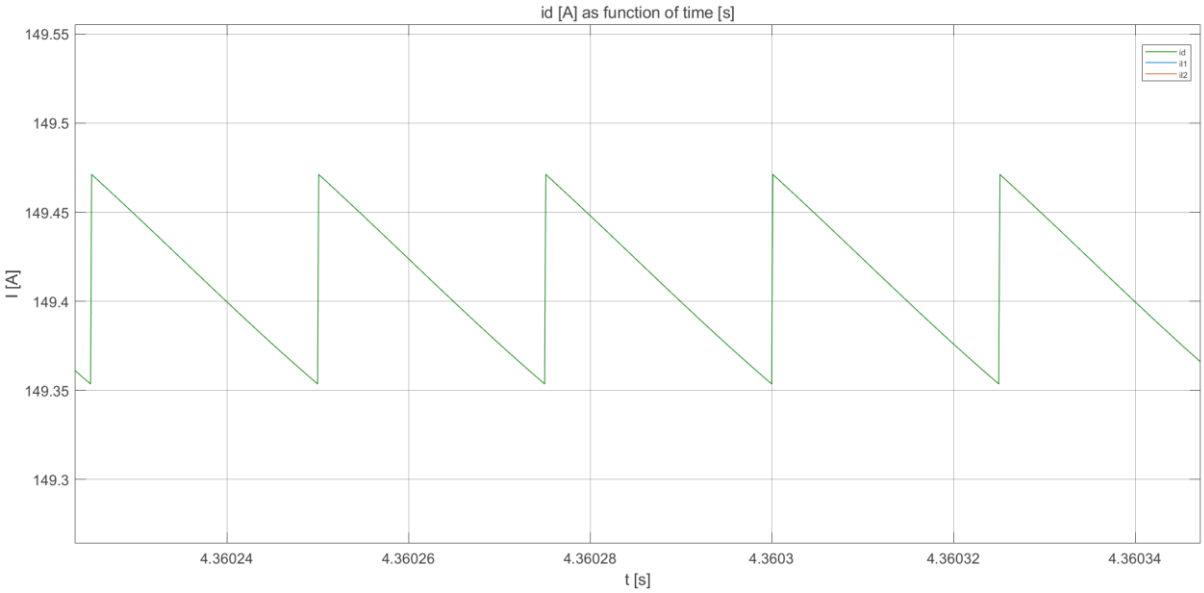


**Figure 73 –** $i_d \ vs. t$ for IBC

From the figure 70, $v_o = 396 \pm 0.053\ [V]$, therefore the output voltage ripple is limited to $0.013\%$. According to the figures 72 and 73, the total current and current inductor are equal to $i_d = 150.0 \pm 0.80\ [A]$ and $i_{L1} = i_{L2} = 75 \pm 7\ [A]$. Therefore, the source current and the inductor current ripple are limited to $0.53\%$ and $9.33\%$.

The characteristics of the MDBC are shown in the figure 74 to 75 show the graphs of the output voltage and current inductor to the MDBC.

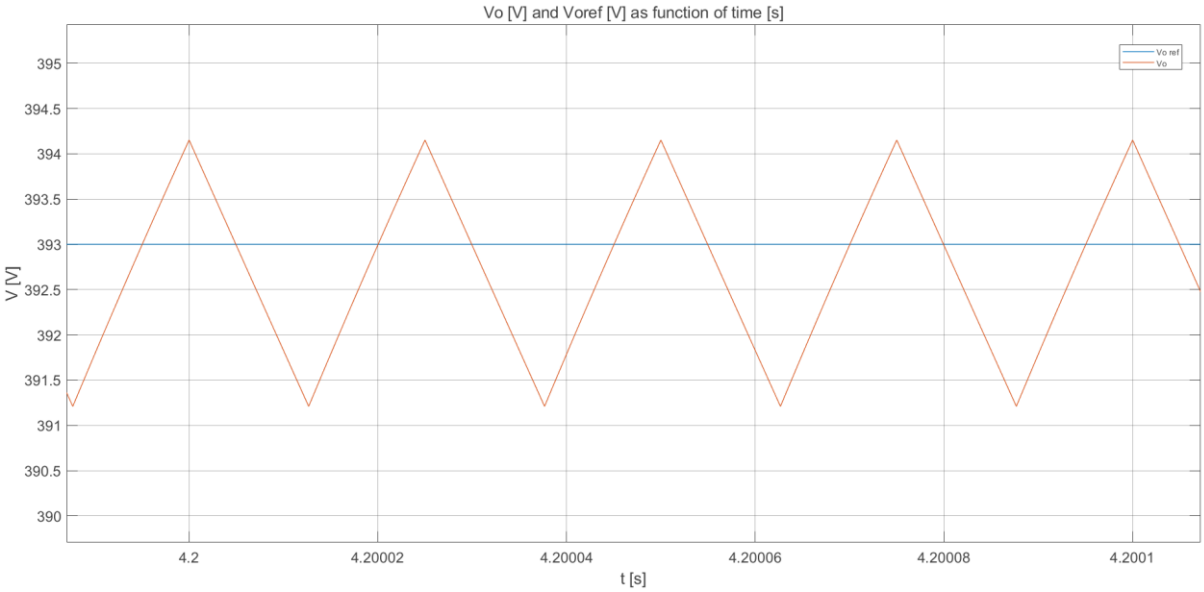


**Figure 74 –** $v_o \text{vs.t}$ (blue curve) and $v_{o\,ref}$ vs.t (orange curve) for the MDBC in steady state condition

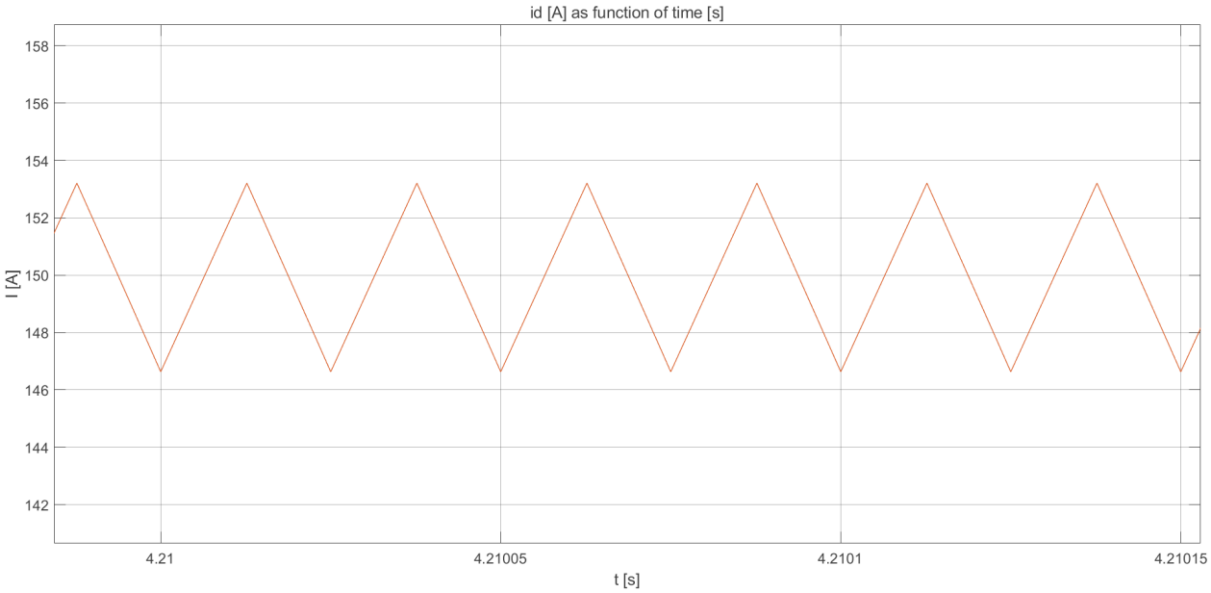


**Figure 75 –** $i_d \; vs. t$ for MDBC

Figure 74 shows the output voltage when the converter is in steady state, according to the figure the value of $v_o = 393.0 \pm 1.3\,[V]$. The value of the current

inductor, as reported by the figure 75, is $i_L = 150.0 \pm 3.3$ [A]. The output voltage ripple is limited to $0.33\%$, the inductor current ripple is equal to $2.2\%$.

Table 20 describes the values of the output voltage ripple $(v_o)$, the source current $(i_d)$ and the current inductor $(i_L)$ ripple for each topology.

**Table 20 –** Output voltage, total current and inductor current ripple for each topology

| **Converter topology** | **Output voltage ripple** $\left(\frac{\Delta V_o}{V_o}\right)$ | **Source current** $\left(\frac{\Delta I_d}{I_d}\right)$ | **Current inductor** $\left(\frac{\Delta I_L}{I_L}\right)$ |
|---|---|---|---|
| MDIBC | $0.0051\%$ | $0.02\%$ | $4.6\%$ |
| IBC | $0.013\%$ | $0.53\%$ | $9.33\%$ |
| MDBC | $0.33\%$ | $2.2\%$. | $2.2\%$ |

From the table 20, it is possible to notice that the proposed converter ripple values are the half when compared to the IBC and much lower when compared to the MDBC. These values of output voltage and current inductor ripple are in accordance with the assumptions used to calculate the component values.

# 8. CONCLUSION

In this work, it is presented a unidirectional DC/DC converter, the multidevice interleaved boost converter (MDIBC), which would be a suitable choice to optimize the drive system fed by fuel cell. This converter is compared to other two converter topologies, the interleaved boost converter (IBC) and the multidevice boost converter (MDBC). For the three topologies, it was analysed the switching characteristic and boundaries. Moreover, the small signal model and losses analysis is deduced. Finally, it is designed a dual loop control strategy to perform the simulations.

The simulations show that, using the same component values, the MDIBC can increase the current ripple frequency and reduce the value of the output voltage and the current ripple is significantly which would imply a size reduction of the passive components, therefore the size and weight reduction of the converter. A lower current inductor ripple would also slow the aging process in the fuel cell.

In a nutshell, regarding the efficiency and the performance of the converter, it seems to be a good solution for automotive application, when compared to the other two converter topologies.

## 9. REFERENCE

[1] R. Matulka, “The History of the Electric Car”. U.S. Department of Energy. September 15th, 2014. Available in: https://www.energy.gov/. Access in: November 12th, 2018.

[2] ELECTRONIC DICTIONARY Merriam-Webster Unabridged. Springfield, Massachusetts, EUA. Available in: http://unabridged.merriam-webster.com/. Access in: November 12th, 2018.

[3] R. A. Dougal, S. Liu and R. E. White, "Power and life extension of battery-ultracapacitor hybrids," in *IEEE Transactions on Components and Packaging Technologies*, vol. 25, no. 1, pp. 120-131, March 2002.

[4] O. Hegazy, M. El Baghdadi, J. Van Mierlo, P. Lataire and T. Coosemans, "Analysis and modelling of a bidirectional multiport DC/DC power converter for battery electric vehicle applications," 2014 1*6th European Conference on Power Electronics and Applications*, Lappeenranta, 2014, pp. 1-12.

[5] O. Hegazy, R. Barrero, J. Van Mierlo, P. Lataire, N. Omar and T. Coosemans, "An Advanced Power Electronics Interface for Electric Vehicles Applications," in *IEEE Transactions on Power Electronics*, vol. 28, no. 12, pp. 5508-5521, Dec. 2013.

[6] J. W. Shim, Y. Cho, S. Kim, S. W. Min and K. Hur, "Synergistic Control of SMES and Battery Energy Storage for Enabling Dispatchability of Renewable Energy Sources," in *IEEE Transactions on Applied Superconductivity*, vol. 23, no. 3, pp. 5701205-5701205, June 2013, Art no. 5701205.

[7] F. Akar, Y. Tavlasoglu, E. Ugur, B. Vural and I. Aksoy, "A Bidirectional Nonisolated Multi-Input DC–DC Converter for Hybrid Energy Storage Systems in Electric Vehicles," in *IEEE Transactions on Vehicular Technology*, vol. 65, no. 10, pp. 7944-7955, Oct. 2016.

[8] O. Hegazy, J. V. Mierlo and P. Lataire, "Analysis, Modeling, and Implementation of a Multidevice Interleaved DC/DC Converter for Fuel Cell Hybrid Electric Vehicles," in *IEEE Transactions on Power Electronics*, vol. 27, no. 11, pp. 4445-4458, Nov. 2012.

[9] O. Hegazy, J. Van Mierlo and P. Lataire, "Analysis, control and comparison of DC/DC boost converter topologies for fuel cell hybrid electric vehicle applications," *Proceedings of the 2011 14th European Conference on Power Electronics and Applications*, Birmingham, 2011, pp. 1-10.

[10] O. Ellabban, J. Van Mierlo, P. Lataire and P. Van den Bossche, "Z-source inverter for vehicular applications," *2011 IEEE Vehicle Power and Propulsion Conference*, Chicago, IL, 2011, pp. 1-6.

[11] O. Hegazy, J. Van Mierlo and P. Lataire, "Design and control of bidirectional DC/AC and DC/DC converters for plug-in hybrid electric vehicles," *2011 International Conference on Power Engineering, Energy and Electrical Drives*, Malaga, 2011, pp. 1-7.

[12] J. W. Zillman, “A History of Climate Activities”. World Meteorological Organization. July 2009. Available in: https://public.wmo.int/en. Access in: November 15th, 2018.

[13] “The Paris Agreement”. World Meteorological Organization. July 2009. Available in: https://unfccc.int/. Access in: November 15th, 2018.

[14] “Global Greenhouse Gas Emissions Data”. United States Environmental Protection Agency. Available in: https://www.epa.gov/. Access in: November 16th, 2018.

[15] “Reducing Pollution with Electric Vehicles”. U.S. Department of Energy. Available in: https://www.energy.gov/. Access in: November 16th, 2018.

[16] “Alternative Fuels Data Center - Emissions from Hybrid and Plug-In Electric Vehicles”. U.S. Department of Energy. Available in: https://www.energy.gov/. Access in: November 16th, 2018.

[17] D. L. Chandler, “Can today’s EVs make a dent in climate change?”. MIT News Office. August 15, 2016. Available in: http://news.mit.edu/. Access in: November 16th, 2018.

[18] N. Mohan, Tore M. Undeland, William P. Robbins, “*Power electronics Converters, Applications and Design*”, 3rd edition. Willey, 2002.

[19] Dan Lambert , “Lead Acid Battery Lifecycle: Terms and Definitions”. Schneider Electric – Data Center Science Center.

[20] C&D TECHNOLOGIES, INC., “Charger Output AC Ripple Voltage and the affect on VRLA batteries”. Technical Bulletin, 2012.

[21] A. Purvins, O. Krievs, I. Steiks and L. Ribickis, "Influence of the current ripple on the hydrogen fuel cell powered inverter system efficiency," *2009 13th European Conference on Power Electronics and Applications*, Barcelona, 2009, pp. 1-7.

[22] W. Choi, P. N. Enjeti, J. W. Howze, G. Joung ,“An experimental evaluation of the effects of ripple current generated by the power conditioning stage on a proton exchange membrane fuel cell stack”, Journal of Materials Engineering and Performance, 2004, Volume 13, Number 3, Page 257.

[23] L. Schindele, M. Braun and H. Spath, "The influence of power electronic dynamics on PEM fuel cell-system," *2005 European Conference on Power Electronics and Applications*, Dresden, 2005, pp. 9 pp.-P.9.